

Representation and manipulation of images based on linear functionals

Citation for published version (APA):

Janssen, B. J. (2009). *Representation and manipulation of images based on linear functionals*. [Phd Thesis 1 (Research TU/e / Graduation TU/e), Biomedical Engineering]. Technische Universiteit Eindhoven.
<https://doi.org/10.6100/IR642780>

DOI:

[10.6100/IR642780](https://doi.org/10.6100/IR642780)

Document status and date:

Published: 01/01/2009

Document Version:

Publisher's PDF, also known as Version of Record (includes final page, issue and volume numbers)

Please check the document version of this publication:

- A submitted manuscript is the version of the article upon submission and before peer-review. There can be important differences between the submitted version and the official published version of record. People interested in the research are advised to contact the author for the final version of the publication, or visit the DOI to the publisher's website.
- The final author version and the galley proof are versions of the publication after peer review.
- The final published version features the final layout of the paper including the volume, issue and page numbers.

[Link to publication](#)

General rights

Copyright and moral rights for the publications made accessible in the public portal are retained by the authors and/or other copyright owners and it is a condition of accessing publications that users recognise and abide by the legal requirements associated with these rights.

- Users may download and print one copy of any publication from the public portal for the purpose of private study or research.
- You may not further distribute the material or use it for any profit-making activity or commercial gain
- You may freely distribute the URL identifying the publication in the public portal.

If the publication is distributed under the terms of Article 25fa of the Dutch Copyright Act, indicated by the "Taverne" license above, please follow below link for the End User Agreement:

www.tue.nl/taverne

Take down policy

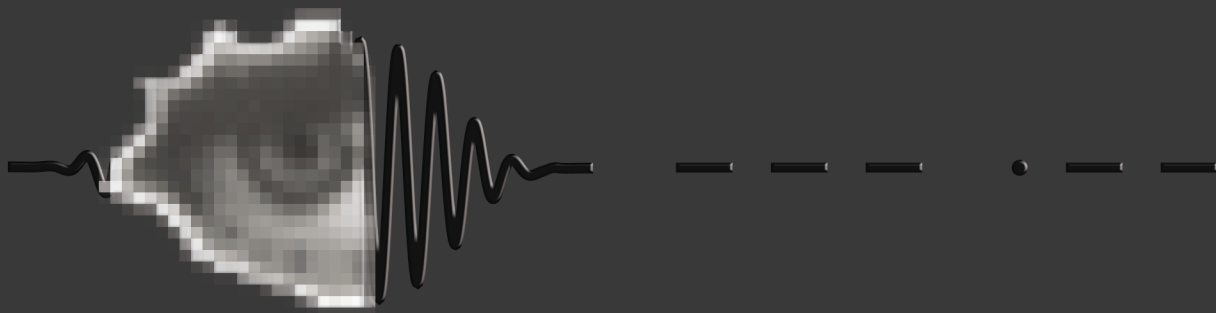
If you believe that this document breaches copyright please contact us at:

openaccess@tue.nl

providing details and we will investigate your claim.

Representation and Manipulation of Images Based on Linear Functionals

B.J. Janssen



Representation and Manipulation of Images Based on Linear Functionals

Colophon

Cover design by Bart Janssen and Marjan Aben.

This thesis was typeset by the author using L^AT_EX_{2 ϵ} .

The Netherlands Organisation for Scientific Research (NWO) is gratefully acknowledged for financial support.

This work was part of NWO vici project “The Problem of Scale in Biomedical Image Analysis”, project number 639.023.403.

Printed by PrintPartners Ipskamp, Enschede, the Netherlands.

A catalogue record is available from the Eindhoven University of Technology Library.

ISBN: 978-90-386-1806-7

© 2009 B.J. Janssen Eindhoven, The Netherlands, unless stated otherwise on chapter front pages, all rights are reserved. No part of this publication may be reproduced or transmitted in any form or by any means, electronic or mechanical, including photocopying, recording, or any information storage and retrieval system, without permission in writing from the copyright owner.

Representation and Manipulation of Images Based on Linear Functionals

PROEFSCHRIFT

ter verkrijging van de graad van doctor aan de
Technische Universiteit Eindhoven, op gezag van de
Rector Magnificus, prof.dr.ir. C.J. van Duijn, voor een
commissie aangewezen door het College voor
Promoties in het openbaar te verdedigen
op maandag 25 mei 2009 om 16.00 uur

door

Bart Jozef Janssen

geboren te Geldrop

Dit proefschrift is goedgekeurd door de promotoren:

prof.dr. L.M.J. Florack

en

prof.dr.ir. B.M. ter Haar Romeny

Copromotor:

dr.ir. R. Duits

Contents

Colophon	ii
Contents	v
1 Introduction and Outline	1
1.1 Introduction	2
1.1.1 Reconstruction from Sparse Image Representations .	4
1.1.2 Enhancement of Time-Frequency Representations . .	5
1.2 Outline of this Thesis	8
2 Linear Reconstruction	11
2.1 Introduction	12
2.2 Theory	13
2.3 Reconstruction from Singular Points	16
2.3.1 Singular Points	17
2.3.2 Prior Selection	17
2.3.3 Implementation	19
2.3.4 Richer Features	22
2.4 Evaluation	22
2.4.1 Qualitative Evaluation	23
2.4.2 Quantitative Evaluation	25
2.5 Conclusions & Recommendations	26
3 Linear Reconstruction on the Bounded Domain	29
3.1 Introduction	30
3.2 Theory	32
3.2.1 Spectral Decomposition	35
3.2.2 Scale Space on the Bounded Domain	37
3.2.3 The Solution to the Reconstruction Problem	39
3.2.4 Neumann Boundary Conditions	40
3.2.5 Singular Points	42
3.3 Implementation	44
3.4 Experiments	46
3.5 Conclusion	51
4 Coarse-to-Fine Reconstruction	53
4.1 Introduction	54
4.2 Image Reconstruction	55

4.3	Approximation	56
4.3.1	Noise Propagation	57
4.3.2	Discretization	58
4.4	Adaptation to a Gauge Field	61
4.4.1	Connections on Vector Bundles	62
4.5	Multi-Scale Approximate Reconstruction	66
4.6	Conclusions	69
5	Left-Invariant Reassignment on the Heisenberg Group	71
5.1	Introduction	72
5.2	Gabor Transforms	73
5.3	The Weyl-Heisenberg Group	75
5.3.1	Differential Operators on the Weyl-Heisenberg Group	76
5.3.2	Phase-Space	79
5.4	Cauchy-Riemann Equations and Window Selection	80
5.5	Reassignment	83
5.6	Discretization	85
5.6.1	Discrete Left-Invariant Vector Fields	88
5.6.2	Phase-Space	89
5.6.3	Discrete Cauchy-Riemann Equations	90
5.6.4	Discrete Reassignment on Phase-Space	93
5.7	Evaluation	94
5.8	Conclusions	96
6	Left-Invariant Diffusion on the Heisenberg Group	105
6.1	Introduction	106
6.2	Non-Linear Anisotropic Diffusion on \mathbb{R}^2	107
6.3	CED on the Weyl-Heisenberg Group	108
6.3.1	Principal Diffusion Directions on H_r	109
6.3.2	Non-Linear Diffusion on H_r	110
6.3.3	Non-Linear Anisotropic Left-Invariant Diffusion	111
6.4	Evaluation	112
6.5	Conclusions	113
7	Summary and Future Research	119
7.1	Summary	120
7.2	Future Research	122
A	Appendix to Chapter 2	123
A.1	Simple Alternative Approach to Theorem 2.2.2	124

B	Appendix to Chapter 3	125
B.1	Green's Function of the Dirichlet Operator on a Rectangle .	126
B.2	The Green's Function as a Limit of the Dirichlet Kernel . .	129
C	Appendix to Chapter 5	131
C.1	Diagonalization of the Gabor Frame Operator	132
	Bibliography	135
	Samenvatting (Summary in Dutch)	147
	Dankwoord	151
	Curriculum Vitae	153
	Publications	155

1

Introduction and Outline

1.1 Introduction

As you read this sentence in the thesis that lies before you, your brain is extracting information mediated by the photons that reflected from this page onto the receptive fields in the retinas of your eyes. The retinal receptive fields connect via the optic nerve to the visual cortex of your brain. Already at this point the human visual system has a difficult problem to solve: Typical receptive field sizes increase as a function of distance to the fovea, which is the part of the retina that contains the smallest and most densely packed receptive fields. As a result the image that is mapped to the cortical surface (a *representation* of the optical world) is hard to interpret directly and has to be reformatted such that it is better suited for further analysis. This reformatting we refer to as *reconstruction*. A visualization of the mapping from the real world to the cortical surface, which is believed to be close to a log-polar mapping [95], and the image to which the mapping is applied, is shown in Figure 1.1. Given the image in the right part of this figure one would like to obtain the “undeformed” image that is shown on the left.

Similar inverse problems occur when a magnetic resonance imaging (MRI) scan, computed tomography (CT) scan or a picture with a photo camera is made. The observations that are done by, e.g., counting the number of photons that hit the surface of a detector during some period of time have to be decoded into a representation that is more useful for further processing. In this thesis we will discuss how one can retrieve a convenient representation of “the real world” when only a few measurements are done with receptors of varying shapes and sizes. The information in these measurements is usually insufficient for a perfect reconstruction therefore we aim at providing a plausible representation based on the information we are given. Apart from reconstruction of images or signals we will discuss enhancement. Enhancement methods aim at getting a convenient or in some sense more appealing (approximate) representation of a signal or image.

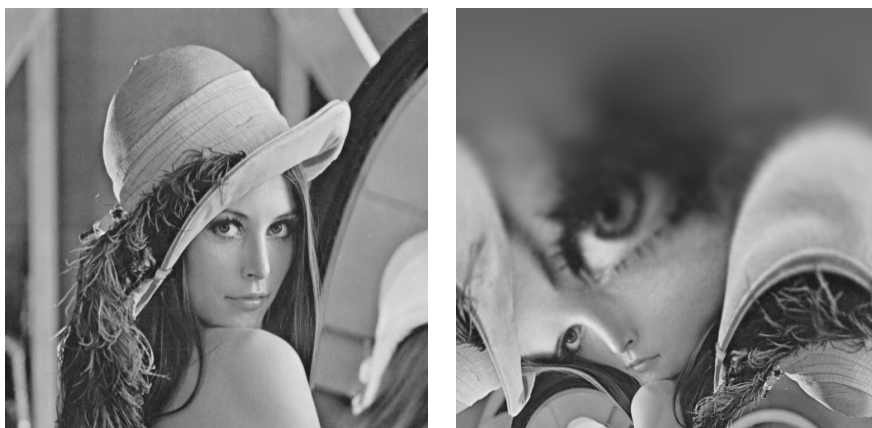


Figure 1.1: The image on the right is obtained by applying a log-polar map to the image on the left. Such a mapping is believed to take place when the optical world is mapped to the cortical surface.

1.1.1 Reconstruction from Sparse Image Representations

Image and signal processing techniques heavily rely on the representation of the signals or images they act on. For certain classes of algorithms such as image matching it is beneficial to employ an adaptive sparse representation of the underlying image. A sparse representation of an image can be thought of as a relatively small set of linear functionals on the image, or “features”. In this thesis we present several methods to reconstruct images or signals from sparse representations. We restrict ourselves to linear representations.

An interesting linear representation is the Gaussian scale space representation of an image. This representation is useful since it makes the scale component of the represented image explicit. Scale (in the sense of inverse resolution) is an inherent property of images and signals in general. Iijima [57] was the first to propose such a representation in the Japanese literature. In 1983 Witkin [118] and Koenderink [74] introduced it to the western scientific community.

The application of catastrophe theory in Gaussian scale space theory led to the identification of special singularities in the Gaussian scale space representation of images. Image matching work by Platel and Balmashnova shows that the locations of singularities and their properties are ideally suited [92, 6] for pattern recognition tasks. Janssen and Florack [63, 43] showed the applicability of singular point tracking in time sequences for motion estimation. To assess the inherently sparse representation of a Gaussian scale space representation of an image by means of its singular points, Nielsen, Lillholm and Griffin [86, 79] developed a reconstruction algorithm. Related approaches for reconstruction from zero-crossings in wavelet representations of images can also be found in literature [82].

In this thesis we develop reconstruction methods and apply them to the reconstruction from measurements that are taken at the locations of these singularities in the scale space representation of an image. Figure 1.2 shows a projection of the famous “Lena” image onto a plane. The figure gives an interpretation of the scale space representation of “Lena”. Here the z -direction corresponds to the scale parameter. A point that is further away from the depicted plane corresponds to a larger scale and thus a more blurred view of the image that is depicted on the plane. Now measurements are taken at the locations of the balls that are depicted in the image, where

the height of the ball corresponds to the size of the receptive field. A ball at a greater height covers a larger area of the image. The location of such a ball corresponds to the location of a singular point in the scale space representation of the image that is shown on the plane in the figure. Paths on which the balls are located are called critical paths and correspond to spatial local extrema. The number of measurements is very small compared to the number of pixels we need to represent the image on a computer screen. The task we take upon ourselves is to find an image that looks as much as possible like the image the measurements have been obtained from.

Although we apply our algorithms to the reconstruction from properties of singular points of Gaussian scale space representations of images we note that the presented algorithms are not limited to this application. Physical measurements can in general be modeled by means of linear functionals and therefore fit in our framework. When there is special structure present in the measurements often more efficient algorithms can be devised to reconstruct the measured physical object. An example of an inverse problem of this type is de-blurring [24], where the assumption of a space invariant point spread function is often quite reasonable. Medical applications such as reconstruction of cone beam CT images or reconstruction from MRI acquisitions also fit in our framework. With respect to the latter example it is shown in [20] that from only a few measurements satisfactory reconstructions can be obtained.

1.1.2 Enhancement of Time-Frequency Representations of Signals

When images or signals are to be manipulated it pays off to select a suitable representation. Duits, van Almsick, and Franken [35, 107, 46] for example showed that orientation scores are suitable representations for the enhancement of elongated structures. These scores make the orientation component explicit and are shown to be of value for crossing preserving image enhancement. This application is a specialization of the general group theoretic framework that was developed in [35]. We use the same framework for the time-frequency analysis of signals.

A musical composition is expressed by means of a musical score such as the one in Figure 1.3. In such a score the pitch and duration are both explicitly

represented at the same time. Such a representation is very convenient and was an inspiration for researchers to come up with a signal transform that has similar properties [48, 30, 31]. This eventually led to a field of research known as time-frequency analysis. The underlying group for the Gabor transform we use to obtain a time-frequency view of a signal is the Weyl-Heisenberg group. Because we recognize the underlying group structure we are able to find representations of a signal that are easier to interpret and still close to the original signal (“reassignment”). Furthermore we are able to enhance the signal itself, making use of the same techniques as those that were used to obtain the reassigned signal.

In fact reconstruction from Gabor transforms of signals or images is again an example of the reconstruction algorithms we mentioned earlier. Here a very special structure is present which allowed researchers to come up with very efficient reconstruction algorithms [8]. We also note that this representation is not signal adaptive and, in our case, highly redundant.

All in all, we present several reconstruction methods to reconstruct from a sparse set of features that are obtained at the locations of image adaptive interest points that are present in the scale space representations of images and show how a time-frequency representations of signals can be enhanced, both in the sense that the time-frequency representation of the signal is easier to interpret and in the sense that spurious structure is removed from the signal itself. To accomplish the enhancement we make use of a group theoretic approach. Time-frequency processing of signals is a step-stone towards time-frequency image processing.

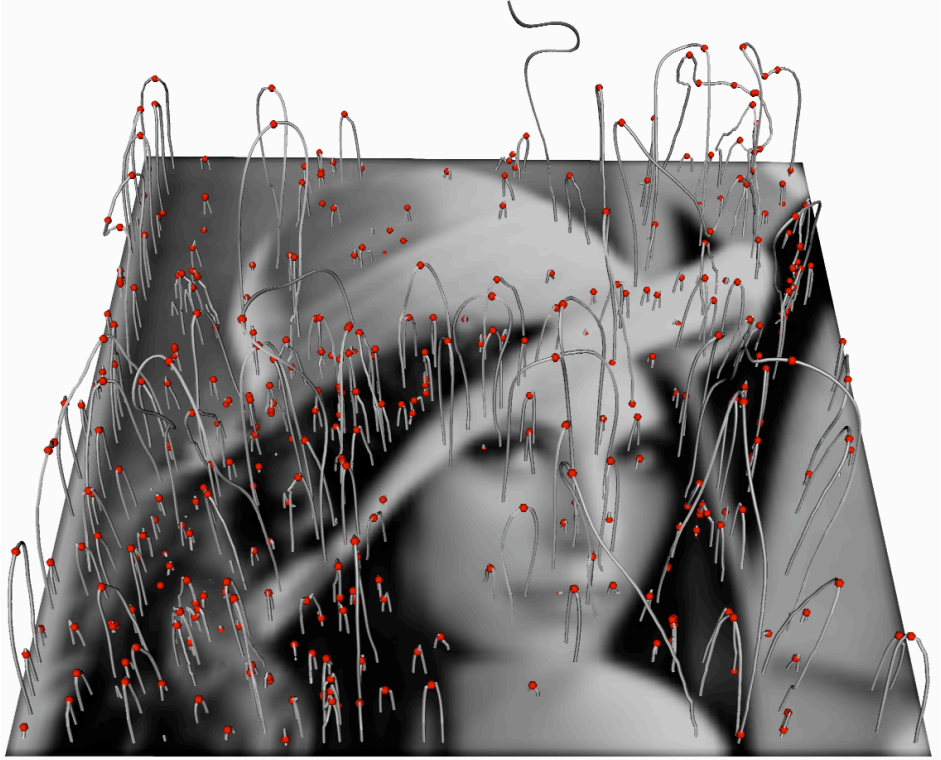


Figure 1.2: A visualization of the critical paths and singular points in the scale space representation of “Lena”. The balls correspond to the locations of singular points. When the ball is further away from the plane on which the image of “Lena” is depicted it corresponds to a larger scale and thereby to a filter that has a larger support. These filters are used to obtain the features from which an image will be reconstructed.



Figure 1.3: An excerpt of the score for “Allegro” in “Concerto per il Clarino” by Joseph Haydn (arranged for B♭ trumpet). This concert for the predecessor of the trumpet was composed for Anton Weidinger, the inventor of the first keyed trumpet [112].

1.2 Outline of this Thesis

The outline of this thesis is as follows.

Chapter 2 discusses the reconstruction from differential structure that is obtained at the locations of singular points of a scale space representation of an image by means of orthogonal projections. The proposed method is applicable to the reconstruction from a set of linear functionals on the image to which we will henceforth refer as *features*. To obtain a visually appealing reconstruction a prior (model) is minimized while insisting on the features to hold. That is, both the original image the features were extracted from and the reconstructed image share the same features. Any prior that is a norm formed by an inner product can be mapped to the presented framework. We select a norm of Sobolev type to demonstrate the method.

In Chapter 3 the reconstruction method is formulated on the bounded domain. The framework that was presented in Chapter 2 on the unbounded domain is adapted such that all operators, including the scale space generators, are confined to the bounded domain on which the to-be-reconstructed-image is defined. This circumvents boundary problems that would arise if the method for unbounded domains were applied to finite-domain images. To avoid approximation and truncation errors the method is implemented such that it is exact on the grid. As a result we can obtain visually more appealing reconstructions compared to those obtained by the method that is presented in Chapter 2 when much regularization is applied.

The reconstructions that are obtained by means of the methods that are presented in Chapter 2 and Chapter 3 give an interpolation of the features. These reconstructions also have to be obtained in a single step, i.e., it is not possible to get a quickly obtainable “preview” of the image at a coarse resolution. Chapter 4 presents a *coarse-to-fine* image reconstruction method that allows an *approximate* reconstruction from the features, i.e., a reconstruction for which the features hold approximately. Information from coarse scale reconstructions is not directly encoded in the features that are used for the finer scale reconstructions but are passed to a finer scale in an implicit manner by means of a gauge field. An advantage of using the gauge field is the reduction of memory consumption and thereby the increase of computational efficiency.

In Chapter 5 the representation of signals in the Gabor domain is discussed. We recognize that Gabor transforms of signals are functions on the Weyl-Heisenberg group. This observation allows us to define differential operators on the Gabor domain that are left-invariant. When an operator on the Gabor domain is left-invariant the corresponding operator on the signal domain is translation and modulation invariant. Using these operators we define a convection process on the Gabor domain of a signal that results in a sharper representation but leaves the signal itself approximately intact. To this end the convection is steered along iso-phase planes in the Gabor domain. The convection process, which is also referred to as *differential reassignment*, is applied on phase-space. This allows for a fast computation compared to computation on the full group. Discretization is done by identifying a discrete group that corresponds to the continuous Weyl-Heisenberg group. The discrete left-invariant vector fields on this discrete group are used to obtain a reassigned time-frequency representation of the signal.

Chapter 6 discusses how the left-invariant vector fields that were obtained in Chapter 5 can be used to enhance the signal itself. To this end a non-linear anisotropic diffusion equation is defined on the domain of Gabor transforms. The initial condition for this evolution equation is the Gabor transform of the raw signal. We show that this diffusion process, which is similar to the coherence enhancing diffusion scheme on images by Weickert [114], can successfully remove noise.



Linear Reconstruction

This chapter is published in:

B.J. Janssen, F.M.W. Kanters, R. Duits, L.M.J. Florack, and B.M. ter Haar Romeny. A linear image reconstruction framework based on Sobolev type inner products. *International Journal of Computer Vision*, 70(3):231–240, 2006. (Invited Paper)

Abstract. Exploration of information content of features that are present in images has led to the development of several reconstruction algorithms. These algorithms aim for a reconstruction from the features that is visually close to the image from which the features are extracted. Degrees of freedom that are not fixed by the constraints are disambiguated with the help of a so-called prior (i.e., a user defined model). We propose a linear reconstruction framework that generalizes a previously proposed scheme. The algorithm greatly reduces the complexity of the reconstruction process compared to non-linear methods. As an example we propose a specific prior and apply it to the reconstruction from singular points. The reconstruction is visually more attractive and has a smaller \mathbb{L}_2 -error than the reconstructions obtained by previously proposed linear methods.

2.1 Introduction

Reconstruction from differential structure of scale space interest points was first introduced by Nielsen and Lillholm [86]. Using the reconstruction the information content of these points can be investigated. Unser and Aldroubi [105] generalized sampling theory by Shannon [97] and Papoulis [90] by finding a consistent reconstruction of a signal from its integer shifted filter responses, i.e., a reconstruction that is indistinguishable from its original when observed through the filters the features were extracted with. The consistency requirement is adopted by Lillholm, Nielsen and Griffin [79, 86] and Kybic et al. [76, 77]. They describe a variational framework that finds a consistent reconstruction that minimizes a so called prior (i.e., a user defined model). The disadvantage of this variational approach is that the reconstruction algorithm is not linear and therefore slow and somewhat cumbersome to implement. Kanters et al. [71] investigated a special case of the reconstruction by Nielsen and Lillholm [86] by adopting the \mathbb{L}_2 -norm as a prior. We shall refer to this as the *standard linear reconstruction scheme*. Advantages of this approach are that the reconstruction algorithm is linear and analytical results for the generalized correlation matrix can be found. The disadvantage is that this method is qualitatively outperformed by nonlinear reconstruction methods [79, 76, 86].

We propose a general reconstruction framework which can be applied to a large set of priors. Any prior that can be described by a norm formed by an inner product can be mapped to this framework. Our method overcomes

the disadvantages of the standard linear reconstruction scheme [71] while retaining linearity. This is done by replacing the \mathbb{L}_2 -inner product by an inner product of Sobolev type. To verify the proposed method we apply it to the reconstruction from singular points. A prior that smoothens the reconstructed image is selected. This results in a reconstruction that has as few additional singular points as possible under the constraints. Also the features are enriched by taking higher order derivatives into account.

For a mathematically rigorous analysis of linear image reconstruction and its connection to Gelfand triples we refer to Duits [41, Section 3.4].

2.2 Theory

Definition 1 (\mathbb{L}_2 -Inner Product). *The \mathbb{L}_2 -inner product for $f, g \in \mathbb{L}_2(\mathbb{R}^2)$ is given by*

$$(f, g)_{\mathbb{L}_2} = \int_{\mathbb{R}^2} \overline{f(x)} g(x) dx . \quad (2.1)$$

This is the standard inner product used in previous work [71, 79, 86].

The reconstruction problem boils down to the selection of an instance of the metameric class consisting of $g \in \mathbb{L}_2(\mathbb{R}^2)$ such that

$$(\psi_i, g)_{\mathbb{L}_2} = c_i , \quad (i = 1 \dots N) \quad (2.2)$$

with ψ_i denoting the distinct localized filters that generate the i^{th} filter response $c_i = (\psi_i, f)_{\mathbb{L}_2} \in \mathbb{C}$, i.e., the selection from the equivalence class of images g that share the same predefined set of features (2.2). The selection of g is done by minimizing a prior subject to the constraints of equation (2.2). A distinction can be made between priors (global constraints) that are constructed by a norm formed by an inner product and those that are constructed by a norm that is not formed by an inner product. In the former case it is possible to translate the reconstruction problem to a linear projection. This maps the reconstruction problem onto straightforward linear algebra. To this end we propose a generalization of Definition 1 as follows.

Definition 2 (A-Inner Product). *We define A to be an operator on $\mathbb{L}_2(\mathbb{R}^2)$*

such that $(I + A^\dagger A)^{-1}$ is bounded¹. Then

$$(f, g)_A = (f, g)_{\mathbb{L}_2} + (Af, Ag)_{\mathbb{L}_2} . \quad (2.3)$$

Note that we can write

$$(f, g)_A = \left(f, (I + A^\dagger A)g \right)_{\mathbb{L}_2} . \quad (2.4)$$

For an image $f \in \mathbb{L}_2(\mathbb{R}^2)$ we consider a collection of filters $\psi_i \in \mathbb{L}_2(\mathbb{R}^2)$ and filter responses $c_i, i = 1, \dots, N$, given by

$$c_i = (\psi_i, f)_{\mathbb{L}_2} . \quad (2.5)$$

Thus the a priori known features are given in terms of an \mathbb{L}_2 -inner product. In order to express these features relative to the new inner product we seek an effective filter, κ_i say, such that

$$(\kappa_i, f)_A = (\psi_i, f)_{\mathbb{L}_2} \quad (2.6)$$

for all f . We will henceforth refer to ψ_i as an “ \mathbb{L}_2 -filter” and to κ_i as its corresponding “A-filter”.

Lemma 2.2.1 (A-Filters). *Given $\psi_i \in \mathbb{L}_2(\mathbb{R}^2)$ then its corresponding A-filter is given by*

$$\kappa_i = (I + A^\dagger A)^{-1} \psi_i . \quad (2.7)$$

Proof. Applying Definition 2,

$$\begin{aligned} (\kappa_i, f)_A &= \left((I + A^\dagger A)^{-1} \psi_i, f \right)_A \\ &= \left((I + A^\dagger A)(I + A^\dagger A)^{-1} \psi_i, f \right)_{\mathbb{L}_2} \\ &= (\psi_i, f)_{\mathbb{L}_2} . \end{aligned} \quad (2.8)$$

□

¹By Neumann [121] p.200, we have that for every closed densely defined operator A in a Hilbert space \mathcal{H} the operator $A^\dagger A$ is self adjoint and $(I + A^\dagger A)$ has a bounded inverse.

We aim to establish a reconstruction g that satisfies equation (2.2) and minimizes

$$E(g) = \frac{1}{2}(g, g)_A . \quad (2.9)$$

Since g satisfies equation (2.2) we may as well write

$$E(g) = \frac{1}{2}((g, g)_{\mathbb{L}_2} + (Ag, Ag)_{\mathbb{L}_2}) - \lambda^i((\psi_i, g)_{\mathbb{L}_2} - c_i) , \quad (2.10)$$

in other words

$$E(g) = \frac{1}{2}(g, g)_A - \lambda^i((\kappa_i, g)_A - c_i) . \quad (2.11)$$

Here and henceforth Einstein summation convention applies to upper and lower feature indices $i = 1 \dots N$, i.e., whenever an upper index matches a lower one it is supposed to be regarded as a dummy summation index. The first term in equation (2.11) is referred to as the *prior*. The remainder consists of a linear combination of *constraints*, recall equation (2.2), with Lagrange multipliers λ^i .

Theorem 2.2.2. *The solution to the Euler-Lagrange equations for equation (2.11) can be found by A -orthogonal projection of the original image f on the linear space V spanned by the filters κ_i , i.e.,*

$$g = \mathcal{P}_V f = (\kappa^i, f)_A \kappa_i . \quad (2.12)$$

Here we have defined $\kappa^i \stackrel{\text{def}}{=} G^{ij} \kappa_j$ with Gram matrix

$$G_{ij} = (\kappa_i, \kappa_j)_A \quad (2.13)$$

and $G^{ik} G_{kj} = \delta_j^i$.

Proof. The functional derivative of equation (2.11) with respect to the image g is given by (recall equation (2.4))

$$\frac{\delta E(g)}{\delta g} = (I + A^\dagger A)g - \lambda^i \psi_i \quad (2.14)$$

The solution to the corresponding Euler-Lagrange equations is formally given by

$$g = \lambda^i (I + A^\dagger A)^{-1} \psi_i = \lambda^i \kappa_i . \quad (2.15)$$

So the filter responses can be expressed as

$$c_i = (\psi_i, g)_{\mathbb{L}_2} = \lambda^j \left(\psi_i, (I + A^\dagger A)^{-1} \psi_j \right)_{\mathbb{L}_2} = \lambda^j (\psi_i, \kappa_j)_{\mathbb{L}_2} = \lambda^j (\kappa_i, \kappa_j)_A . \quad (2.16)$$

Consequently $\lambda^i = G^{ij} c_j$. Applying this to equation (2.15) leads to

$$g = \lambda^i \kappa_i = G^{ij} c_j \kappa_i = G^{ij} (\kappa_j, f)_A \kappa_i = (\kappa^i, f)_A \kappa_i . \quad (2.17)$$

This completes the proof of Theorem 2.2.2. \square

Theorem 2.2.2 refers to an Euler-Lagrange formalism to comply with previous work on this subject [71, 79, 86]. The authors do notice the linear reconstruction problem can be approached in a simpler and more elegant way. This approach is sketched in Appendix A.1.

2.3 Reconstruction from Singular Points

The theory of the previous section is applicable to any set of linear features. Here we are particularly interested in feature attributes of so-called singular points in Gaussian scale space. A Gaussian scale space representation $u(x; s)$ in n spatial dimensions is obtained by convolution of a raw image $f(x)$ with a normalized Gaussian:

$$\begin{aligned} u(x; s) &= (f * \varphi_s)(x) \\ \varphi_s(x) &= \frac{1}{\sqrt{4\pi s}^n} e^{-\frac{\|x\|^2}{4s}} . \end{aligned} \quad (2.18)$$

For the remainder of this paper we use the following convention for the continuous Fourier Transform

$$\begin{aligned} \mathcal{F}(f)(\omega) &= \hat{f}(\omega) = \frac{1}{\sqrt{2\pi}^n} \int_{-\infty}^{\infty} e^{-i\omega x} f(x) dx \\ \mathcal{F}^{-1}(f)(x) &= f(x) = \frac{1}{\sqrt{2\pi}^n} \int_{-\infty}^{\infty} e^{i\omega x} \hat{f}(\omega) d\omega . \end{aligned} \quad (2.19)$$

Notice that with this definition Fourier transformation becomes a unitary transformation.

2.3.1 Singular Points

A *singular point* is a *non-Morse critical point*² of a Gaussian scale space representation of an image. Scale s is taken as a control parameter. This type of point is also referred to in the literature as a *degenerate spatial critical point* or as a *toppoint* or *catastrophe*.

Definition 3 (Singular Point). *A singular point $(x; s) \in \mathbb{R}^{n+1}$ is defined by the following equations, in which ∇ denotes the spatial gradient operator:*

$$\begin{cases} \nabla u(\mathbf{x}; s) = 0 \\ \det \nabla \nabla^T u(\mathbf{x}; s) = 0 \end{cases} \quad (2.20)$$

The behavior near singular points is the subject of *catastrophe theory*. Damon rigorously studied the applicability of established *catastrophe theory* in a scale space context [26]. Florack and Kuijper have given an overview of the established theory in their paper about the topological structure of scale space images for the generic case of interest [44]. More on catastrophe theory in general can be found in a monograph by Gilmore [51].

2.3.2 Prior Selection

Johansen showed [65, 66] that a one dimensional signal is defined up to a multiplicative constant by its singular points. This is probably not the case for two dimensional signals (images). It was conjectured that these points endowed with suitable attributes do contain enough information to be able to obtain a reconstruction that is visually close to the initial image [71, 79, 86].

As can be seen in Figure 2.1 the standard linear reconstruction proposed by Kanters et al. [71], which uses the standard \mathbb{L}_2 -inner product, is far from optimal. The problem can be identified by determining the number of additional singular points that appear in the reconstructed image while strictly insisting on the features to hold. In case of a perfect reconstruction the number of singular points would be equal for the reconstructed and original image. In practice, however, one observes that a reconstruction like the one shown in Figure 2.1 on the right, has more singular points than

²See [51] pp. 13 for notational conventions.

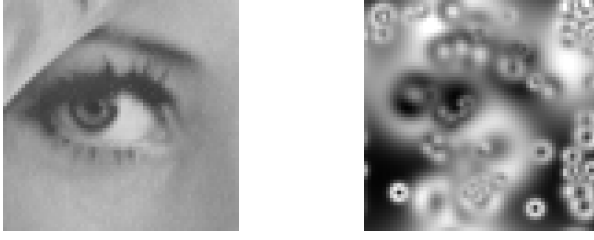


Figure 2.1: The image on the right hand side shows the standard linear reconstruction, taking up to second order differential structure into account, as is proposed by Kanters et al. [71] from 63 singular points of *Lena's eye*. The original image, from which the singular points are taken is shown on the left hand side.

the original image. The number of singular points in the reconstructed image can be reduced by smoothing the image (while not violating the constraints). Therefore a prior derived from the following inner product is proposed³:

$$\begin{aligned} (f, g)_A &= (f, g)_{\mathbb{L}_2} + (-\gamma\sqrt{-\Delta}f, -\gamma\sqrt{-\Delta}g)_{\mathbb{L}_2} = (f, g)_{\mathbb{L}_2} - (f, \gamma^2\Delta g)_{\mathbb{L}_2} \\ &= (f, g)_{\mathbb{L}_2} + (\gamma\nabla f, \gamma\nabla g)_{\mathbb{L}_2} . \end{aligned} \quad (2.21)$$

This prior introduces a smoothness constraint to the reconstruction problem. The degree of smoothness is controlled by the parameter γ . When γ vanishes the projection equals the one from standard linear reconstruction [71]. Note that this is a standard prior in first order Tikhonov regularization [42, 102]. A visualization of the projection using the inner product of equation (2.21) can be found in Figure 2.2.

In practice one should consider

$$f \mapsto (f - \bar{f}) \mathbf{1}_\Omega , \quad (2.22)$$

with \bar{f} the average of f and Ω denotes the support of f . Then for $A = -\gamma\sqrt{-\Delta}$

$$\|f - \bar{f}\|_A^2 = \|f - \bar{f}\|_{\mathbb{L}_2}^2 + \|Af\|_{\mathbb{L}_2}^2 \quad (2.23)$$

is minimized resulting in minimal variance reconstruction.

³The operational significance of the fractional operator $-\sqrt{-\Delta}$, which is the generator of the Poisson scale space, is explained in detail by Duits et al. [38]. In Fourier space it corresponds to the multiplicative operator $-||\omega||$.

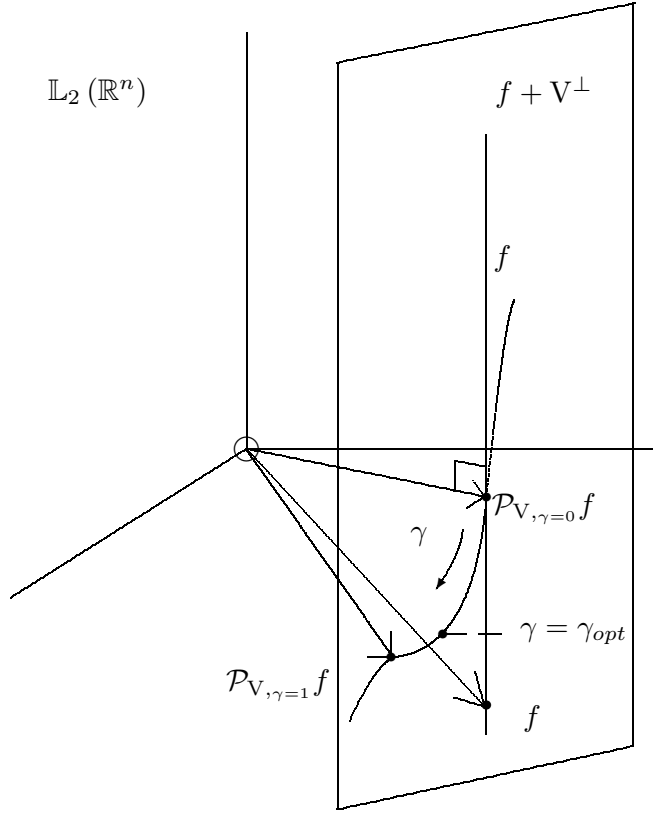


Figure 2.2: Illustration of the metameric class V of images with consistent features. For $\gamma = 0$ we have an orthogonal projection in $\mathbb{L}_2(\mathbb{R}^2)$. For $\gamma > 0$ this is an A -orthogonal projection, which is a skew projection in $\mathbb{L}_2(\mathbb{R}^2)$. The smoothness of the projection increases with $\gamma > 0$.

2.3.3 Implementation

Setting $A = -\gamma\sqrt{-\Delta}$ the A-filter equals

$$\kappa_i = (I - \gamma^2 \Delta)^{-1} \psi_i = \mathcal{F}^{-1} \left(\omega \mapsto \frac{1}{1 + \gamma^2 \|\omega\|^2} \mathcal{F}(\psi_i)(\omega) \right). \quad (2.24)$$

The filter shape in the spatial domain is somewhat harder to obtain. For two dimensions ($n = 2$) the convolution filter that represents the linear operator $(I - \gamma^2 \Delta)^{-1}$ equals

$$\phi_\gamma(x, y) = \frac{1}{2\pi\gamma^2} K_0 \left[\frac{\sqrt{x^2 + y^2}}{\gamma} \right] \quad (2.25)$$

with K_0 the zeroth order modified Bessel function of the second kind. This was also noted by Florack, Duits and Bierkens [42] who worked on Tikhonov regularization and its relation to Gaussian scale space. Notice that this kernel is singular at the origin. This is caused by the fact that a first order Sobolev space on \mathbb{R}^2 is not a reproducing kernel Hilbert space. By slightly increasing the order of the Sobolev space this inconvenience could be circumvented [35]. The nature of the singularity is relatively harmless, however.

The calculation of the Gram matrix G_{ij} (equation (2.13)) is the computationally hardest part of the reconstruction algorithm. An analytic expression for this matrix is not available (unless $\gamma = 0$ [71]). Therefore the inner products $(\kappa_i, \kappa_j)_A$ have to be found by numerical integration. By the Parseval theorem we have (recall equations (2.24) and (2.25))

$$\begin{aligned} (\kappa_i, \kappa_j)_A &= \left(\frac{1}{1 + \gamma^2 \|\omega\|^2} \hat{\psi}_i, \hat{\psi}_j \right)_{\mathbb{L}_2} \\ &= \left(\frac{1}{1 + \gamma^2 \|\omega\|^2}, \hat{\psi}_i \hat{\psi}_j \right)_{\mathbb{L}_2} \\ &= \left(\phi_\gamma, \bar{\psi}_i * \psi_j \right)_{\mathbb{L}_2} . \end{aligned} \tag{2.26}$$

In which ϕ_γ is given by equation (2.25).

At this point we have not yet specified the ψ_i filters. Since we are interested in the properties of singular points in Gaussian scale space we define the filters as follows.

Definition 4 (Feature Extraction). *A filter ψ_i is a localized derivative of the Gaussian kernel, recall equation (2.18), at a certain scale. Given $x, y, \xi, \eta \in \mathbb{R}$ and $m, n \in \mathbb{N}_0$*

$$\psi_i(x, y) \stackrel{\text{def}}{=} \frac{\partial^{m+n} \varphi_s(\xi - x, \eta - y)}{\partial x^m \partial y^n} \tag{2.27}$$

with $i \stackrel{\text{def}}{=} (m, n, \xi, \eta, s) \in \mathbb{N}_0^2 \times \mathbb{R}^2 \times \mathbb{R}_+$.

Notice that

$$\begin{aligned}
 \left(\frac{\partial^{m+n}}{\partial x^m \partial y^n} u \right) (\xi, \eta, s) &= \left(\frac{\partial^{m+n}}{\partial x^m \partial y^n} \varphi_s * f \right) (\xi, \eta) \\
 &= \int f(x, y) \left(\frac{\partial^{m+n}}{\partial x^m \partial y^n} \varphi_s \right) (\xi - x, \eta - y) dx dy \\
 &= (\bar{\psi}_i, f) = (\psi_i, f)
 \end{aligned} \tag{2.28}$$

since $\bar{\psi}_i = \psi_i$. So the differential structure at a point in scale space can be described by a set of linear functionals on the image f .

Applying Definition 4 to equation (2.26) reveals that the inner products in the Gram matrix can be expressed as a Gaussian derivative of the spatial representation of ϕ_γ . Note that this can be exploited for any operator that one chooses to use as a regularizer.

The singularity of $\phi_\gamma(x)$ at the origin gives rise to numerical problems. The Fourier representation $\hat{\phi}_\gamma(x)$ does not have a singularity, therefore the Fourier representation of the operator is sampled and after that a discrete inverse Fourier transform is applied to it.

At this point we could construct the Gram matrix and obtain the solution of our reconstruction problem, according to equation (2.17)

$$g = G^{ij} c_j \kappa_i . \tag{2.29}$$

Instead, in order to improve accuracy, we rewrite our problem in the following manner,

$$g = \tilde{G}^{ij} \tilde{c}_j \tilde{\kappa}_i , \tag{2.30}$$

with , $\tilde{G}_{ij} = \frac{G_{ij}}{\sqrt{G_{ii}}\sqrt{G_{jj}}}$ (no summation convention), $\tilde{c}_j = \frac{1}{\sqrt{G_{jj}}}c_j$ and $\tilde{\kappa}_i = \frac{1}{\sqrt{G_{ii}}}\kappa_i$. This way the condition number of the matrix to be inverted,

$$C = \sqrt{\frac{\mu_1}{\mu_n}} , \tag{2.31}$$

with $\mu_1 \geq \mu_2 \geq \dots \geq \mu_n > 0$ its eigenvalues, can be controlled. Since the condition number solely depends on the largest and the smallest eigenvalue we can easily minimize equation (2.31) by setting the diagonal of this

matrix to unity, as is expressed in equation (2.30). In matrix notation we note that (underscore denotes vectorial representation)

$$(S\underline{\kappa})^T (SGS)^{-1} S\underline{c} = \underline{\kappa}^T G^{-1} \underline{c} , \quad (2.32)$$

where we used $S^T = S$, with

$$S_{ij} = \begin{cases} \frac{1}{\sqrt{G_{ii}}} & \text{if } i = j \\ 0 & \text{if } i \neq j \end{cases} , \quad (2.33)$$

$$\underline{\kappa} = (\kappa_1, \dots, \kappa_N)^T \text{ and } \underline{c} = (c_1, \dots, c_N)^T .$$

2.3.4 Richer Features

Obtaining a visually appealing reconstruction from singular points can be achieved by selecting an “optimal” space for projection. This approach is discussed above. Another way to enhance the quality of the reconstruction is by using more information about the points that are used for reconstruction, i.e., by using richer features. In the standard case only up to second order differential structure was used. In our experiments also higher order differential properties of the singular points were taken into account. This has the side effect that the Gram matrix will be harder to invert when more possibly dependent properties are used.

2.4 Evaluation

To evaluate the suggested prior and the proposed reconstruction scheme reconstructions from singular points of different images are performed. The singular points are obtained using ScaleSpaceViz [69] (available on the web), which is based on a zero-crossings method. After the singular points are found the unstable ones are filtered out by applying a threshold on the amount of structure that is present around a singular point. The amount of structure can be found by calculating the “differential quadratic total variation norm” or “deviation from flatness”

$$\text{tv} = \sigma^4 \text{Tr}(\mathbf{H}^2) \quad (2.34)$$

that was proposed by Platel et al. [93]. Here \mathbf{H} represents the Hessian matrix and σ represents the scale at which the singular point appears. The reconstruction algorithm is implemented in Mathematica [119].

The images that are chosen to evaluate the performance of the reconstruction algorithm are those used by Kanters et al. and Lillholm et al. for the evaluation of their reconstruction algorithms [71, 79], *Lena's eye* and *MR brain*. The size of the former image is 64×64 pixels and the size of the latter image is 128×128 pixels. The pixel values of these images are integer valued ranging from 0 to 255.

2.4.1 Qualitative Evaluation

First we study reconstruction from singular points taking into account up to second order derivatives of the image at the locations of the singular points. Figure 2.3 shows the reconstruction from 31 singular points of *Lena's eye*. These points are selected using a tv-norm of 32. Note that the tv-norm scales with the square of the image range. The first image in the upper row displays the image from which the singular points were obtained. Successive images are reconstructions from these points with an increasing γ . The second image in the first row shows a reconstruction with $\gamma = 0$, which equals the reconstruction by Kanters et al. [71, 70], and the first picture in the second row depicts the reconstruction with a minimal relative \mathbb{L}_2 -error. The same convention is used in the reconstruction from 55 singular points of *MR brain* that is displayed in Figure 2.4. The singular points of this image were acquired using a tv-norm of 128. Figure 2.3 shows the “fill-in effect” of the smoothing prior. The reconstruction with the smallest relative \mathbb{L}_2 -error is visually more appealing than the images with a smaller γ . A reconstruction with $\gamma = 250$ lacks details that were visible in the other reconstructions. This happens because the Gram matrix is harder to invert when dependent basis functions are used. With an increasing γ the kernels become wider and thus more dependent on one another. The reconstructions of *MR brain* show “leaking” edges. Because the prior smooths the image the very sharp edges of this image are not preserved and consequently the leaking effect appears.

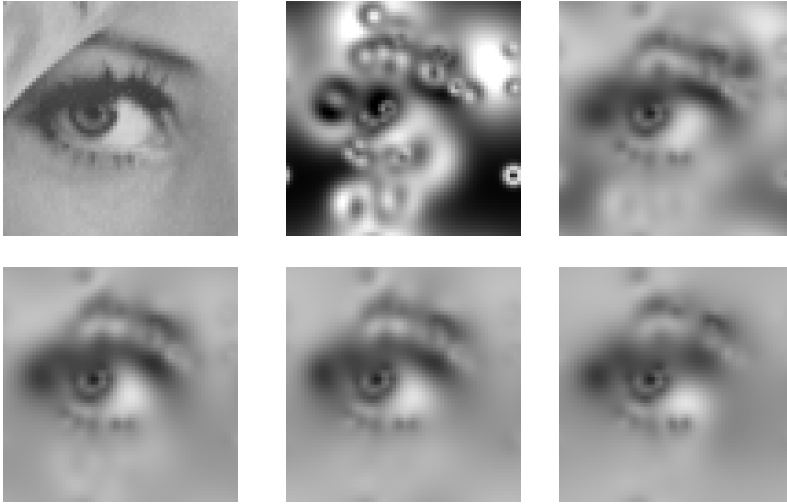


Figure 2.3: Reconstruction from 31 singular points of *Lena's eye* with up to second order features. The upper row shows the original image and reconstructions with $\gamma = 0$ and $\gamma = 5$. The second row shows reconstructions with $\gamma = 22$, $\gamma = 50$ and $\gamma = 250$. The first image in the second row shows the reconstruction with the lowest relative \mathbb{L}_2 -error.

To investigate the influence of enrichment of the features the same experiments are repeated but up to fourth order derivatives are taken into account in the features. The results for the reconstruction from the singular points of *Lena's eye* can be found in Figure 2.5 and the results for the reconstruction from the singular points of *MR brain* are depicted in Figure 2.6. In both cases the images show more detail and are visually more appealing than their second order counter parts. The reconstruction of the *MR brain* image still shows leakage, but this effect is reduced when compared to second order reconstruction. Inspection of Figures 2.3, 2.4, 2.5 and 2.6 shows that, although the reconstructions are still far from optimal, remarkably few singular points are involved relative to the total number of pixels.

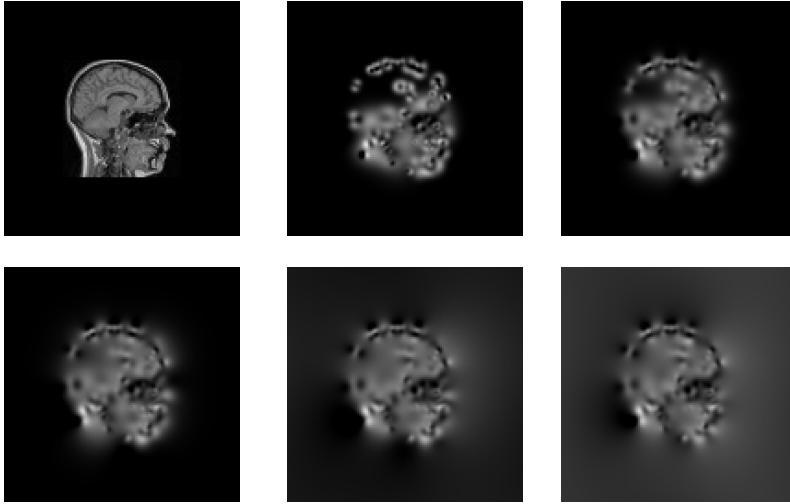


Figure 2.4: Reconstruction from 55 singular points of *MR brain* with up to second order features. The upper row shows the original image and reconstructions with $\gamma = 0$ and $\gamma = 3$. The second row shows reconstructions with $\gamma = 7$, $\gamma = 50$ and $\gamma = 250$. The first image in the second row shows the reconstruction with the lowest relative \mathbb{L}_2 -error.

2.4.2 Quantitative Evaluation

In order to verify the quality of the reconstructions of both images under a varying γ the relative \mathbb{L}_2 -error⁴,

$$\mathbb{L}_2\text{-error} = \frac{\|f - g\|_{\mathbb{L}_2}}{\|f\|_{\mathbb{L}_2}}, \quad (2.35)$$

of the reconstructed images is calculated. Figure 2.7 shows four graphs depicting this error for both second order and fourth order reconstruction of *Lena's eye* and *MR brain*. All graphs show that an optimal value exists for the γ parameter. This can be explained by the fact that the Gram matrix is harder to invert with increasing γ due to increasing correlation among the filter cf. equation (2.26). Because of that dependent equations will be removed during the Singular Value Decomposition, which is used to obtain the inverse of the Gram matrix. This leads to a reconstruction with less detail and thus a larger \mathbb{L}_2 -error. The reconstructions of the

⁴An exposition of several alternative measures that can be used to assess the reconstruction quality can be found in [68].

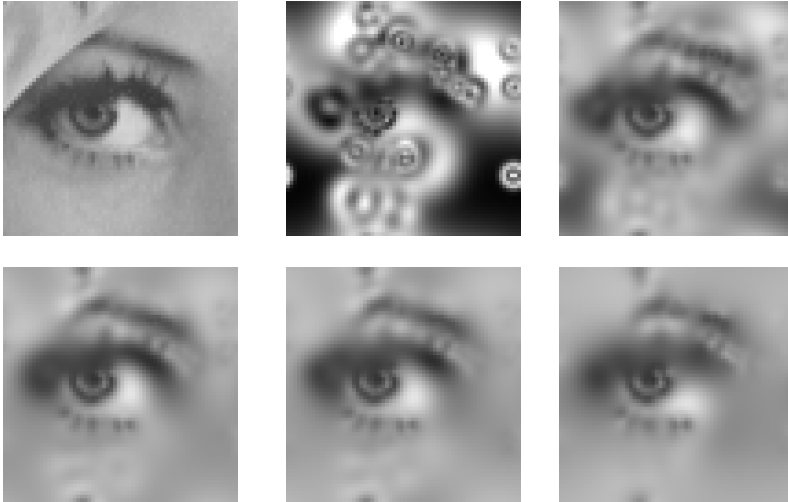


Figure 2.5: Reconstruction from 31 singular points of *Lena's eye* with up to fourth order features. The upper row shows the original image and reconstructions with $\gamma = 0$ and $\gamma = 4$. The second row shows reconstructions with $\gamma = 19$, $\gamma = 50$ and $\gamma = 250$. The first image in the second row shows the reconstruction with the lowest relative \mathbb{L}_2 -error.

MR brain image show an increasing \mathbb{L}_2 - error with an increasing γ . This error becomes even larger than the \mathbb{L}_2 -error of the reconstruction with $\gamma = 0$. This can be attributed to the sharp edges of the head that are smoothed and thus show leakage into the black surroundings of the head. The background clearly dominates the contribution to the \mathbb{L}_2 -error. The reconstruction of *Lena's eye* does not suffer from this problem because of its smoothness.

2.5 Conclusions & Recommendations

We proposed a linear reconstruction method that leaves room for selection of arbitrary priors as long as the prior is a norm of Sobolev type. This greatly reduces the complexity of the reconstruction algorithm compared to non-linear methods.

We select one possible prior characterized by a free parameter γ that aims for a smooth reconstruction. This provides a control parameter for select-

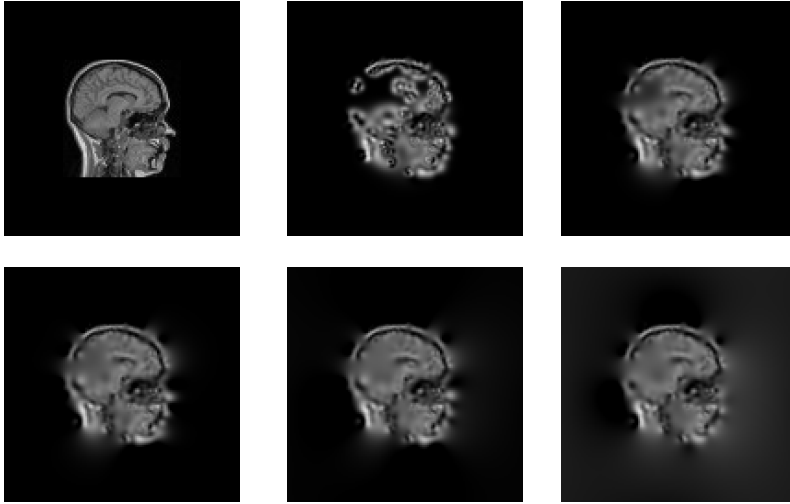


Figure 2.6: Reconstruction from 55 singular points of *MR brain* with up to fourth order features. The upper row shows the original image and reconstructions with $\gamma = 0$ and $\gamma = 4$. The second row shows reconstructions with $\gamma = 8$, $\gamma = 50$ and $\gamma = 250$. The first image in the second row shows the reconstruction with the lowest relative \mathbb{L}_2 -error.

ing different metameric reconstructions, i.e., reconstructions all consistent with the prescribed constraints. Comparisons with standard linear reconstruction as done by Kanters et al. [71] show it is possible to improve the reconstruction quality while retaining linearity. Reconstruction from a selection of singular points of the *MR brain* image proves to be more difficult than reconstruction of smoother images like *Lena's eye*. The problem, that shows up as “leaking” edges, is reduced by taking higher order differential structure into account in the reconstruction algorithm. When the γ parameter is increased basis functions get more dependent on each other. This leads to a harder to invert Gram matrix and consequently to a reduction of detail in the reconstruction.

Both, taking a $\gamma > 0$ and taking higher order features into account, lead to visually more appealing images and a smaller \mathbb{L}_2 -error when compared to standard linear reconstruction. It remains an open question how to select an optimal γ .

Future work will include the use of anisotropic diffusion depending on the local image orientation and investigation of so called flux features.

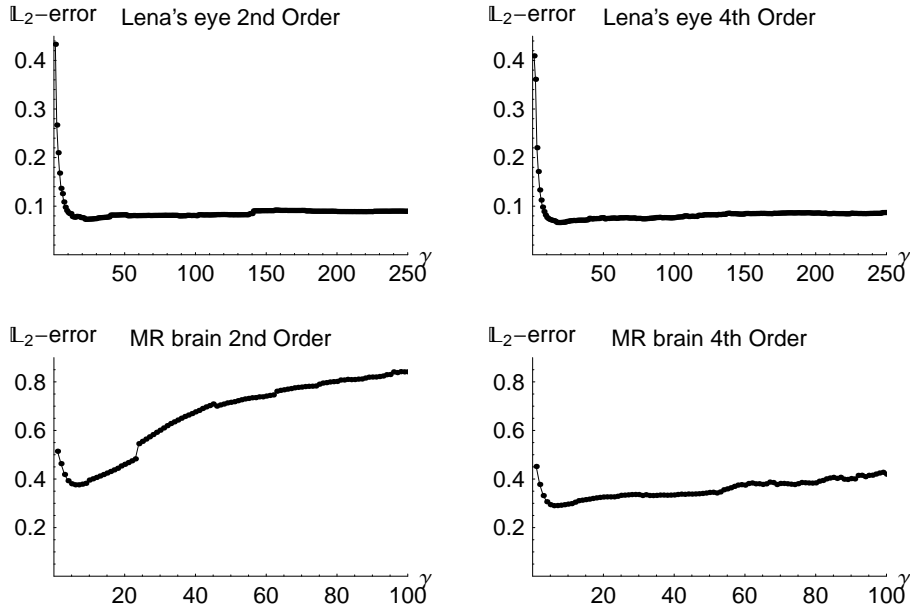


Figure 2.7: The relative \mathbb{L}_2 -error of the reconstructions from 31 singular points of *Lena's eye* (upper row) and 55 singular points of *MR brain* (lower row). The first column shows the \mathbb{L}_2 -error for varying γ when second order reconstruction is used, i.e., up to second order derivatives are taken into account in the features. The second column displays fourth order reconstruction. The minimal relative \mathbb{L}_2 -errors of the reconstructions of *Lena's eye* ($\gamma = 22$ and $\gamma = 19$) are larger than those of *MR brain* ($\gamma = 7$ and $\gamma = 8$). This suggests, in order to reduce the “fill-in effect” that causes this difference for the optimal value of γ , the use of anisotropic diffusion (which will be addressed in future work).

A large, light gray, stylized number '3' is centered in the background of the page.

Linear Reconstruction on the Bounded Domain

This chapter is published in:

B.J. Janssen and R. Duits. Linear image reconstruction by Sobolev norms on the bounded domain. *International Journal of Computer Vision*, 84(2):205–219, August 2009. (Invited Paper)

Abstract. The reconstruction problem is usually formulated as a variational problem in which one searches for that image that minimizes a so called prior (image model) while insisting on certain image features to be preserved. When the prior can be described by a norm induced by some inner product on a Hilbert space, the exact solution to the variational problem can be found by orthogonal projection. In previous work we considered the image as compactly supported in $\mathbb{L}_2(\mathbb{R}^2)$ and we used Sobolev norms on the unbounded domain including a smoothing parameter $\gamma > 0$ to tune the smoothness of the reconstructed image. Due to the assumption of compact support of the original image, components of the reconstructed image near the image boundary are too much penalized. Therefore, in this work we minimize Sobolev norms only on the actual image domain, yielding much better reconstructions (especially for $\gamma \gg 0$). As an example we apply our method to the reconstruction of singular points that are present in the scale space representation of an image.

3.1 Introduction

One of the fundamental problems in signal processing is the reconstruction of a signal from its samples. In 1949 Shannon published his work on signal reconstruction from its equispaced ideal samples [97]. Many generalizations [90, 104] and applications [77, 20] followed thereafter.

Reconstruction from differential structure of scale space interest points, first introduced by Nielsen and Lillholm [86], is an interesting instance of the reconstruction problem, since the samples are non-uniformly distributed over the image they were obtained from and the filter responses of the filters do not necessarily coincide. Several linear and non-linear methods [86, 64, 76, 79] appeared in literature which all search for an image that (1) is indistinguishable from its original when observed through the filters the features were extracted with, and (2) simultaneously minimizes a certain prior. If such a prior is a norm of Sobolev type on the *unbounded* domain one can obtain visually attractive reconstructions while retaining linearity, as we have shown in earlier work [64, 35]. However, boundaries often cause problems to signal processing algorithms (see, e.g., [83, Chapter 7.5] or [27, Chapter 10.7]) and should be handled with care.

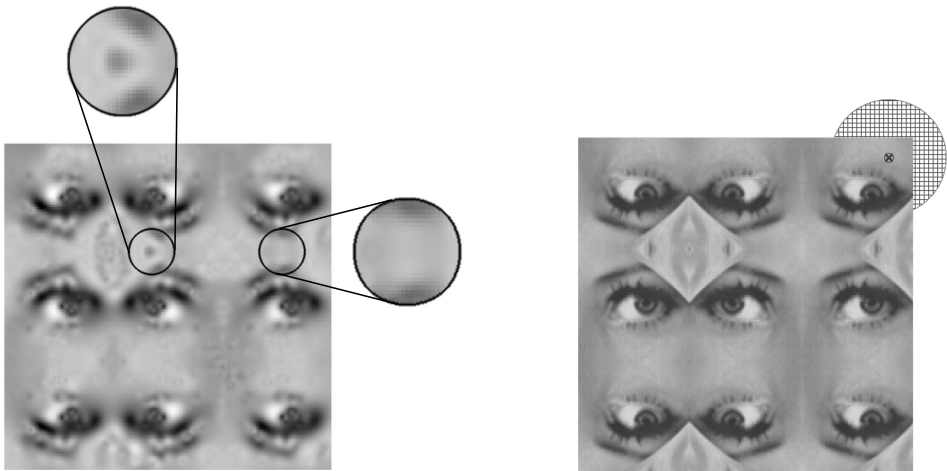


Figure 3.1: The left image shows a reconstruction from differential structure obtained from the right image using the unbounded domain reconstruction method as presented in our previous work [64]. The upper circle in the right image shows a detail of an area near the center of the image and the circle on the right shows a corresponding area near the boundary of the image. One would expect that the same details would appear in both circles. However, this is not the case since kernels that are associated to image-features partly lay outside the image domain and are, as a consequence, penalized by the energy minimization methods that are defined on the unbounded domain. This is illustrated by a marked circle, placed on top of the input image that is displayed on the right.

The problem that appears in the unbounded domain reconstruction method is illustrated in Figure 3.1. In this figure the left image is a reconstruction from differential structure obtained from a concatenation of (mirrored) versions of Lena’s eye. The input image is depicted on the right of Figure 3.1 and is still considered as a compactly supported element in $\mathbb{L}_2(\mathbb{R}^2)$, as required in our *previous* work [64]. So the mirroring has nothing to do with boundary conditions. In this particular case we observe that our previous work shows limitations. If the reconstruction method on the unbounded domain would work properly, details that appear in the center of the image are also expected to appear at the corresponding locations near the boundary of the image. This is, however, not the case. To clarify this observation we depicted two magnifications of corresponding positions in the image. The upper circle in Figure 3.1 contains a magnification of a part taken from the center of the reconstructed image. This will henceforth be called “magnification a ”. The circle on the right contains a magnification

of a corresponding patch near the boundary and is referred to as “magnification b ”. Note that magnification a contains details that magnification b does not contain.

This problem can be attributed to the fact that kernels, associated to the image-features, partly lay outside the image domain and are “penalized” by the energy minimization methods on the unbounded domain. As a result the reconstructed image shows defects, in particular near the boundary. Even kernels that are attached to features close to the center of the image are unnecessarily suppressed by the energy minimization formulated on the unbounded domain. So the reconstruction depicted in magnification a still suffers from a boundary problem, although less visible than the reconstruction of magnification b .

A first rough approach to tackle this problem could be to extend the image symmetrically in all directions and cut out the center after reconstruction. This results in an increase in computation time and it still does not solve the problem in a rigorous manner. Instead, in this article we solve this problem by considering bounded domain Sobolev norms. An additional advantage of our method is that we can enforce a much higher degree of regularity than the unbounded domain counterpart. Furthermore, we give an interpretation of the 2 parameters that appear in the reconstruction framework in terms of filtering by a low-pass Butterworth filter. This allows for a good intuition on how to choose these parameters.

3.2 Theory

In order to avoid the problem discussed in the introduction and illustrated in Figure 3.1 we restrict the reconstruction problem to the domain $\Omega \subset \mathbb{R}^2$ that is defined as the support of the image $f \in \mathbb{L}_2(\mathbb{R}^2)$ from which the features $\{c_p(f)\}_{p=1}^P, c_p(f) \in \mathbb{R}$ are extracted. Let the $\mathbb{L}_2(\Omega)$ -inner product on the domain $\Omega \subset \mathbb{R}^2$ for $f, g \in \mathbb{L}_2(\Omega)$ be given by

$$(f, g)_{\mathbb{L}_2(\Omega)} = \int_{\Omega} \overline{f(x)} g(x) dx . \quad (3.1)$$

A feature $c_p(f)$ is obtained by taking the inner product of the p^{th} filter

$\psi_p \in \mathbb{L}_2(\Omega)$ with the image $f \in \mathbb{L}_2(\Omega)$,

$$c_p(f) = (\psi_p, f)_{\mathbb{L}_2(\Omega)} . \quad (3.2)$$

We define an image $g \in \mathbb{L}_2(\Omega)$ to be equivalent to the image f if they share the same features, $\{c_p(f)\}_{p=1}^P = \{c_p(g)\}_{p=1}^P$, which is expressed in the following equivalence relation for $f, g \in \mathbb{L}_2(\Omega)$:

$$f \sim g \Leftrightarrow (\psi_p, f)_{\mathbb{L}_2(\Omega)} = (\psi_p, g)_{\mathbb{L}_2(\Omega)} \text{ for all } p = 1, \dots, P. \quad (3.3)$$

Next, we introduce the Sobolev space of order $2k$ on the domain Ω ,

$$\mathbb{H}^{2k}(\Omega) = \{f \in \mathbb{L}_2(\Omega) \mid |\Delta|^k f \in \mathbb{L}_2(\Omega)\} , \quad k > 0 . \quad (3.4)$$

The completion of the space of $2k$ -differentiable functions on the domain Ω that vanish on the boundary of its domain $\partial\Omega$ is given by

$$\mathbb{H}_0^{2k}(\Omega) = \{f \in \mathbb{H}^{2k}(\Omega) \mid f|_{\partial\Omega} = 0\} , \quad k > \frac{1}{2} . \quad (3.5)$$

Now $\mathbb{H}_0^{2k,\gamma}(\Omega)$ denotes the normed space obtained by endowing $\mathbb{H}_0^{2k}(\Omega)$ with the following inner product,

$$\begin{aligned} (f, g)_{\mathbb{H}_0^{2k,\gamma}(\Omega)} &= (f, g)_{\mathbb{L}_2(\Omega)} + \gamma^{2k} \left(|\Delta|^{\frac{k}{2}} f, |\Delta|^{\frac{k}{2}} g \right)_{\mathbb{L}_2(\Omega)} \\ &= (f, g)_{\mathbb{L}_2(\Omega)} + \gamma^{2k} \left(|\Delta|^k f, g \right)_{\mathbb{L}_2(\Omega)} , \end{aligned} \quad (3.6)$$

for all $f, g \in \mathbb{H}_0^{2k}(\Omega)$ and $\gamma \in \mathbb{R}^+$.

We want to find the solution to the reconstruction problem, which is the image g of minimal $\mathbb{H}_0^{2k,\gamma}$ -norm that shares the same features with the image $f \in \mathbb{H}_0^{2k,\gamma}(\Omega)$ from which the features $\{c_p(f)\}_{p=1}^P$ were extracted. The reconstructed image g is found by an orthogonal projection, within the space $\mathbb{H}_0^{2k,\gamma}(\Omega)$, of f onto the subspace V spanned by the filters κ_p that correspond to the ψ_p filters,

$$\arg \min_{g \sim f} \|g\|_{\mathbb{H}_0^{2k,\gamma}(\Omega)}^2 = \mathbb{P}_V f , \quad (3.7)$$

as shown in previous work [64]. The filters $\kappa_p \in \mathbb{H}_0^{2k,\gamma}(\Omega)$ are given by

$$\kappa_p = \left(I + \gamma^{2k} |\Delta|^k \right)^{-1} \psi_p . \quad (3.8)$$

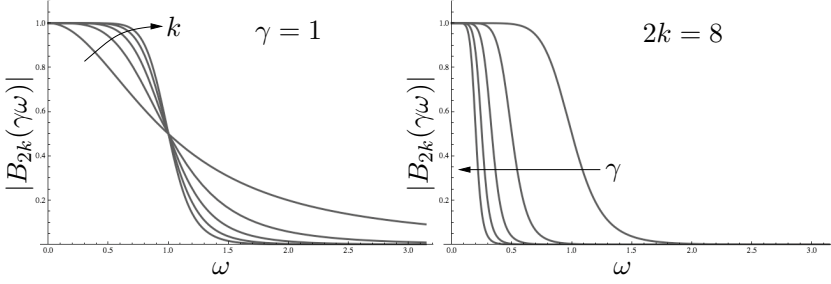


Figure 3.2: The filter response of a Butterworth filter, cf. eq. (3.11). On the left, γ is kept constant and the filter responses for different $k > 0$ are shown. On the right, the order of the filter, $2k$, is kept constant and the filter responses for different $\gamma > 0$ are shown.

As a consequence $(\kappa_p, f)_{\mathbb{H}_0^{2k, \gamma}(\Omega)} = (\psi_p, f)_{\mathbb{L}_2(\Omega)}$ for all f and $p = 1, \dots, P$. Here we assumed that $f \in \mathbb{H}^{2k}(\Omega)$. However, it suffices to take $f \in \mathbb{L}_2(\Omega)$ if ψ satisfies certain regularity conditions. The interested reader can find the precise conditions and further details in [35].

The two parameters γ and k that appear in the reconstruction problem, allow for an interesting interpretation. If $\Omega = \mathbb{R}$, the fractional operator $(I + \gamma^{2k}|\Delta|^k)^{-1}$ can be written as

$$(I + \gamma^{2k}|\Delta|^k)^{-1} f = \mathcal{F}^{-1} \left(\omega \mapsto (1 + \gamma^{2k}|\omega|^{2k})^{-1} (\mathcal{F}f)(\omega) \right) \quad (3.9)$$

for all $f \in \mathbb{H}^{2k}$ and $\omega \in \mathbb{R}$. Here $\mathcal{F} : \mathbb{L}_2(\mathbb{R}) \rightarrow \mathbb{L}_2(\mathbb{R})$ denotes Fourier transformation, which is defined almost everywhere as

$$(\mathcal{F}f)(\omega) = \frac{1}{\sqrt{2\pi}} \int_{-\infty}^{\infty} f(x) e^{-i\omega x} dx. \quad (3.10)$$

Therefore it is equivalent to filtering with the classical low-pass Butterworth filter [19] of order $2k$ and cut-off frequency $\omega_0 = \frac{1}{\gamma}$. The Fourier transform of this filter is defined as

$$B_{2k} \left(\frac{\omega}{\omega_0} \right) = \frac{1}{1 + \left| \frac{\omega}{\omega_0} \right|^{2k}}. \quad (3.11)$$

The filter response of the Butterworth filter is shown in Figure 3.2. One can observe the order of the filter controls how well the ideal low-pass filter is approximated and the effect of γ on the cut-off frequency.

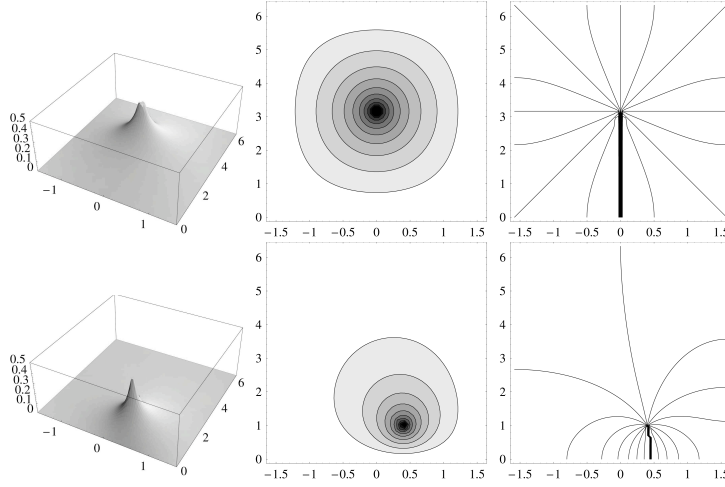


Figure 3.3: From left to right plots of the graph of $\mathbf{x} \mapsto G(\mathbf{x}, \mathbf{y})$, isocontours $\{\mathbf{x} \in \mathbb{R}^2 | G(\mathbf{x}, \mathbf{y}) = c\}$ for various $c > 0$, and isocontours of its Harmonic conjugate $H(\mathbf{x}, \mathbf{y}) = \frac{-1}{2\pi} \arg \left(\frac{\text{sn}(x_1 + ix_2, \tilde{k}) - \text{sn}(y_1 + iy_2, \tilde{k})}{\text{sn}(x_1 + ix_2, \tilde{k}) - \text{sn}(y_1 + iy_2, \tilde{k})} \right)$; x_1 runs along the horizontal axis whereas x_2 runs along the vertical axis. In the upper row $(y_1, y_2) = (0, \pi)$, and in the bottom row $(y_1, y_2) = (1, 0.4)$. To keep $\log(z) = \log(|z|) + i \arg(z) = \int_1^z \frac{1}{\xi} d\xi$ single valued, we apply a branch-cut on the negative real axis. The thick lines in the $x_1 x_2$ -plane are mapped to the negative real axis, so here the graph of $H(\cdot, \mathbf{y})$ is discontinuous (the graph has a jump).

3.2.1 Spectral Decomposition

In this section we set $k = 1$ and investigate the Laplace operator on the bounded domain: $\Delta : \mathbb{H}_0^2(\Omega) \rightarrow \mathbb{L}_2(\Omega)$. This is a bounded operator, since $\|\Delta f\|_{\mathbb{L}_2(\Omega)} \leq 1 \|f\|_{\mathbb{H}_0^2(\Omega)}$ for all $f \in \mathbb{H}_0^2(\Omega)$, and its right inverse is given by the minus Dirichlet operator:

Definition 5 (Dirichlet Operator). *The Dirichlet operator \mathcal{D} is given by*

$$g = \mathcal{D}f \Leftrightarrow \begin{cases} \Delta g = -f \\ g|_{\partial\Omega} = 0 \end{cases} \quad (3.12)$$

with $f \in \mathbb{L}_2(\Omega)$ and $g \in \mathbb{H}_0^2(\Omega)$.

The Green's function $G : \Omega \times \Omega \rightarrow \mathbb{R}$ of the Dirichlet operator is given by

$$\begin{cases} \Delta G(\mathbf{x}, \cdot) = -\delta_{\mathbf{x}} \\ G(\mathbf{x}, \cdot)|_{\partial\Omega} = 0 \end{cases} \quad (3.13)$$

for fixed $\mathbf{x} \in \Omega$. On the domain¹ $\Omega = [-a, a] \times [0, b]$ the closed form solution is given by² (see Appendix B.1)

$$G_{a,b}(\mathbf{x}, \mathbf{y}) = -\frac{1}{2\pi} \log \left| \frac{\operatorname{sn}(x_1 \frac{z(1, \tilde{k})}{a} + i x_2 \frac{z(1, \sqrt{1-\tilde{k}^2})}{b}, \tilde{k}) - \operatorname{sn}(y_1 \frac{z(1, \tilde{k})}{a} + i y_2 \frac{z(1, \sqrt{1-\tilde{k}^2})}{b}, \tilde{k})}{\operatorname{sn}(x_1 \frac{z(1, \tilde{k})}{a} + i x_2 \frac{z(1, \sqrt{1-\tilde{k}^2})}{b}, \tilde{k}) - \operatorname{sn}(y_1 \frac{z(1, \tilde{k})}{a} + i y_2 \frac{z(1, \sqrt{1-\tilde{k}^2})}{b}, \tilde{k})} \right|. \quad (3.14)$$

Here $\mathbf{x} = (x_1, x_2), \mathbf{y} = (y_1, y_2) \in \Omega$, $\tilde{k} \in \mathbb{R}$ is determined by the aspect ratio of the rectangular domain Ω , sn denotes the Jacobi-elliptic function [52], [117, Chapter XXII], and

$$z(1, \tilde{k}) = \int_0^1 \frac{dt}{\sqrt{1-t^2} \sqrt{1-\tilde{k}^2 t^2}}. \quad (3.15)$$

In Appendix B.1 we derive eq. (3.14), and show how to obtain \tilde{k} . Figure 3.3 shows a graphical representation of this non-isotropic Green's function for a square domain ($\tilde{k} \approx 0.1716$). Notice this function vanishes at its boundaries and is, in the center of the domain, very similar to the isotropic fundamental solution on the unbounded domain [33, 85]. In Appendix B.2 we put a relation between the fundamental solution of the Laplace operator on the unbounded domain and the Green's function on the bounded domain with Dirichlet boundary conditions. In terms of regularization this means the Dirichlet operator smoothes inwards the image but never “spills” over the border of the domain Ω .

When the Dirichlet operator, as defined in Definition 5, is expressed by means of its Green's function, which is presented in eq. (3.14),

$$(\mathcal{D}f)(\mathbf{x}) = \int_{\Omega} G(\mathbf{x}, \mathbf{y}) f(\mathbf{y}) d\mathbf{y}, \quad f \in \mathbb{L}_2(\Omega), \quad \mathcal{D}f \in \mathbb{H}_0^2(\Omega) \quad (3.16)$$

¹This domain is chosen in order to simplify the notation in Appendix B.1, where conformal mapping is used to obtain eq. (3.14).

²Our solution is a generalization of the solution derived by Boersma et al. in [13].

one can verify it extends to a compact, self-adjoint operator on $\mathbb{L}_2(\Omega)$. As a consequence, by the spectral decomposition theorem of compact self-adjoint operators [121], we can express the Dirichlet operator in an orthonormal basis of eigenfunctions. The normalized eigenfunctions f_{mn} with corresponding eigenvalues λ_{mn} of the Laplace operator $\Delta : \mathbb{H}_0^2(\Omega) \rightarrow \mathbb{L}_2(\Omega)$ are given by

$$f_{mn}(x, y) = \sqrt{\frac{1}{ab}} \sin\left(\frac{n\pi x}{a}\right) \sin\left(\frac{m\pi y}{b}\right) \quad (3.17)$$

$$\lambda_{mn} = - \left(\left(\frac{n\pi}{a} \right)^2 + \left(\frac{m\pi}{b} \right)^2 \right), \quad (3.18)$$

$(x, y) \in \Omega$ with $\Omega = [0, a] \times [0, b]^3$ and $m, n \in \mathbb{N}$. These functions can be found by the method of separation, [75]. Since $\Delta \mathcal{D} = -I$, the eigenfunctions of the Dirichlet operator coincide with those of the Laplace operator, eq. (3.17), and its corresponding eigenvalues are the inverse of the eigenvalues of the Laplace operator, eq. (3.18).

3.2.2 Scale Space on the Bounded Domain

The spectral decomposition which is presented in the previous subsection by eqs. (3.17) and (3.18), will now be applied to the construction of a scale space on the bounded domain. We will follow the second author's previous work [37] on scale spaces on the bounded domain. Here we recall from [37] that Neumann boundary conditions are required in order to maintain most scale space axioms, [38]. However, here we shall first consider Dirichlet boundary conditions. In Section 3.2.4 we will also consider Neumann boundary conditions. Before we show how to obtain a Gaussian scale space representation of an image on the bounded domain we find, as suggested by Koenderink [74], the image $h \in \mathbb{H}^2(\Omega)$ which is the harmonic extension of $f|_{\partial\Omega}$. So it is the solution to

$$\begin{cases} \Delta h(x, y) = 0 & \text{for all } x, y \in \Omega \\ h(x, y) = f(x, y) & \text{for all } x, y \in \partial\Omega \end{cases} \quad (3.19)$$

Now $\tilde{f} = f - h$ vanishes at the boundary $\partial\Omega$ (so this requires Dirichlet boundary conditions in scale space) and can serve as an initial condition

³This domain is chosen in order to facilitate the readability of the notation of the spectral decomposition.

for the heat equation on the bounded domain. A practical method for obtaining h on an arbitrarily shaped domain, is suggested by Georgiev [50] and a fast method on a rectangular domain is proposed by Averbuch et al. [5]. Now \tilde{f} can be expressed in the orthogonal basis:

$$\tilde{f} = \sum_{m,n \in \mathbb{N}} (f_{mn}, \tilde{f})_{\mathbb{L}_2(\Omega)} f_{mn} , \quad (3.20)$$

which effectively exploits the sine transform.

The (fractional) operators that will appear in the construction of a Gaussian scale space on the bounded domain can be expressed as

$$|\Delta|^k f_{mn} = |\lambda_{mn}|^k f_{mn} , \quad (3.21)$$

$$e^{-s|\Delta|} f_{mn} = e^{s\lambda_{mn}} f_{mn} . \quad (3.22)$$

We also note that the κ_p filters, defined in eq. (3.8), are readily obtained by application of the following identity

$$\left(I + \gamma^{2k} |\Delta|^k \right)^{-1} f_{mn} = \frac{1}{1 + \gamma^{2k} |\lambda_{mn}|^k} f_{mn} . \quad (3.23)$$

Consider the Gaussian scale space representation⁴ on bounded domain Ω (see [37])

$$u_{\tilde{f}}^{\Omega}(x, y, s) = \sum_{m,n \in \mathbb{N}} e^{s\lambda_{mn}} (f_{mn}, \tilde{f})_{\mathbb{L}_2(\Omega)} f_{mn}(x, y) \quad (3.24)$$

where the scale parameter $s \in \mathbb{R}^+$. It is the unique solution to

$$\begin{cases} \frac{\partial u}{\partial s} = \Delta u \\ u(\cdot, s)|_{\partial\Omega} = 0 \text{ for all } s > 0 \\ u(\cdot, 0) = \tilde{f} \end{cases} . \quad (3.25)$$

By straightforward computation one has

$$\begin{aligned} \Delta u_{\tilde{f}}^{\Omega}(x, y, s) &= \sum_{m,n \in \mathbb{N}} e^{s\lambda_{mn}} (f_{mn}, \tilde{f})_{\mathbb{L}_2(\Omega)} \Delta f_{mn}(x, y) \\ &= \sum_{m,n \in \mathbb{N}} \lambda_{mn} e^{s\lambda_{mn}} (f_{mn}, \tilde{f})_{\mathbb{L}_2(\Omega)} f_{mn}(x, y) \\ &= \partial_s \sum_{m,n \in \mathbb{N}} e^{s\lambda_{mn}} (f_{mn}, \tilde{f})_{\mathbb{L}_2(\Omega)} f_{mn}(x, y) \\ &= \partial_s u_{\tilde{f}}^{\Omega}(x, y, s) . \end{aligned} \quad (3.26)$$

⁴The framework in this paper is readily generalized to α -scale spaces in general (see, e.g., [37]) by replacing $(-\lambda_{mn})$ by $(-\lambda_{mn})^{2\alpha}$.

The filter ϕ_p that measures differential structure present in the scale space representation $u_{\tilde{f}}^\Omega$ of \tilde{f} at a point p with coordinates (x_p, y_p, s_p) , such that

$$\left(D^{\mathbf{n}_p} u_{\tilde{f}}^\Omega\right)(x_p, y_p, s_p) = \left(\phi_p, \tilde{f}\right)_{\mathbb{L}_2(\Omega)} , \quad (3.27)$$

is given by (writing multi-index $\mathbf{n}_p = (n_p^1, n_p^2)$)

$$\phi_p(x, y) = \sum_{m, n \in \mathbb{N}} e^{s_p \lambda_{mn}} (D^{\mathbf{n}_p} f_{mn})(x_p, y_p) f_{mn}(x, y) , \quad (3.28)$$

where we note that $\frac{d}{dx} \sin(x) = \cos(x) = \sin(x + \frac{\pi}{2})$ and

$$\begin{aligned} (D^{\mathbf{n}_p} f_{mn})(x_p, y_p) &= \sqrt{\frac{1}{ab}} \left(\frac{m\pi}{b}\right)^{n_p^2} \left(\frac{n\pi}{a}\right)^{n_p^1} \sin\left(\frac{m\pi y_p}{b} + \frac{\pi}{2} n_p^2\right) \\ &\quad \sin\left(\frac{n\pi x_p}{a} + \frac{\pi}{2} n_p^1\right) , \end{aligned} \quad (3.29)$$

$\mathbf{x} = (x, y) \in \Omega$, $\mathbf{x}_p = (x_p, y_p) \in \Omega$ and $\mathbf{n}_p = (n_p^1, n_p^2) \in \mathbb{N} \times \mathbb{N}$. Here we use notation ϕ_p for the filters that measure features of the type presented in eq. (3.27). However, we stress that this is just one particular case of the filters ψ_p that are used to measure the general features, cf. eq. (3.2).

3.2.3 The Solution to the Reconstruction Problem

Now that we have constructed a scale space on the bounded domain and shown how to measure its differential structure we can express the solution to the reconstruction problem (recall eqs. (3.7) and (3.8)) in terms of eigenfunctions and eigenvalues of the Laplace operator. To this end we recall that $V = \text{span}\{\kappa_q | q \in 1, \dots, P\}$ and we apply the orthogonal projection operator $\mathbb{P}_V : \mathbb{H}_0^{2k, \gamma}(\Omega) \rightarrow V$ to \tilde{f} :

$$\begin{aligned} \mathbb{P}_V \tilde{f} &= \sum_{p, q=1}^P G^{pq}(\kappa_p, \tilde{f})_{\mathbb{H}_0^{2k}(\Omega)} \kappa_q \\ &= \sum_{p, q=1}^P G^{pq}(\phi_p, \tilde{f})_{\mathbb{L}_2(\Omega)} \kappa_q \\ &= \sum_{p, q=1}^P G^{pq} c_p(\tilde{f}) \kappa_q , \end{aligned} \quad (3.30)$$

where G^{pq} are components of the inverse of the Gram matrix. This implies $G^{pr}G_{rq} = \delta_q^p$, with $G_{pq} = (\kappa_p, \kappa_q)_{\mathbb{H}_0^{2k, \gamma}(\Omega)}$. The filters κ_p satisfy

$$\kappa_p(x, y) = \sum_{m, n \in \mathbb{N}} \frac{e^{s_p \lambda_{mn}}}{1 + \gamma^{2k} |\lambda_{mn}|^k} (D^{\mathbf{n}_p} f_{mn})(x_p, y_p) f_{mn}(x, y) . \quad (3.31)$$

It can indeed be verified by direct computation that

$$\mathbb{P}_V^2 = \mathbb{P}_V , \quad \mathbb{P}_V^* = \mathbb{P}_V , \quad \mathcal{R}(\mathbb{P}_V) = V , \quad (3.32)$$

so \mathbb{P}_V is indeed the orthogonal projection onto V . The projection that is made explicit in eq. (3.30) is, due to the Pythagoras theorem, the unique solution to the optimization problem

$$\arg \min_{g \sim \tilde{f}} \|g\|_{\mathbb{H}_0^{2k, \gamma}(\Omega)}^2 = \arg \min_{g \sim \tilde{f}} \underbrace{\|g - \mathbb{P}_V \tilde{f}\|_{\mathbb{H}_0^{2k, \gamma}(\Omega)}^2}_{\in V^\perp} + \underbrace{\|\mathbb{P}_V \tilde{f}\|_{\mathbb{H}_0^{2k, \gamma}(\Omega)}^2}_{\in V} , \quad (3.33)$$

which was introduced in eq. (3.7).

In order to compute the projection in eq. (3.30) we apply a *singular value decomposition* (SVD) [94, Chapter 2.9] to guarantee well-posedness of our algorithm. We briefly outline the application of the SVD to the projection in eq. (3.30). Let the columns of the matrix \hat{V} be composed of the eigenvectors $\{\mathbf{v}_i\}_{i=1}^P$ of $G^T G$, where $G = [G_{pq}]_{p,q=1}^P$, with corresponding eigenvalues σ_i^2 , ($\sigma_1 > \sigma_2 > \dots$). We define $D = \text{diag}\{\sigma_i\}$ and $U = G \hat{V} D^{-1}$. This implies $U^T = U^{-1}$ and $(G^T G)^{-1} G^T = \hat{V} D^{-1} U^T$, from which we deduce that

$$\mathbb{P}_V \tilde{f} = \sum_{q=1}^P \sum_{i \in I} \left(\sum_{p=1}^P \frac{u_i^p c_p(\tilde{f})}{\sigma_i} \right) v_i^q \kappa_q \quad (3.34)$$

with \mathbf{u}_i the i^{th} column of U and u_i^p the p^{th} element of the vector \mathbf{u}_i . The set I is defined as $I = \{i \in 1 \dots P \mid \frac{\sigma_i}{\sigma_1} \geq \text{tolerance}\}$, thus directions corresponding to eigenvalues σ_i such that $\frac{\sigma_i}{\sigma_1}$ is smaller than a given tolerance are removed from the projection.

3.2.4 Neumann Boundary Conditions

The axioms that naturally lead to α -scale spaces [38] cannot all be maintained in case of the bounded domain. One has to drop the axiom of

translation invariance. This can be observed from Figure 3.3: the Green's function of the Laplace operator on the bounded domain deforms when it is moved closer to the boundary. In order to maintain the other axioms such as gray value invariance and increase of entropy, Neumann boundary conditions should be chosen [37]. Imposing zero Neumann boundary conditions coincides with the symmetric extension of the image at the boundaries and periodic boundary conditions on the extended domain. In this case the eigenvalues λ_{mn} (3.18) are maintained, the eigenfunctions are given by

$$f_{mn}(x, y) = \sqrt{\frac{1}{ab(1 + \delta_{m0})(1 + \delta_{n0})}} \cos\left(\frac{n\pi x}{a}\right) \cos\left(\frac{m\pi y}{b}\right), \quad (3.35)$$

where $m, n \in \mathbb{N}$. We note that again:

$$|\Delta|^k f_{mn} = |\lambda_{mn}|^k f_{mn}. \quad (3.36)$$

When the eigenfunctions in eq. (3.24) are replaced by the eigenfunctions in eq. (3.35), eq. (3.24) is the unique solution to the heat equation

$$\begin{cases} \frac{\partial u}{\partial s} = \Delta u \\ \frac{\partial u(\cdot, s)}{\partial \mathbf{n}}|_{\partial\Omega} = 0 \text{ for all } s > 0 \\ u(\cdot, 0) = \tilde{f} \end{cases}, \quad (3.37)$$

where \mathbf{n} is the outward normal of the image boundary $\partial\Omega$.

When Neumann boundary conditions other than zero are required, we proceed in a similar fashion as proposed in Section 3.2.2. In this case, however, we have to take care that Green's second identity,

$$\int_{\Omega} (h\Delta f - f\Delta h) d\mathbf{x} = \int_{\partial\Omega} \left(h \frac{\partial f}{\partial \mathbf{n}} - f \frac{\partial h}{\partial \mathbf{n}} \right) d\sigma(\mathbf{x}) \quad (3.38)$$

with $d\sigma(\mathbf{x})$ a boundary measure and $\mathbf{x} \in \Omega$, is not violated. As a consequence, we cannot find an $h \in \mathbb{H}^2(\Omega)$ such that

$$\begin{cases} \Delta h = 0 \\ \frac{\partial h}{\partial \mathbf{n}}|_{\partial\Omega} = \frac{\partial f}{\partial \mathbf{n}} \end{cases}, \quad (3.39)$$

holds, since

$$\int_{\Omega} \Delta h d\mathbf{x} = \int_{\partial\Omega} \frac{\partial h}{\partial \mathbf{n}} d\sigma(\mathbf{x}) = \int_{\partial\Omega} \frac{\partial f}{\partial \mathbf{n}} d\sigma(\mathbf{x}). \quad (3.40)$$

In order to solve this problem we introduce a constant source term in (3.39) and find instead an h such that

$$\begin{cases} \Delta h = K \\ \frac{\partial h}{\partial \mathbf{n}}|_{\partial\Omega} = \frac{\partial f}{\partial \mathbf{n}} \end{cases}, \quad (3.41)$$

with $K = \frac{1}{|\Omega|} \int_{\partial\Omega} \frac{\partial f}{\partial \mathbf{n}} d\sigma(\mathbf{x})$ and $|\Omega|$ the area of the domain. An efficient method to solve h from eq. (3.41) based on the method by Averbuch [5] can be found in [120]. Now $\tilde{f} = f - h$ has zero normal derivatives at the boundary $\partial\Omega$ and can serve as an initial condition for the heat equation that is presented in eq. (3.37).

3.2.5 Singular Points

The theory presented in the previous subsections is applicable to generic linear features, cf. eq. (3.2). In Section 3.4 we will apply our reconstruction method to image reconstruction from differential properties of so called singular points of a scale space representation of an image. Therefore we will briefly summarize how to obtain the locations of these points. A non-Morse critical point of a scale space representation of an image, to which we will henceforth refer to as a singular point, is defined as follows:

Definition 6 (Singular Point). *A singular point $(x, y, s) \in \mathbb{R}^2 \times \mathbb{R}^+$ of a scale space representation $u_f^\Omega(x, y, s)$ of the image f is defined by the following equations, in which ∇ denotes the spatial gradient operator:*

$$\begin{cases} \nabla u_f^\Omega(x, y, s) = 0 \\ \det \nabla \nabla^T u_f^\Omega(x, y, s) = 0. \end{cases} \quad (3.42)$$

See [26, 44] for further details, and [51] for a general introduction to catastrophe theory. Figure 3.4 illustrates the set of singular points for a typical image. Solutions of eq. (3.42) can be found by a zero-crossings method [81, 69]. Given an initial approximate location of a singular point, (x_a, y_a, s_a) , we can refine its position in scale space to a corrected position, (x_c, y_c, s_c) , by calculating $(x_c, y_c, s_c) = (x_a + \delta x, y_a + \delta y, s_a + \delta s)$, where

$$\begin{bmatrix} \delta x \\ \delta y \\ \delta s \end{bmatrix} = (\mathbf{M}(x_a, y_a, s_a))^{-1} \begin{bmatrix} \mathbf{g}(x_a, y_a, s_a) \\ (\det \nabla \nabla^T u_f^\Omega)(x_a, y_a, s_a) \end{bmatrix}, \quad (3.43)$$

and where

$$\mathbf{M} = \begin{bmatrix} \nabla \nabla^T u_f^\Omega & \mathbf{w} \\ \mathbf{z}^T & c \end{bmatrix}, \quad (3.44)$$

$$\mathbf{g}(x, y, s) = \nabla u_f^\Omega(x, y, s), \quad \mathbf{w} = \partial_s \mathbf{g}, \quad (3.45)$$

$$\mathbf{z}(x, y, s) = \nabla \det \nabla \nabla^T u_f^\Omega(x, y, s), \quad c(x, y, s) = \partial_s \det \nabla \nabla^T u_f^\Omega(x, y, s). \quad (3.46)$$

Notice that all derivatives are taken in the point (x_a, y_a, s_a) . This procedure is repeated in order to obtain a more accurate location of a singular point. For further details we refer to [44, 92]. In general, images are not determined by their singular points. Consider for example the class of images

$$f(x, y) = f_{mn}(x, y), \quad (3.47)$$

whose bounded domain scale space representations are given by

$$u_f^\Omega(x, y, s) = e^{s\lambda_{mn}} f_{mn}(x, y). \quad (3.48)$$

These scale space representations do not contain any singular points. However, scale space representations of natural images do contain singular points attached to generic topological transitions [26]. If one endows these points with suitable attributes one can obtain a reconstruction that is visually close to the initial image [64].

3.3 Implementation

The implementation of the reconstruction method that was presented in a continuous Hilbert space framework is completely performed in a discrete framework in order to avoid approximation and truncation errors due to sampling. Here we shall make use of a *discrete* sine transform (rather than truncated Fourier series) and its inverse, which are exact on the grid.

First we introduce the discrete sine transform $\mathcal{F}_S : \mathfrak{l}_2(I_N^{\mathcal{D}}) \rightarrow \mathfrak{l}_2(I_N^{\mathcal{D}})$ on a rectangular domain $I_N^{\mathcal{D}} = \{1, \dots, N-1\} \times \{1, \dots, M-1\}$

$$(\mathcal{F}_S f)(u, v) = -\frac{2}{\sqrt{MN}} \sum_{i=1}^{M-1} \sum_{j=1}^{N-1} \underbrace{\sin\left(\frac{iu\pi}{M}\right) \sin\left(\frac{jv\pi}{N}\right)}_{(\varphi_i \otimes \varphi_j)(u, v)} f(i, j), \quad (3.49)$$

with $(u, v) \in I_N^{\mathcal{D}}$. Notice that this unitary transform is its own inverse and that

$$(\varphi_i, \varphi_j)_{l_2(I_N^{\mathcal{D}})} = \delta_{ij} , \quad (3.50)$$

so $\{\varphi_i \otimes \varphi_j \mid \begin{smallmatrix} i = 1, \dots, M-1 \\ j = 1, \dots, N-1 \end{smallmatrix}\}$ forms an orthonormal basis in $l_2(I_N^{\mathcal{D}})$.

The Gaussian scale space representation $u_f^{I_N^{\mathcal{D}}}(i, j, s)$ of an image $f \in l_2(I_N^{\mathcal{D}})$ introduced in the continuous domain in eq. (3.24) now reads

$$\begin{aligned} u_f^{I_N^{\mathcal{D}}}(i, j, s) &= \left(e^{s\Delta} f \right) (i, j) \\ &= -\frac{2}{\sqrt{MN}} \sum_{u=1}^{M-1} \sum_{v=1}^{N-1} \hat{f}(u, v) e^{-s \left(\frac{u^2}{M^2} + \frac{v^2}{N^2} \right) \pi^2} (\varphi_u \otimes \varphi_v) (i, j) \end{aligned} \quad (3.51)$$

where $\hat{f}(u, v) = (\mathcal{F}_S f)(u, v)$. Differential structure of order $\mathbf{n}_p = (n_p^1, n_p^2) \in \mathbb{N} \times \mathbb{N}$ at a certain position $(i_p, j_p) \in I_N^{\mathcal{D}}$ and at scale $s_p \in \mathbb{R}^+$ is measured by

$$\begin{aligned} \left(D^{\mathbf{n}_p} u_f^{I_N^{\mathcal{D}}} \right) (i_p, j_p, s_p) &= -\frac{2}{\sqrt{MN}} \sum_{u=1}^{M-1} \sum_{v=1}^{N-1} \hat{f}(u, v) e^{-s_p \left(\frac{u^2}{M^2} + \frac{v^2}{N^2} \right) \pi^2} \\ &\quad \left(\frac{u\pi}{M} \right)^{n_p^1} \left(\frac{v\pi}{N} \right)^{n_p^2} \sin \left(\frac{i_p u \pi}{M} + \frac{\pi}{2} n_p^1 \right) \sin \left(\frac{j_p v \pi}{N} + \frac{\pi}{2} n_p^2 \right) . \end{aligned} \quad (3.52)$$

The filters ϕ_p , with $p = (i_p, j_p, s_p, \mathbf{n}_p)$ a multi-index, are given by

$$\begin{aligned} \phi_p(i, j, s) &= -\frac{2}{\sqrt{MN}} \sum_{u=1}^{M-1} \sum_{v=1}^{N-1} e^{-s_p \left(\frac{u^2}{M^2} + \frac{v^2}{N^2} \right) \pi^2} (\varphi_u \otimes \varphi_v) (i, j) \\ &\quad \left(\frac{u\pi}{M} \right)^{n_p^1} \left(\frac{v\pi}{N} \right)^{n_p^2} \sin \left(\frac{i_p u \pi}{M} + \frac{\pi}{2} n_p^1 \right) \sin \left(\frac{j_p v \pi}{N} + \frac{\pi}{2} n_p^2 \right) \end{aligned} \quad (3.53)$$

and the filters κ_p corresponding to ϕ_p read

$$\begin{aligned} \kappa_p(i, j, s) &= -\frac{2}{\sqrt{MN}} \sum_{u=1}^{M-1} \sum_{v=1}^{N-1} \frac{e^{-s_p \left(\frac{u^2}{M^2} + \frac{v^2}{N^2} \right) \pi^2}}{1 + (\pi\gamma)^{2k} \left(\frac{u^2}{M^2} + \frac{v^2}{N^2} \right)^k} (\varphi_u \otimes \varphi_v) (i, j) \\ &\quad \left(\frac{u\pi}{M} \right)^{n_p^1} \left(\frac{v\pi}{N} \right)^{n_p^2} \sin \left(\frac{i_p u \pi}{M} + \frac{\pi}{2} n_p^1 \right) \sin \left(\frac{j_p v \pi}{N} + \frac{\pi}{2} n_p^2 \right) . \end{aligned} \quad (3.54)$$

An element $G_{pq} = (\phi_p, \phi_q)_{l_2(I_N^D)}$ of the Gram matrix can, because of the orthonormality of the transform, be expressed in just a double sum,

$$G_{pq} = -\frac{2}{\sqrt{MN}} \sum_{u=1}^{M-1} \sum_{v=1}^{N-1} \frac{e^{-(s_p+s_q)\left(\frac{u^2}{M^2} + \frac{v^2}{N^2}\right)\pi^2}}{1 + (\pi\gamma)^{2k} \left(\frac{u^2}{M^2} + \frac{v^2}{N^2}\right)^k} \quad (3.55)$$

$$\left(\frac{u\pi}{M}\right)^{n_p^1} \left(\frac{v\pi}{N}\right)^{n_p^2} \sin\left(\frac{i_p u \pi}{M} + \frac{\pi}{2} n_p^1\right) \sin\left(\frac{j_p v \pi}{N} + \frac{\pi}{2} n_p^2\right)$$

$$\left(\frac{u\pi}{M}\right)^{n_q^1} \left(\frac{v\pi}{N}\right)^{n_q^2} \sin\left(\frac{i_q u \pi}{M} + \frac{\pi}{2} n_q^1\right) \sin\left(\frac{j_q v \pi}{N} + \frac{\pi}{2} n_q^2\right) .$$

In order to gain accuracy we implement eq. (3.55) by summing in the reverse direction and multiplying by γ^{2k} . Then we compute

$$\tilde{g} = \sum_{p,q=1}^P G^{pq} \gamma^{2k} c_p(f) \phi_q \quad (3.56)$$

and find the reconstructed image g by filtering \tilde{g} by a discrete version of the 2D Butterworth filter of order $2k$ and with cut-off frequency $\omega_0 = \frac{1}{\gamma}$.

The implementation was written using the sine transform as defined in eq. (3.49) where we already explicitly mentioned that the transform can be written as

$$(\mathcal{F}_S f)(u, v) = -\frac{2}{\sqrt{MN}} \sum_{i=1}^{M-1} \sum_{j=1}^{N-1} (\varphi_i \otimes \varphi_j)(u, v) f(i, j) . \quad (3.57)$$

Now we define the cosine transform, $\mathcal{F}_S : l_2(I_N^N) \rightarrow l_2(I_N^N)$, on a rectangular domain, $I_N^N = \{0, \dots, N-1\} \times \{0, \dots, M-1\}$, in a similar manner

$$(\mathcal{F}_C f)(u, v) = \sum_{i=0}^{M-1} \sum_{j=0}^{N-1} (\tilde{\varphi}_i \otimes \tilde{\varphi}_j)(u, v) f(i, j) , \quad (3.58)$$

where

$$(\tilde{\varphi}_i \otimes \tilde{\varphi}_j)(u, v) = \cos\left(\frac{\pi(i + \frac{1}{2})u}{M}\right) \sqrt{\frac{2 - \delta_{u0}}{M}} \cos\left(\frac{\pi(j + \frac{1}{2})v}{N}\right) \sqrt{\frac{2 - \delta_{v0}}{N}} \quad (3.59)$$

and $(u, v) \in I_N^N$. These cosine basis functions $\{\tilde{\varphi}_i \otimes \tilde{\varphi}_j \mid \begin{smallmatrix} i = 0, \dots, M-1 \\ j = 0, \dots, N-1 \end{smallmatrix}\}$ form an orthogonal basis in $l_2(I_N^N)$ and can thus be used to transform the reconstruction method that was explicitly presented for the Dirichlet case into a reconstruction method based on Neumann boundary conditions.

3.4 Experiments

We evaluate the reconstruction method by applying it to the problem that was presented in the introduction. The upper row of Figure 3.5 shows from left to right: the image from which the features were extracted, a reconstruction by the unbounded domain method [64] (parameters: $\gamma = 50, k = 1$), and a reconstruction by the newly introduced bounded domain method using Dirichlet boundary conditions (parameters: $\gamma = 50, k = 1$). Features that were used are up to second order derivatives measured at the singular points (see Section 3.2.5) of the scale space representation of the original image f . One can clearly see that the structure that is missing in the middle image (cf. Figure 3.1) does appear when the bounded domain method is used (top-right image in Figure 3.5).

The visual quality of the reconstruction in the top-right image in Figure 3.5 is not appealing. In order to obtain a visually more appealing reconstruction one could, like in our previous work on image reconstruction [64], endow the feature points with higher order differential structure. Another possibility is to select a different set of features. We proceed with the latter approach.

Singular points of a scale space representation of an image tend to catch blob-like structures, whereas singular points of the scale space representation of the Laplacian of an image (henceforth called Laplacian singular points) are more likely to catch information about edges and ridges in the image. This is so because the Laplacian tends to act as an edge detector. Furthermore, the number of singular points that manifest themselves in the scale space of an image is much smaller than the number of Laplacian singular points of an image. If more information about the image is used by the reconstruction algorithm, e.g., in the form of more features, one can expect to obtain a more appealing reconstruction. This motivates us to reconstruct from the properties of Laplacian singular points instead of singular points.

The bottom row of Figure 3.5 shows reconstructions from up to second order differential structure obtained from the scale space representation of f , evaluated at the locations of the singular points of the scale space representation of the Laplacian of f . On the left the unbounded domain method was used with $\gamma = 100$ and $k = 1$, this leads to a reconstructed signal that has “spilled” too much over the border of the image and therefore is not as

sharp as the reconstruction obtained by our newly proposed method using Dirichlet boundary conditions (parameters: $\gamma = 100$ and $k = 1$). Due to this spilling, the Gram matrix of the unbounded domain reconstruction method is harder to invert since basis functions start to become more and more dependent. This problem gets worse when γ increases. Our bounded domain method is immune to this problem as long as the parameter k is not chosen too high.

In order to quantify the observation that the Gram matrix is harder to invert when γ gets larger, we applied both the reconstruction method presented in this paper and the unbounded domain method [64] to the reconstruction from up to second order derivatives measured at the singular points of the scale space representation of Lena’s eye. Lena’s eye is the left-most image in Figure 3.6 and has dimensions of 64×64 pixels. We fixed $k = 1$ and set the tolerance of the *singular value decomposition* (SVD) algorithm that was used to compute the inverse of the Gram matrix (see Section 3.2.3, eq. (3.34)) to 10^{-7} . The percentage of features that were removed by the SVD algorithm as a function of γ is displayed in Figure 3.7. From this figure we can observe that the unbounded domain method breaks down for $\gamma \gg 0$, whereas the method that is presented in this paper is much more robust. Even for $\gamma \gg 0$ barely any features are removed by the thresholding step in the SVD algorithm.

If the order of the Sobolev space k is chosen too high, our method also breaks down. Figure 3.8 shows several reconstructions from up to second order differential structure taken at the locations of the singular points of Barbara’s face using Dirichlet boundary conditions. The image from which the features were obtained is the right-most image in Figure 3.6 and has dimensions of 128×128 pixels. From top to bottom the parameter $k = \{0.5 + \epsilon, 1.0, 1.5, 2.0, 2.5\}$ (introduced in eq. (3.4)), which controls the order of the Sobolev space we are projecting in is varied. From left to right the parameter $\gamma = \{1, 4, 16, 64, 256, 1024\}$ (introduced in eq. (3.6)), which controls the importance of smoothness is varied. One can clearly see the effect of the parameters. We will interpret the results in terms of the low-pass Butterworth filter introduced in eq. (3.11). When k is increased the order of the filter increases and consequently approximates the ideal low-pass filter more closely. In the bottom row of Figure 3.8 ($k=2.5$) the filter is too sharp (i.e., it approximates the ideal low-pass filter too closely) which results in a reconstruction that does not satisfy all features. This effect is even visible when $\gamma = 1$. Increasing γ corresponds to decreasing the cut-off frequency of the filter, which smoothes the “bumpy”

features that are most apparent in the top-most sub-images of Figure 3.8. If $k = 1$ increasing γ does not cause problems for the inversion of the Gram matrix (and consequent loss of features). This can also be observed from Figure 3.7. It does have a smoothing effect on the reconstructed image. Therefore it is preferred to use a $\gamma \gg 0$.

3.5 Conclusion

In previous work we considered the image as compactly supported in $\mathbb{L}_2(\mathbb{R}^2)$ and we used Sobolev norms on the unbounded domain including a smoothing parameter $\gamma > 0$ to tune the smoothness of the reconstructed image. Due to the assumption of compact support of the original image components of the reconstructed image near the image boundary are too much penalized. Therefore we proposed to minimize Sobolev norms only on the actual image domain, yielding much better reconstructions (especially for $\gamma \gg 0$). We give a closed form expression for the Green's function of the Dirichlet operator in the spatial domain and put a relation between the fundamental solution of the Laplace operator on the unbounded domain and the Green's function on the bounded domain with Dirichlet conditions. Both feature extraction and the reconstruction method are formulated on the bounded domain in terms of the eigenfunctions and corresponding eigenvalues of the Laplace operator on the bounded domain: $\Delta : \mathbb{H}_0^2(\Omega) \rightarrow \mathbb{L}_2(\Omega)$. By changing the eigenfunctions the Dirichlet boundary conditions can be interchanged with Neumann boundary conditions. The implementation is done completely in the discrete domain and is exact on the grid, avoiding truncation or approximation errors. This is achieved by making use of fast discrete sine or discrete cosine transforms.

We also showed an interpretation for the parameter γ and the order of the Sobolev space k in terms of filtering by the classical Butterworth filter. In future work we plan to exploit this interpretation by automatically selecting the order of the Sobolev space.

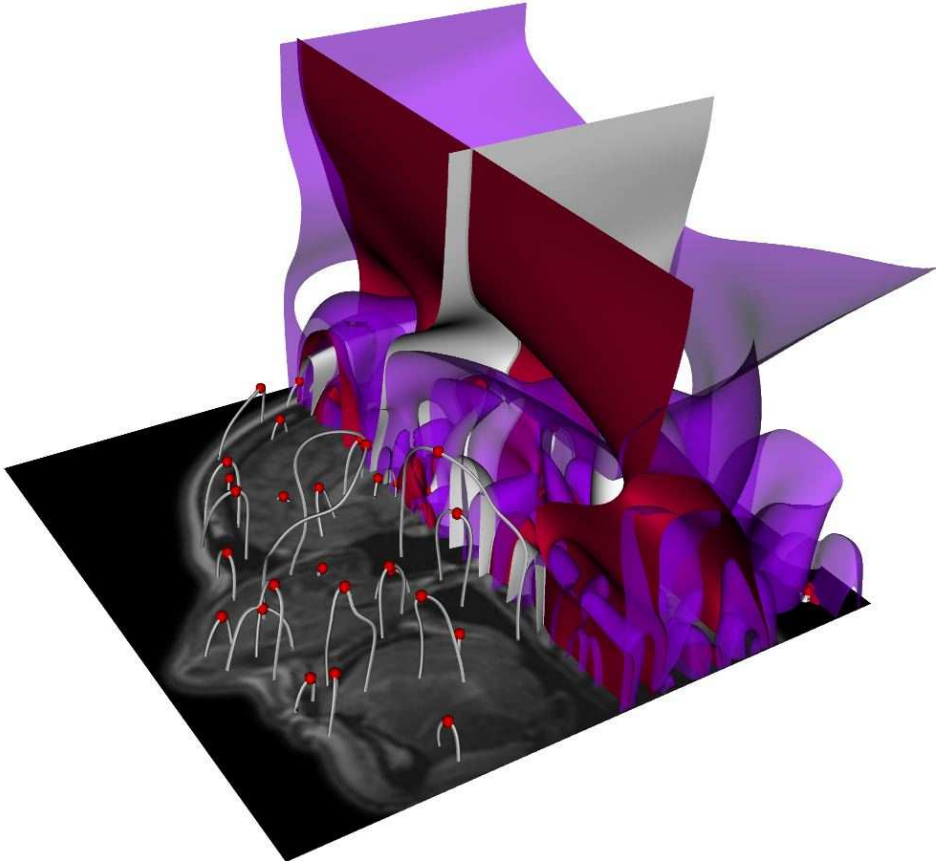


Figure 3.4: A visualization of the “deep structure” of a Gaussian scale space representation of an image. The gray paths represent critical paths (paths of vanishing gradient), a red ball shows the location of a singular point on a critical path. The surfaces show the iso-surfaces given by $\frac{\partial u_f^\Omega(x,y,s)}{\partial x} = 0$, $\frac{\partial u_f^\Omega(x,y,s)}{\partial y} = 0$ and $\det \nabla \nabla^T u_f^\Omega(x,y,s) = 0$, which are used in the calculation of the position of a singular point. Critical paths are found by intersecting the surfaces that satisfy $\frac{\partial u_f^\Omega(x,y,s)}{\partial x} = 0$ and $\frac{\partial u_f^\Omega(x,y,s)}{\partial y} = 0$. Singular points are found by intersecting the critical paths with the surface that satisfies $(\det \nabla \nabla^T u_f^\Omega)(x,y,s) = 0$. The image in this figure was provided by dr. B. Platel, Eindhoven University of Technology, department of Biomedical Engineering.

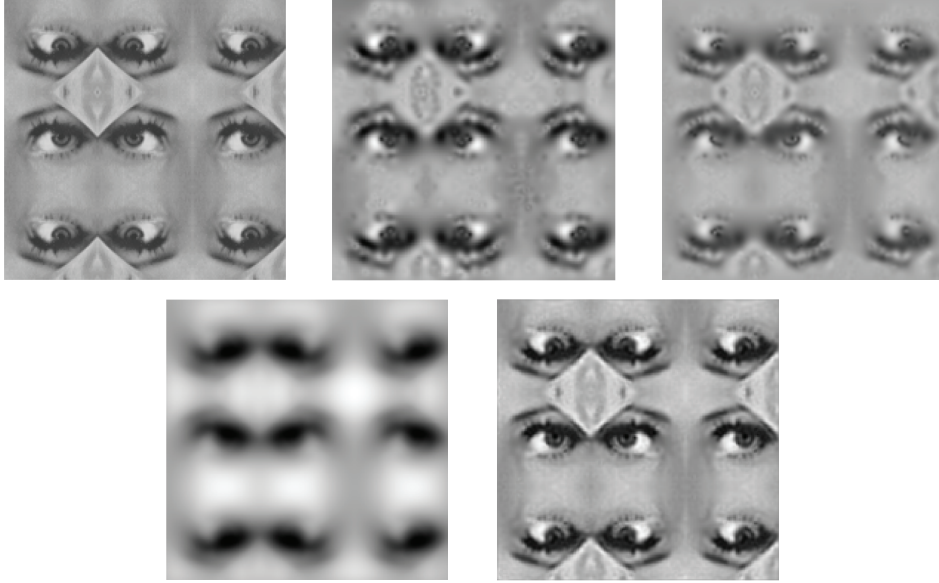


Figure 3.5: Top left: The image f from which the features were extracted. Top center and right: reconstruction from second order structure of the singular points of f using the unbounded domain method [64] (parameters: $\gamma = 50, k = 1$) and the bounded domain method (parameters: $\gamma = 50, k = 1$). Bottom row: unbounded domain (left) and bounded domain (right) reconstruction from up to second order differential structure obtained from the scale space representation of f , evaluated at the locations of the singular points of the Laplacian of f . The parameters for the reconstruction algorithm are $k = 1$ and $\gamma = 100$. The latter value of γ results in a blurred reconstruction for the unbounded domain method, whereas the bounded domain method does produce a visually appealing reconstruction (lower right) of the image that is shown in the upper left corner of this figure.



Figure 3.6: Input images that were used in the experiments. The left image shows *Lena's eye*, which is an image patch of 64×64 pixels. On the right *Barbara's face* is shown. This is an image patch of 128×128 pixels.

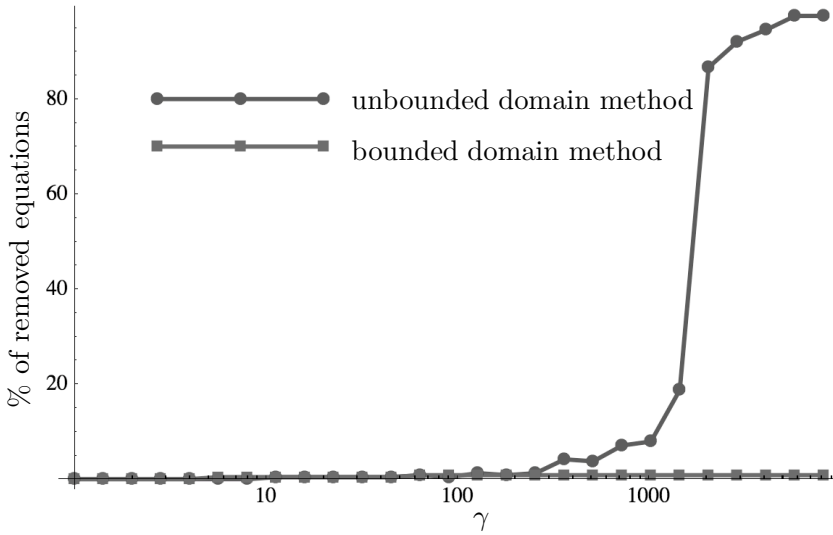


Figure 3.7: The percentage of features dropped by the *singular value decomposition* (SVD) algorithm that is used for the inversion of the Gram matrix as a function of γ . The γ axis is sampled logarithmically. Features used are up to second order derivatives measured at the singular points of the scale space representation of *Lena's eye* (see Figure 3.6). The SVD tolerance is set to 10^{-7} and $k = 1$ for both the bounded domain and the unbounded domain method.



Figure 3.8: Reconstructions from second order differential structure taken at the locations of the singular points of the scale space representation of Barbara's face using Dirichlet boundary conditions. From top to bottom $k = \{0.5 + \epsilon, 1.0, 1.5, 2.0, 2.5\}$ and from left to right $\gamma = \{1, 4, 16, 64, 256, 1024\}$. The image from which the features were obtained is shown in Figure 3.6.



Coarse-to-Fine Reconstruction

This chapter is based on:

B.J. Janssen, R. Duits, and L.M.J. Florack. Coarse-to-fine image reconstruction based on weighted differential features and background gauge fields. In *Scale Space and Variational Methods in Computer Vision: Proceedings of the Second International Conference, SSVM 2009, Voss, Norway*, Lecture Notes in Computer Science, Berlin, June 2009. Springer Verlag.

Abstract. We propose an iterative approximate reconstruction method where we minimize the difference between reconstructions from subsets of multi-scale measurements. To this end we interpret images not as scalar-valued functions but as sections through a fibred space. Information from previous reconstructions, which can be obtained at a coarser scale than the current one, is propagated by means of covariant derivatives on a vector bundle. The gauge field that is used to define the covariant derivatives is defined by the previously reconstructed image. An advantage of using covariant derivatives in the variational formulation of the reconstruction method is that with the number of iterations the accuracy of the approximation increases. The presented reconstruction method allows for a reconstruction at a resolution of choice, which can also be used to speed up the approximation at a finer level. An application of our method to reconstruction from a sparse set of differential features of a scale space representation of an image allows for a weighting of the features based on the sensitivity of those features to noise. To demonstrate the method we apply it to the reconstruction from singular points of a scale space representation of an image.

4.1 Introduction

Reconstruction from signal samples is a long standing problem in signal and image analysis [97]. We present a method for the approximation of a signal or image from its generalized samples, i.e., the samples are given on a non-equidistant grid and were obtained by means of spatially varying filters. Variational reconstruction of non-equidistant image samples has recently become of interest to the image compression community [49] where significant gains in reconstruction quality have been obtained by introducing anisotropic non-linear regularization strategies. In the scale space community a general interest in reconstruction from generalized samples has been there for quite some time [86, 79, 64, 62, 43, 63].

We propose a method that produces an image that approximately satisfies all features. Features that are more robust to perturbations of the source image are given a higher weight, which steers the reconstruction method such that those features are better approximated than those that are more sensitive to noise. This leads to a more robust reconstruction method compared to interpolating methods.

A gauge field is introduced by means of covariant derivatives on a vector bundle. This way a model of the to be reconstructed image can be incorporated in the energy functional which is minimized to find a suitable reconstruction. Using this gauge field we can construct a coarse-to-fine image reconstruction method. A coarse-to-fine approach naturally leads to a more efficient algorithm in terms of memory consumption and computational efficiency.

In Section 4.2 we will briefly introduce the image reconstruction problem. Section 4.3 describes the approximation approach and its discretization, Section 4.4 shows how to incorporate a gauge field into the reconstruction method. We conclude the paper by presenting the coarse-to-fine reconstruction algorithm and applying it to the reconstruction from singular points of a scale space representation of an image.

4.2 Image Reconstruction

In the reconstruction problem we aim for a reconstruction from a set of linear functionals on an image. These functionals represent measurements on the image and are henceforth called features. More rigorously: a feature $d_i \in \mathbb{R}$ of an image $f \in \mathbb{L}_2(\mathbb{R}^2)$ measured with a filter $\psi_i \in \mathbb{L}_2(\mathbb{R}^2)$ is given by

$$d_i = (\psi_i, f)_{\mathbb{L}_2} , \quad (4.1)$$

$i = 1, \dots, P$ in which $(\cdot, \cdot)_{\mathbb{L}_2}$ denotes the \mathbb{L}_2 inner product. In general the set of features do not describe the input image f unambiguously (they do not constitute a frame [34]), and there is need for a model to which the reconstruction should adhere. When such a model can be described by a (semi-)norm the reconstruction can be obtained directly by means of an orthogonal projection onto the features [64].

Nielsen and Lillholm [86, 79] proposed to find a reconstruction from its features using a nonlinear regularization term (model). They first search for a reconstruction that satisfies all features using a linear method and, starting from this reconstruction, subsequently apply a gradient descent that is constrained to be orthogonal to the metameric class [f] :

$$[f] = \{g \in \mathbb{L}_2(\mathbb{R}^2) \mid (\psi, f)_{\mathbb{L}_2} = (\psi, g)_{\mathbb{L}_2}\} . \quad (4.2)$$

This so called observation-constrained evolution ensures that the features are *interpolated*. When measurements are contaminated by noise *approximation* is often favored over interpolation. In the following we will not discuss the interpolation but approximation of a set of features $\{d_i\}_{i=1}^P$ that were obtained from a source image by the filters $\{\psi_i\}_{i=1}^P$.

4.3 Approximation

Instead of searching for a signal that interpolates the given features one can try to find a signal that approximates the features. In the case of noisy measurements the latter approach is often preferred. We now aim for the function $g \in \mathcal{H}^1(\mathbb{R}^2)$ that minimizes

$$E(g) = \underbrace{\sum_{i=1}^P ((g, \psi_i)_{\mathbb{L}_2} - d_i)^2}_{\text{data term}} + \frac{\lambda}{2} \underbrace{\int_{\mathbb{R}^2} \|\nabla g\|^2 dV}_{\text{regularization term}} \quad , \quad (4.3)$$

where $\lambda \in \mathbb{R}^+$ a parameter that controls the quality of the approximation. As λ tends to 0 the approximation will approach the interpolation of the features. The minimizer of this linear functional can be found by finding the unique g that solves the following Euler equation:

$$\left(\sum_{i=1}^P \psi_i ((\psi_i, g)_{\mathbb{L}_2} - d_i) \right) - \lambda \Delta g = 0 \quad . \quad (4.4)$$

The parameter λ takes into account each feature with the same weight. This is not desirable when the features are not normalized and even after normalization one can improve on the selection of the weights. We allow for these improvements by introducing P extra parameters (which we will call feature weights), $\alpha_i \in \mathbb{R}^+$, $i = 1 \dots P$, that will be set to a fixed value based on the properties of the features. In case of reconstruction from differential features of a scale space representation of an image, which is the main motivation for our method, we can select the newly introduced parameters based on the noise propagation in the scale space representation of an image. The global parameter λ can be absorbed by these parameters but will be maintained in our formulation for the sake of clarity. For fixed

α_i we now search for the g that satisfies

$$\arg \min_{g \in \mathbb{L}_2(\mathbb{R}^2)} E(g) = \arg \min_{g \in \mathbb{L}_2(\mathbb{R}^2)} \sum_{i=1}^P \alpha_i ((g, \psi_i)_{\mathbb{L}_2} - d_i)^2 + \frac{\lambda}{2} \int_{\mathbb{R}^2} \|\nabla g\|^2 dV . \quad (4.5)$$

In the next section we will discuss how the feature weights can be selected.

4.3.1 Noise Propagation

In order to be able to select sensible values for the α_i parameters that appear in eq. (4.5), we need to make some assumptions on the noise and the set of filters $\{\psi_i\}_{i=1}^P$ that are used to extract the measurements. With regard to the noise we assume additive zero-mean white Gaussian noise which has a correlation distance of τ pixels. In recent work about stability of toppoints [6] (which are singular points of a Gaussian scale space representation of an image) this was found to be a sensible assumption. In our application we will reconstruct from differential structure taken from the Gaussian scale space representation of the input image f , therefore we assume that the set of filters $\{\psi_i\}_{i=1}^P$ consists of Gaussian kernels or derivatives thereof.

The idea now is to construct the weights α_i according to the sensitivity of their associated differential features to noise. In order to estimate the sensitivity of a feature d_i of the image f that is contaminated by additive noise we can adopt work on noise propagation in scale space by Blom [11]. He proposes to compute at a certain scale $t > 0$ the momenta $M_{m_x, m_y, n_x, n_y}^2 = \langle N_{m_x, m_y}, N_{n_x, n_y} \rangle$ of derivatives of orders m_x, m_y, n_x , and n_y of the fiducial noise function N . He assumes only the covariance matrix $\langle N^2 \rangle$ of the noise to be given. In case the correlation distance τ is much smaller than the scale t ,

$$M_{m_x, m_y, n_x, n_y}^2 \simeq \langle N^2 \rangle \left(\frac{\tau}{2t} \right) \left(\frac{-1}{4t} \right)^{\frac{1}{2}(m_x + m_y + n_x + n_y)} Q_{m_x + n_x} Q_{m_y + n_y} , \quad (4.6)$$

with

$$Q_n = \begin{cases} (n+1)!! & \text{if } n \text{ even} \\ 0 & \text{if } n \text{ odd} \end{cases} . \quad (4.7)$$

Features that are sensitive to perturbations on the source image f should influence the final result less than features that are relatively insensitive to these perturbations. Therefore we compute α_i from eq. (4.6) such that

$$\alpha_i \propto M_{n_x^i, n_y^i, n_x^i, n_y^i}^{-2} \quad (4.8)$$

at scale t^i . The parameters n_x^i, n_y^i , and t^i are the derivative order in the x direction, the derivative order in the y direction and the scale of the i^{th} filter ψ_i . Here we stress that these estimations are based on the assumption that the filters are partial derivatives of a Gaussian. We furthermore ensure that $\sum_{i=1}^P \alpha_i = 1$, which essentially makes α_i independent of the value of $\langle N^2 \rangle$ and τ .

4.3.2 Discretization

We can try to solve an approximation to g by discretizing eq. (4.4) (augmented with the feature weights) or discretize the energy functional in eq. (4.5), and thereafter finding a discrete minimizer of the discretized energy. These two approaches can be equivalent for a slick choice of so called test functions that are involved in the former method. We will proceed by elaborating on directly discretizing the energy.

To solve g from eq. (4.5) we will approximate g by a β -spline of order n :

$$\beta^n(x) = \mathcal{F}^{-1} \left(\omega \mapsto \frac{(e^{i\omega/2} - e^{-i\omega/2})^{n+1}}{(i\omega)^{n+1}} \right) (x), \quad (4.9)$$

where \mathcal{F}^{-1} denotes inverse Fourier transformation. Equality (4.9) is equivalent to the $(n+1)$ -fold convolution of the β -spline of order 0

$$\beta^0(x) = \begin{cases} 1 & -\frac{1}{2} < x < \frac{1}{2} \\ \frac{1}{2} & |x| = \frac{1}{2} \\ 0 & \text{otherwise} \end{cases}; \quad (4.10)$$

a rectangle. Further details concerning β -splines can be found in, e.g., [103]. It was shown in the context of optic flow [78] and registration [101] that such an approach has computational advantages over a finite difference approach. Arigovindan et al.[2, 1] showed good results in his application

of this approach to (a multi-grid scheme for) image and vector field interpolation. Moreover it allows for a coarse-to-fine implementation in an elegant way. Key to the latter advantage is the 2-scale relation

$$\beta^n\left(\frac{x}{2^j}\right) = \sum_{k \in \mathbb{Z}} 2^{-n} \binom{n+1}{k} \beta^n\left(\frac{x}{2^{j-1}} - k\right). \quad (4.11)$$

The n -th order β -spline approximation of g in two spatial dimensions at resolution $a > 0$, is given by

$$\tilde{g}_a(x, y) = \sum_{l=0}^{M-1} \sum_{k=0}^{N-1} c_{k,l} \beta^n\left(\frac{x}{a} - k\right) \beta^n\left(\frac{y}{a} - l\right), \quad (4.12)$$

with $c_{k,l}, x, y \in \mathbb{R}$, $\beta^n(\cdot)$ the central β -spline of order $n \in \mathbb{N}$, resolution parameter a , and $N, M \in \mathbb{N}$ correspond to the width and height of the image in pixels. Notice this is a representation of the image in the continuous domain and that $\tilde{g}_a \in C^n(\mathbb{R}^2)$, i.e., n -times continuously differentiable.

The regularization term in eq. (4.5), $\int_{\mathbb{R}^2} \|\nabla g\|^2 dx dy$, can be approximated with the help of eq. (4.12) by

$$\begin{aligned} \int_{-\infty}^{\infty} \int_{-\infty}^{\infty} \|\nabla g_a(x, y)\|^2 dx dy = & \quad (4.13) \\ & \sum_{i=1}^2 \sum_{l,n=0}^{M-1} \sum_{k,m=0}^{N-1} c_{k,l} c_{m,n} \left[\int_{-\infty}^{\infty} \frac{\partial \beta^n}{\partial x_i} \left(\frac{x_i}{a} - k\right) \frac{\partial \beta^n}{\partial x_i} \left(\frac{x_i}{a} - m\right) dx_i \right] \\ & \left[\int_{-\infty}^{\infty} \beta^n \left(\frac{x_{1-i}}{a} - l\right) \beta^n \left(\frac{x_{1-i}}{a} - n\right) dx_{1-i} \right], \end{aligned}$$

where (x_1, x_2) correspond to (x, y) in eq. (4.12). When we consider the integrals in the previous equations we notice that it can be expressed by a convolution:

$$\int_{-\infty}^{\infty} \frac{\partial \beta^n}{\partial x} \left(\frac{x}{a} - k\right) \frac{\partial \beta^n}{\partial x} \left(\frac{x}{a} - m\right) dx = -a \int_{-\infty}^{\infty} \frac{\partial \beta^n}{\partial u}(u) \frac{\partial \beta^n}{\partial u}((m-k) - u) du. \quad (4.14)$$

This is easily verified by substitution of integration variable ($u = \frac{x}{a} - k$) and noting that $\beta^n(x) = \beta^n(-x)$ for all $x \in \mathbb{R}$. We furthermore note that

a derivative of a central β -spline of degree n is again a linear combination of β -splines at the expense of lowering its degree to $(n - 1)$

$$\frac{\partial}{\partial x} \beta^n(x) = \beta^{n-1}(x + 1/2) - \beta^{n-1}(x - 1/2) . \quad (4.15)$$

Notice this identity is readily obtained from eq. (4.9).

As a result we can write eq. (4.13) in matrix-vector notation as

$$\int_{-\infty}^{\infty} \int_{-\infty}^{\infty} \|\nabla g_a(x, y)\|^2 dx dy = \vec{c}^T R \vec{c} , \quad (4.16)$$

with $\vec{c} = \{c_i\}_{i=0}^{(M-1)(N-1)}$ and

$$R = \left\{ a \beta^{2n}(n-l) \right\}_{n,l=0}^{M-1} \otimes \left\{ -a \frac{\partial \beta^{2n}}{\partial x}(m-k) \right\}_{m,k=0}^{N-1} + \\ \left\{ -a \frac{\partial \beta^{2n}}{\partial y}(n-l) \right\}_{n,l=0}^{M-1} \otimes \left\{ a \beta^{2n}(m-k) \right\}_{m,k=0}^{N-1} . \quad (4.17)$$

We will express the inner product in the data term in equation (4.5) in terms of β -splines as well. This leads to an expression similar to eq. (4.14),

$$(g_a, \psi_i)_{\mathbb{L}_2(\mathbb{R}^2)} = (-1)^{n_i+m_i} \sum_{k,l=0}^{N-1, M-1} c_{k,l} (\beta^n * \psi_i)(k - x_i, l - y_i) , \quad (4.18)$$

where (x_i, y_i) and (n_i, m_i) are the location and differential order of the i^{th} filter ψ_i respectively. In contrast to the discretization of the regularization we will not derive a closed form expression for this convolution but we will approximate the β -spline in eq. (4.18) by a Gaussian. Here we use the observation in [106] that

$$\beta^n(x) \cong \sqrt{\frac{6}{\pi(n+1)}} e^{-\frac{6x^2}{(n+1)}} . \quad (4.19)$$

The data term can be expressed in matrix-vector notation by

$$E_{\text{data}}(\vec{c}) = \|\vec{S}\vec{c} - \vec{d}\|^2 , \quad (4.20)$$

where $S = \{(\beta^n * \psi_i)(k - x_i, l - y_i)\}_{k,l=0,i=1}^{(N-1)(M-1),P}$ and $\vec{d} = \{d_i\}_{i=1}^P$.

Now we can write the minimizer of equation (4.5) in matrix-vector notation as

$$(S^T S + \lambda R) \mathbf{c} = S^T \mathbf{d}. \quad (4.21)$$

This linear system of equations can be solved using a conjugate gradient (CG) method [7]. In case the matrix S is sparse it is beneficial to apply a multi-grid method [15]. Mainly due to the non-sparseness of S , the conjugate gradient method is preferred. Notice that, in this specific case, R can be expressed as a convolution. For large images it is not feasible to explicitly compute $S^T S$, therefore we compute the matrix vector product $\hat{\mathbf{c}} = S^T S \mathbf{c}$ that appears in a conjugate gradient iteration by first evaluating $\tilde{\mathbf{c}} = S \mathbf{c}$ and thereafter evaluating $\hat{\mathbf{c}} = S^T \tilde{\mathbf{c}}$.

4.4 Adaptation to a Gauge Field

In the previous sections we used a very simple model as a regularization term. For several applications it would be beneficial if we were able to introduce a more sophisticated model of the image we want to reconstruct. Feature based image editing [68] and optic flow estimation [43, 63] are applications that potentially have great benefit of such a refinement. Recently an image in-painting method was introduced that achieves a model refinement by means of covariant derivatives on a vector bundle that are guided by a user selectable gauge field [50]. We will adapt a similar approach.

The basic idea is to replace the gradient that appears in the regularization term of eq. (4.5) by a covariant derivative D^{A_h} that is biased by a gauge field $h \in \mathbb{H}^2(\mathbb{R}^2)$. To this covariant derivative the gauge field h should be “invisible”, i.e $D^{A_h} h = 0$. If we were able to put h to be the original image f the approximation would exactly produce f again.

To this end we interpret f not as a scalar function but as a section through a fibred space $E = \mathbb{R}^2 \times \mathbb{R}^+$. Heuristically this means that we rescale intensity by a spatially varying factor, the unit section σ . Thus we consider $f\sigma$ instead of f to model intensity values in the image (the latter is a special case in which $\sigma(\vec{x}) = (\vec{x}, 1) \forall \vec{x} \in \mathbb{R}^2$). This implies that when we consider

derivatives, we need to account for the spatial variability of σ . In the next subsection we will introduce to this end a connection on a vector bundle. There, we will also make the heuristic description of our approach presented in the beginning of this section a bit more rigorous.

For the reader who is not familiar with the concept of vector bundles it could be useful to take notice of Fig. 4.1 before reading the next subsection, since it aids in developing the right geometrical interpretation of the presented material.

4.4.1 Connections on Vector Bundles

Consider a vector bundle (E, π, M) , with total space $E = \mathbb{R}^2 \times \mathbb{R}^+$, base space $M = \mathbb{R}^2$, and projection $\pi : E \rightarrow M$. π projects a point in E (a point in M augmented with an intensity $L \in \mathbb{R}^+$) to M in the following manner

$$\pi(x, y, L) = (x, y) . \quad (4.22)$$

L amounts to a certain physical quantity such as luminous intensity, which is expressed in candela (cd). Next we define a section $s : M \rightarrow E$ such that $\pi \circ s = \text{id}_M$, where id_M denotes the identity map on M . We define the association of a section σ_f with unique image $f \in \mathbb{L}_2(\mathbb{R}^2)$ as

$$f \leftrightarrow \sigma_f \Leftrightarrow \forall_{(x,y) \in \mathbb{R}^2} \sigma_f(x, y) = (x, y, f(x, y)) . \quad (4.23)$$

The multiplication of such a section σ_f by an image g is given by

$$g\sigma_f = \sigma_{fg} . \quad (4.24)$$

Let $\tilde{\sigma}$ denote the unit section $\tilde{\sigma}(x, y) = (x, y, L_0)$, with L_0 a fixed luminous intensity unit (e.g. 1cd).

We want to define a connection D over the space of sections $\Gamma(E)$ on E . Let $\mathcal{L}(\Gamma(TM), \Gamma(E))$ denote the space of linear operators that map a section of a tangent bundle on M to a section of a vector bundle. Here we stress that a section of a tangent bundle, $V \in \Gamma(TM)$, is just a vector field on M . A map

$$D : \Gamma(E) \rightarrow \mathcal{L}(\Gamma(TM), \Gamma(E)) \quad (4.25)$$

is a connection on a vector bundle iff it possesses the following properties, cf. [67], pp.106. In the following we will use standard notation $D_V\sigma = (D\sigma)(V)$.

1. D is tensorial in V :

$$D_{V+W}\sigma = D_V\sigma + D_W\sigma \text{ for } V, W \in \Gamma(TM), \sigma \in \Gamma(E) \quad (4.26)$$

$$D_{fV}\sigma = fD_V\sigma \text{ for } f \in C^\infty(M, \mathbb{R}), V \in \Gamma(TM) . \quad (4.27)$$

2. D is \mathbb{R} -linear in σ :

$$D_V(\sigma + \tau) = D_V\sigma + D_V\tau \text{ for } V \in \Gamma(TM), \sigma, \tau \in \Gamma(E) \quad (4.28)$$

and it satisfies the Leibniz product rule:

$$D_V(f\sigma) = V(f)\sigma + fD_V\sigma \text{ for } f \in C^\infty(M, \mathbb{R}) . \quad (4.29)$$

Suppose we have a section D on a vector bundle. Then it must satisfy the four properties (eqs. (4.26) to (4.29)) mentioned above. Therefore we must have the following identity

$$\begin{aligned} D\sigma(X)(c(t)) &= D(z\tilde{\sigma})(X)(c(t)) \\ &= X|_{c(t)}(z)\tilde{\sigma} + \sum_{i=1}^2 z(c(t))\dot{c}^i(t)D_{\partial_{x_i}}\tilde{\sigma} \end{aligned} \quad (4.30)$$

for all sections $\sigma = z\tilde{\sigma}$, and vector fields $X = \sum_{i=1}^2 \dot{c}^i \partial_{x_i}$. Here $c : (0, 1) \rightarrow M$ is a smooth curve on M , $\dot{c}^i(t) = \langle dx^i, \dot{c}(t) \rangle$ $i = 1, 2$, with $\dot{c}(t) = \frac{d}{dt}c(t)$, and $z \in C^\infty(M, \mathbb{R})$ an arbitrary image. By $\{dx^i\}_{i=1}^2 = \{dx, dy\}$ we denote the dual frame in the cotangent bundle T^*M .

For each $i = 1, 2$ $D_{\partial_{x_i}}\tilde{\sigma}$ should be a section on the vector bundle. Such a section can be identified with a function

$$A_i : M \rightarrow \mathbb{R} \quad (4.31)$$

by eq. (4.23) , i.e.,

$$D_{\partial_{x_i}}\sigma = \sigma_{A_i} = A_i\tilde{\sigma} . \quad (4.32)$$

Substituting eq. (4.32) into eq. (4.30) yields

$$D\sigma(X)(c(t)) = \sum_{i=1}^2 \left(\dot{c}^i(t) \partial_{x_i}(z)(c(t)) + z(c(t)) \dot{c}^i(t) A_i(c(t)) \right) \tilde{\sigma} . \quad (4.33)$$

So each connection is parameterized by the co-vector field $A = \sum_{i=1}^2 A_i dx^i$.

At this point we still have a degree of freedom, namely we still can select a specific co-vector field. In our application we want a certain image h to be “invisible” so for a fixed h we select $A = A_h$ such that

$$\left(D^{A_h}(\sigma_h) \right) = 0 , \quad (4.34)$$

i.e., $D_{\dot{c}}^{A_h}(\sigma_h) = 0$ for all curves c , holds for a specific image h . Here we made the dependence of D on A_h explicit in the superscript notation (in the previous equations we left it out in order to facilitate readability). Given the requirement of eq. (4.34) we explicitly calculate

$$\left(\dot{c}^i(t) (\partial_{x_i} h)(c(t)) + h(c(t)) \dot{c}^i(t) A_i(c(t)) \right) \tilde{\sigma} = 0 \tilde{\sigma} \quad (4.35)$$

for all curves $c : (0, 1) \rightarrow M$

$$\Leftrightarrow (\nabla h)(c(t)) + h(c(t)) A(c(t)) = 0 \quad (4.36)$$

$$\Leftrightarrow A_h(c(t)) = - \sum_{i=1}^2 \partial_{x_i} \log h(c(t)) dx^i \quad \forall h > 0 . \quad (4.37)$$

Which gives us an expression for A_h (eq. (4.37)) provided h is strictly positive. This is a limitation of our method. However, for a system that observes physical quantities this is a realistic assumption.

From the previous derivations we conclude that applying a covariant derivative that is gauged by an image h to an image f amounts to

$$\begin{aligned} \left(D^{A_h}(\sigma_f) \right) (\dot{c}) &= \left(\dot{c}(f) + \sum_{i=1}^2 A_i \dot{c}^i f \right) \tilde{\sigma} = \left(\dot{c}(f) - \sum_{i=1}^2 ((\partial_{x_i} \log h) \dot{c}^i f) \right) \tilde{\sigma} \\ &= \left(\dot{c}(f) - \frac{f}{h} \dot{c}(h) \right) \tilde{\sigma} . \end{aligned} \quad (4.38)$$

Here we used the following short notation:

$$\dot{c}(f) = \sum_{i=1}^2 \dot{c}^i \partial_{x_i}(f) = (\dot{c}(t) \cdot \nabla f)(c(t)) = \frac{d}{dt} f(c(t)) . \quad (4.39)$$

Note that eq. (4.38) can be rewritten as

$$\forall_{c:(0,1) \rightarrow M} : \left(D^{A_h} \sigma_f(\dot{c}(t)) \right) (c(t)) = \tilde{\sigma} (df + f A_h) (\dot{c}(t)) , \quad (4.40)$$

i.e., $D^{A_h} (f \tilde{\sigma}) = \tilde{\sigma} (df + f A_h)$. When we identify $\sigma_f = f \tilde{\sigma} \leftrightarrow f$ this simplifies to

$$D^{A_h} f = (d + A_h) f , \quad (4.41)$$

in which $A_h f$ is a multiplication.

The calculation of a covariant derivative as described in eq. (4.38) allows for a geometrical interpretation. A visualization thereof, which is depicted in Fig. 4.1, will be described next. We stipulate this is a specially crafted example since there is only structure present in one single direction. Therefore we only have to construct a visualization for the calculation of a covariant derivative in the direction that is labelled by x in the figure. The derivative in the direction that is labelled by y simply vanishes.

On the base space M a curve $c : (0, 1) \rightarrow M$ is drawn. We want to calculate the covariant derivative of the section σ_f at the point that corresponds to $c(t)$ on the base space. The covariant derivative is gauged by the gauge field h . Therefore another section, σ_h , is depicted in the figure. The gradient of σ_h at the point $\sigma_h(c(t))$ in total space E is depicted by a line, labelled A , through $\sigma_h(c(t))$ and $\sigma_h(c(t+\epsilon))$. The line labelled D visualizes in a similar manner the gradient of σ_f at $\sigma_h(c(t))$. On the left side it is shown how the gradient of A is attenuated by the fraction of the values of $\sigma_f(c(t))$ and $\sigma_h(c(t))$. The value of this attenuated directional derivative is added to the directional derivative of σ_f at $\sigma_f(c(t))$ in the upper left of the figure to finally produce the result of eq. (4.38). To clarify the attenuation process we added Fig. 4.2 where the relevant lines are labeled the same as their corresponding lines in Fig. 4.1.

In essence the energy functional for which we search a minimizer stays the same as the one for which a minimizer is sought in eq. (4.5). We merely change the notion of a gradient, which is adapted to a gauge field h , the resulting energy functional now reads

$$E(g) = \sum_{i=1}^P \alpha_i ((g, \psi_i)_{\mathbb{L}_2} - d_i)^2 + \frac{\lambda}{2} \int_{\mathbb{R}^2} \|D^{A_h} g\|^2 dV , \quad (4.42)$$

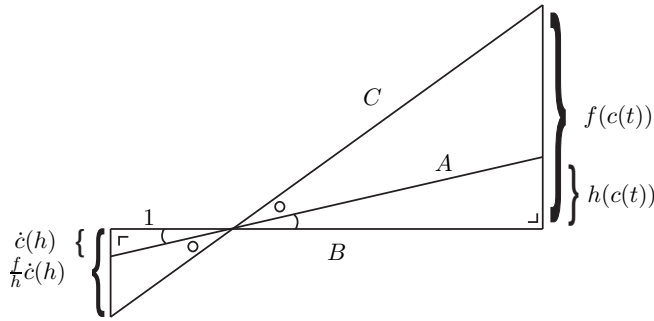


Figure 4.2: Visualization of the amplification of $\dot{c}(h)$ by $\frac{f(c(t))}{h(c(t))}$. This image clarifies the congruence relations that are used in Fig. 4.1.

For more information about catastrophe theory in general, its application in scale space theory and the calculation of the locations of singular points we refer to [51, 26, 44, 69]. A filter ψ_i corresponding to a derivative at a certain position in the scale space of an image is given by

$$\psi_i(x, y) = (2s_i)^{\frac{n_i+m_i}{2}} \frac{\partial^{n_i+m_i}}{\partial(x^{n_i}y^{m_i})} \frac{1}{4\pi s_i} e^{-\frac{((x-x_i)^2+(y-y_i)^2)}{4s_i}}, \quad (4.46)$$

where we used natural derivatives¹ [80] as proposed by Lindeberg. Here we used multi-index notation $i = (x_i, y_i, m_i, n_i, s_i)$. A singular point is encoded by storing the second order derivative jet for each singular point location.

The discretization proposed in section 4.3.2 allows for a reconstruction at a certain resolution $a > 0$. We will select scales $\{2^j\}_{j=0}^J$. First we find all features which can be approximated well at the coarsest resolution J , i.e., those features for which

$$\|\psi_i - P_{V_a}\psi_i\| < \epsilon, \quad (4.47)$$

where P_{V_a} denotes the \mathbb{L}_2 -projection onto the set $V_a = \{\beta^n(\frac{x}{a} - k)\beta^n(\frac{x}{a} - l) | k, l \in \mathbb{Z}\}$ and $\epsilon > 0$ a small constant. For an efficient method to obtain an approximation of this error we refer to [12]. Next we compute a reconstruction at resolution J using a constant gauge field h . Then, for each scale $j = J - 1 \dots 0$ we find the gauge field by application of the two scale relation (see eq. (4.11)) to the reconstructed image at scale $j + 1$. In order

¹In image processing the term natural derivative is used to denote this particular scaling of a Gaussian derivative.



Figure 4.3: From left to right, (1) the source image “trui”, (2) reconstruction at resolution 65×65 pixels from 84 feature points, (3) reconstruction from 226 feature points at 129×129 pixels and gauged by the image on its left, (4) reconstruction from 727 feature points at 257×257 pixels and gauged by the image on its left, (5) same reconstruction as the image on the left but not gauged, and (6) reconstruction from all 1070 feature points, no gauge field. The features are up to second order differential structure obtained from the scale space representation of the source image at its singular point positions.

to reduce memory consumption and gain computational efficiency we leave out all features that were used in a coarser scale reconstruction than the current one such that those features are only implicitly encoded (via the gauge field) in the reconstruction algorithm.

See the caption of Figure 4.3 for a description of the experiments we conducted. Comparing the fourth and fifth image shows that features which are not directly encoded are passed by the gauge field (lower resolution images). In fact the difference between the two reconstructions is quite striking. We furthermore note that memory requirements and the computational complexity for the algorithms to produce these two images are equivalent. When the features of all 1070 singular points are directly used (right most image in Figure 4.3) the visual quality is more appealing. The memory requirements are however much larger. We also mention the method of feature selection for the next level is quite crude and can be improved by incorporating, e.g., a feedback loop. These are possibilities for future exploration which are allowed by the presented framework.

4.6 Conclusions

We introduced a coarse-to-fine image reconstruction method that approximates a set of generalized samples that are weighted according to their noise robustness. Information from a coarse resolution reconstruction is

passed to a finer resolution level by means of a gauge field. To this end we considered the image not as a scalar function but as a section through a fibred space. Application of the newly proposed method to the reconstruction from singular points of a scale space representation of an image shows the feasibility of the method.



Left-Invariant Reassignment on the Heisenberg Group

5.1 Introduction

The Gabor transform was first proposed in 1964 in a discrete setting [48, 100]. Later it was formulated in a continuous setting [56] showing its close resemblance to the short-time Fourier transform. In the mid 1970's Koderá et al. [73] noticed the need for a further enhancement of the spectrogram that is obtained from the short-time Fourier transform of a signal by taking its squared modulus. They noticed that, due to the uncertainty principle, there is always a tradeoff between time and frequency resolution in the short-time Fourier transform (or as they call it: moving-window method). As a result the spectrogram shows a “blurred” version of the true spectral density. The modified moving-window method they propose as a solution to this problem indeed sharpens the spectrogram and thereby increases its readability. However, their modification only handles the square modulus of the short-time Fourier transform of a signal and loses the phase information. Therefore it is not possible to reconstruct the signal from its modified moving-window method representation; it is not invertible. The improvements of the method by Auger and Flandrin [3] yielded computational advantages but still lacked the property of invertibility.

The first method that does have the invertibility property is an application of reassignment to the continuous wavelet transform [28]. A method called differential reassignment was later developed by Chassande-Mottin et al. [23, 22]. This method produces a vector field along which the spectrogram is continuously deformed, whence the term differential reassignment. A group-theoretical interpretation of the latter method can be found in [29].

We show how reassignment can be interpreted on the full Weyl-Heisenberg group. To this end we add an extra dimension to the conventional Gabor transform and analyze what operators can be applied to our Gabor transform of a signal. The operators that are shown to be suitable for the construction of partial differential equation (PDE) based methods are then mapped back to the conventional Gabor transform. These operators are subsequently used to implement a convection process on the transform domain. Discretization of the reassignment method is done by identifying a discrete group for which the corresponding operators are derived and which allows for an exact implementation on a discrete grid. Based on these discrete operators we identify a discrete window which allows an ac-

curate implementation of the reassignment method. We furthermore show that a reassigned version of a Gabor transform can be obtained by means of a morphological erosion operation.

5.2 Gabor Transforms

In order to obtain local frequency information of a signal $f : \mathbb{R}^d \rightarrow \mathbb{C}$, $d \in \mathbb{N}$ one usually employs a continuous Gabor transform $\mathcal{G}_\psi f : \mathbb{R}^d \times \mathbb{R}^d \rightarrow \mathbb{C}$ defined by

$$(\mathcal{G}_\psi f)(x, \omega) = \int_{\mathbb{R}^d} f(\xi) \overline{\psi(\xi - x)} e^{-2\pi i(\xi - x) \cdot \omega} d\xi . \quad (5.1)$$

Here $\psi : \mathbb{R}^d \rightarrow \mathbb{C}$ is the analysis window. Another convention for the continuous Gabor transform one often encounters is the following one:

$$(\mathbb{G}_\psi f)(x, \omega) = \int_{\mathbb{R}^d} f(\xi) \overline{\psi(\xi - x)} e^{-2\pi i \xi \cdot \omega} d\xi . \quad (5.2)$$

The definition in eq. (5.1) amounts to a shifted modulation factor and the one in eq. (5.2) amounts to a modulation factor that is fixed. If one is only interested in the modulus of the transformed signal, such as the spectrogram, the choice of convention is of no importance.

If $\|\psi\|^2 = 1$, then for all $f \in \mathbb{L}_2(\mathbb{R}^d)$, by the results in [54], it follows that

$$\|\mathcal{G}_\psi f\|^2 = \|f\|^2 . \quad (5.3)$$

As a result we find for all $f, g \in \mathbb{L}_2(\mathbb{R}^d)$

$$(\mathcal{G}_\psi f, \mathcal{G}_\psi g)_{\mathbb{L}_2(\mathbb{R}^d)} = (f, g)_{\mathbb{L}_2(\mathbb{R}^d)} . \quad (5.4)$$

So the inverse transform can be obtained by noting that

$$(f, \mathcal{G}_\psi^* \mathcal{G}_\psi g)_{\mathbb{L}_2(\mathbb{R}^d)} = (f, g)_{\mathbb{L}_2(\mathbb{R}^d)} , \quad (5.5)$$

for all f, g . So $\mathcal{G}_\psi^{-1} = \mathcal{G}_\psi^*$.

We will use yet another definition of the continuous Gabor transform for reasons that will become apparent later on. In our definition of the continuous Gabor transform of a signal $\mathcal{W}_\psi f : \mathbb{R}^d \times \mathbb{R}^d \times (\mathbb{R}/\mathbb{N}) \rightarrow \mathbb{C}$, we introduce one extra variable compared to the more conventional definitions in eqs. (5.1) and (5.2):

$$(\mathcal{W}_\psi f)(x, \omega, s) = e^{-2\pi i(s + \frac{x \cdot \omega}{2})} \int_{\mathbb{R}^d} f(\xi) \overline{\psi(\xi - x)} e^{-2\pi i(\xi - x) \cdot \omega} d\xi, \quad (5.6)$$

where $x, \omega \in \mathbb{R}^d$, and $s \in \mathbb{R}/\mathbb{N}$. We note that

$$(\mathcal{G}_\psi f)(x, \omega) = (\mathcal{W}_\psi f)(x, \omega, s = -\frac{x \cdot \omega}{2}) \quad (5.7)$$

and

$$(\mathbb{G}_\psi f)(x, \omega) = (\mathcal{W}_\psi f)(x, \omega, s = \frac{x \cdot \omega}{2}). \quad (5.8)$$

Since \mathcal{W}_ψ only adds a modulation component, i.e., $e^{-2\pi i(s + \frac{x \cdot \omega}{2})}$, in front of \mathcal{G}_ψ , we can reconstruct in the following manner

$$f(\xi) = (\mathcal{W}_\psi^* \circ \mathcal{W}_\psi f)(\xi) \quad (5.9)$$

$$= \int_0^1 \int_{\mathbb{R}^d} (\mathcal{W}_\psi f)(x, \omega, s) \psi(\xi - x) e^{2\pi i(s - \frac{x \cdot \omega}{2} + \xi \cdot \omega)} dx d\omega ds. \quad (5.10)$$

Notice that we chose to integrate over s even though the integrand does not depend on it. However, as soon as an operator Ψ is applied in the Gabor domain the effective operator $\mathcal{W}_\psi^* \circ \Psi \circ \mathcal{W}_\psi$ reasonably requires integration over s .

To get more insight into these transforms consider a translation operator associated to the time variable $x \in \mathbb{R}^d$ acting on a signal,

$$(\mathcal{T}_{x'} f)(x) = f(x - x'), \quad (5.11)$$

and a translation operator associated to the frequency variable $\omega \in \mathbb{R}^d$,

$$(\mathcal{M}_\omega f)(x) = e^{2\pi i \omega \cdot x} f(x), \quad (5.12)$$

which is a modulation. It is easy to verify that these operators do not commute, i.e.,

$$\mathcal{T}_x \mathcal{M}_\omega = e^{2\pi i x \cdot \omega} \mathcal{M}_\omega \mathcal{T}_x, \quad (5.13)$$

and, as a result,

$$(\mathcal{M}_\omega \mathcal{T}_x)(\mathcal{M}_{\omega'} \mathcal{T}_{x'}) = e^{2\pi i x \cdot \omega'} \mathcal{M}_{\omega+\omega'} \mathcal{T}_{x+x'} . \quad (5.14)$$

The continuous Gabor transform in eq. (5.1) can be expressed in terms of these time and frequency-shift operators,

$$\mathcal{G}_\psi(f)(x, \omega) = \int_{\mathbb{R}^d} f(\xi) \overline{\mathcal{M}_\omega \mathcal{T}_x \psi(\xi)} d\xi . \quad (5.15)$$

We must however conclude from eq. (5.14) that this transform is not fully covariant with respect to these time and frequency shifts of the input signal. Notice the absolute value of this transform *is* covariant with respect to translations and modulations. Apparently time and frequency translations, that form the domain of the continuous Gabor transform parameterized by \mathbb{R}^{2d} , do not form a group. They however do, as noted in the context of reassignment by Daudet et al. [29], form a $2d + 1$ -dimensional group: the Weyl-Heisenberg group. Hence the occurrence of $s \in \mathbb{R}$ in eq. (5.6). We elaborate on this in the next section.

5.3 The Weyl-Heisenberg Group

For simplicity we consider $d = 1$, and consider the Heisenberg group H_3 that is parameterized by the group elements $g = (x, \omega, s) \in \mathbb{R}^3$ with group product

$$gg' = (x, \omega, s)(x', \omega', s') = (x + x', \omega + \omega', s + s' + \frac{1}{2}(\omega x' - x \omega')) , \quad (5.16)$$

group inverse $g^{-1} = (-x, -\omega, -s)$, and unit element $e = (0, 0, 0)$. The Haar measure $d\mu_{H_3}(g)$ that is associated to the group, i.e., the measure that is invariant under group translations, is the conventional Lebesgue measure: $d\mu_{H_3} = dx d\omega ds$.

The Schrödinger representation $\mathcal{U} : H^3 \rightarrow \mathcal{B}(\mathbb{L}_2(\mathbb{R}^2))$, which is a mapping from Heisenberg group elements to bounded linear operators on $\mathbb{L}_2(\mathbb{R}^2)$, is given by

$$\mathcal{U}_{g=(x, \omega, s)} \psi(\xi) = e^{2\pi i(s + \omega \cdot \xi - \frac{x \cdot \omega}{2})} \psi(\xi - x) = e^{2\pi i s} \mathcal{M}_{\frac{\omega}{2}} \mathcal{T}_x \mathcal{M}_{\frac{\omega}{2}} \psi(\xi) \quad (5.17)$$

with $\psi \in \mathbb{L}_2(\mathbb{R})$. One can verify this is a unitary irreducible representation of H_3 [53, Chapter 9]. This means that using this representation the group product, cf. eq (5.16), the identity element and group inverse of the Heisenberg group are preserved.

Using eq. (5.17) the continuous Gabor transform, recall eq. (5.6), can be expressed as follows

$$(\mathcal{W}_\psi f)(g) = (\mathcal{U}_g \psi, f)_{\mathbb{L}_2(\mathbb{R})} = e^{-2\pi i(s + \frac{x \cdot \omega}{2})} \int_{\mathbb{R}^d} f(\xi) \overline{\psi(\xi - x)} e^{-2\pi i(\xi - x) \cdot \omega} d\xi \quad (5.18)$$

for all $f \in \mathbb{L}_2(\mathbb{R})$ and $g = (x, \omega, s) \in H_3$. The group structure that is thus put on the domain of the continuous Gabor transform will show to be crucial for the reassignment method, and in fact for many other signal processing methods.

To get a periodic phase we now consider the *reduced* Heisenberg group $H_r = H_3 / \{0\} \times \{0\} \times \mathbb{Z}$, where we have divided out the kernel of \mathcal{H}_r , $\{(0, 0, t) \mid t \in \mathbb{Z}\}$. We now identify H_r with $\mathbb{R}^2 \times \mathbb{T}$ and denote group elements by $g = (x, \omega, z)$ with $z = e^{2\pi i s}$. As a consequence we have

$$(\mathcal{W}_\psi f)(x, \omega, z) = z^{-1} (\mathcal{W}_\psi f)(x, \omega, 1) \quad (5.19)$$

for all $f, \psi \in \mathbb{L}_2(\mathbb{R})$. The closure of all continuous Gabor transforms in $\mathbb{L}_2(H_r)$ is defined by the function space

$$\mathcal{H} = \{F : H_r \rightarrow \mathbb{C} \mid F(p, q, z) = z^{-1} F(p, q, 1), \\ F(\cdot, \cdot, z) \in \mathbb{L}_2(\mathbb{R}^2) \text{ for all } z \in \mathbb{T}\} . \quad (5.20)$$

Clearly $\mathcal{W}_\psi f \in \mathcal{H}$ for all $f, \psi \in \mathbb{L}_2(\mathbb{R})$.

5.3.1 Differential Operators on the Weyl-Heisenberg Group

The reassignment procedure should be covariant with respect to translations and modulations of the signal. This constraint was also suggested in the context of reassignment in [29]. In order to ensure covariance it is natural to study how operators on the continuous Gabor transform of a signal relate to operators on the signal itself. To this end we first introduce

the left-regular and right-regular representations of functions $\phi \in \mathbb{L}_2(H_r)$, which are given by

$$(\mathcal{L}_g\phi)(h) = \phi(g^{-1}h) , \quad g, h \in H_r \quad (5.21)$$

$$(\mathcal{R}_g\phi)(h) = \phi(hg) , \quad g, h \in H_r \quad (5.22)$$

respectively. A vector field X on H_r is called left-invariant when

$$(X\mathcal{L}_g\phi) = \mathcal{L}_g(X\phi) \Leftrightarrow \forall_{h \in H_r} : X_h\mathcal{L}_g\phi = X_{g^{-1}h}\phi \quad (5.23)$$

for all smooth functions $\phi : H_r \rightarrow \mathbb{C}$, and $g, h \in H_r$. We consider these vector fields to construct operators $\Phi : \mathcal{H} \rightarrow \mathcal{H}$ on Gabor transforms since their left-invariance ensures that the corresponding operator Υ_ψ on the signal $f \in \mathbb{L}_2(\mathbb{R})$ is covariant with respect to group translations, i.e., translations and modulations of the signal (recall eq. (5.17))

$$\forall_{g \in H_r} \quad \Phi \circ \mathcal{L}_g = \mathcal{L}_g \circ \Phi \Leftrightarrow \forall_{g \in H_r} \quad \Upsilon_\psi \circ \mathcal{U}_g = \mathcal{U}_g \circ \Upsilon_\psi , \quad (5.24)$$

with

$$\Upsilon_\psi = (\mathcal{W}_\psi)^* \circ \Phi \circ \mathcal{W}_\psi : \mathbb{L}_2(\mathbb{R}) \rightarrow \mathbb{L}_2(\mathbb{R}) , \quad (5.25)$$

and $\psi \in \mathbb{L}_2(\mathbb{R})$. This can be easily verified by noticing that

$$\mathcal{W}_\psi \circ \mathcal{U}_g = \mathcal{L}_g \circ \mathcal{W}_\psi \quad \forall_{g \in H_r} \quad \text{and} \quad \mathcal{W}_\psi^* \circ \mathcal{L}_g = \mathcal{U}_g \circ \mathcal{W}_\psi^* \quad \forall_{g \in H_r} . \quad (5.26)$$

This allows us to consider left-invariant operators on the Gabor domain of which the equivalent covariant counterparts would be highly non-trivial on the signal domain. Therefore we proceed to construct the left-invariant vector fields for the specific case of H_r .

Let us take a basis $\{A_1, A_2, A_3\} = \{\partial_x, \partial_\omega, \partial_z\}$ attached to the unit element $e = (0, 0, 0)$ of H_r for the Lie-algebra $T_e(H_r)$ equipped with the Lie product

$$[A, B] = \lim_{t \rightarrow 0} \left(\frac{a(t)b(t)a^{-1}(t)b^{-1}(t) - e}{t^2} \right) , \quad (5.27)$$

with a and b smooth curves in H_r through the unit element such that their tangent vector at the unit element equals A and B respectively. Here we used shorthand notation for partial derivatives, e.g., ∂_x is shorthand notation for $\frac{\partial}{\partial x}$. One can verify that the only non-vanishing product of elements of this basis is $[A_1, A_2] = -A_3$.

Any tangent vector τ at the origin can be written as

$$\tau = \sum_{i=1}^3 a_i A_i , \quad (5.28)$$

where $a_i \in \mathbb{R}$, ($i = 1, 2, 3$) represent the coordinates of the tangent vector. Now we can identify a left-invariant vector field $X^{(\tau)}$ that is associated to such a tangent vector τ at the origin. Let $t \mapsto \gamma(t)$ be a smooth curve in H_r such that $\gamma(0) = 0$ and $\dot{\gamma}(0) = \tau$ (here we used $\dot{\gamma}(t)$ to denote $\frac{d}{dt}\gamma(t)$). Now we define, following [98, Chapter XII],

$$\left(X^{(\tau)}\phi\right)(h) = d\mathcal{R}(\tau)\phi(h) = \frac{d}{dt}\phi(h \cdot \gamma(t))|_{t=0} , \quad (5.29)$$

with $h \in H_r$ and ϕ a sufficiently smooth function on H_r . One can verify that

$$\left(X^{(\tau)}\mathcal{L}_g\phi\right)(h) = \frac{d}{dt}\mathcal{L}_g\phi(h \cdot \gamma(t))|_{t=0} \quad (5.30)$$

$$= \frac{d}{dt}\phi(g^{-1}h \cdot \gamma(t))|_{t=0} = \left(X^{(\tau)}\phi\right)(g^{-1}h) , \quad (5.31)$$

which shows $X^{(\tau)}$ is indeed left-invariant. This construction follows directly from the fact that $\mathcal{R}_g \circ \mathcal{L}_h = \mathcal{L}_h \circ \mathcal{R}_g$ for all $g, h \in H_r$. We furthermore note that

$$\left(X^{(\tau)}\phi\right)(h) = \left(X^{(\tau)}\mathcal{L}_h\phi\right)(0) , \quad (5.32)$$

for all h so $X_h^{(\tau)}$ can always be identified with $X_e^{(\tau)}$ by means of \mathcal{L}_h .

After application of eq. (5.29) to $\gamma(t) = \tau t$ for (recall eq. (5.28)) $a_i = 1$, $a_j = 0$ $i \neq j$ with respectively $i = 1, 2, 3$ we obtain the following left-invariant vector fields:

$$\begin{aligned} \mathcal{A}_1|_g\phi &= \left((\partial_x + \frac{\omega}{2}\partial_s)\phi\right)(g) \\ \mathcal{A}_2|_g\phi &= \left((\partial_\omega - \frac{x}{2}\partial_s)\phi\right)(g) \\ \mathcal{A}_3|_g\phi &= (\partial_s\phi)(g) \end{aligned} \quad (5.33)$$

for all $g = (x, \omega, e^{2\pi i s}) \in H_r$ and $\phi \in \mathbb{L}_2(H_r)$. It is easy to verify that all their commutators $[\mathcal{A}_i, \mathcal{A}_j] = \mathcal{A}_i\mathcal{A}_j - \mathcal{A}_j\mathcal{A}_i$ vanish except for

$$[\mathcal{A}_1, \mathcal{A}_2] = -\mathcal{A}_3 = -[\mathcal{A}_2, \mathcal{A}_1] . \quad (5.34)$$

In principle we are now set to construct left-invariant operators by means of linear combinations of the left-invariant vector fields that were obtained in eq. (5.33). However, we will postpone this until after the introduction of phase-space.

5.3.2 Phase-Space

The previous section outlined how to perform operations on \mathcal{H} such that their net effect on the signal is covariant with respect to translations and modulations. It would however be very practical if we were able to link the previous construction to the range of \mathcal{G}_ψ , $R(\mathcal{G}_\psi) = \{\mathcal{G}_\psi f \mid f \in \mathbb{L}_2(\mathbb{R})\}$ since this would both decrease the dimensionality of the problem at hand and give a direct connection to established methods from literature. To this end we identify \mathcal{H} with $\mathbb{L}_2(\mathbb{R}^2)$ by means of the operator $\mathcal{S} : \mathcal{H} \rightarrow \mathbb{L}_2(\mathbb{R}^2)$ which is defined by

$$(\mathcal{S}F)(x, \omega) = F(x, \omega, e^{-\pi i x \cdot \omega}) = e^{\pi i x \cdot \omega} F(x, \omega, 1) \quad (5.35)$$

for all $F \in \mathcal{H}$. The space where \mathcal{S} maps to is called phase-space. The inverse of this operator is given by

$$(\mathcal{S}^{-1}\tilde{F})(x, \omega, z) = z^{-1} e^{-\pi i x \cdot \omega} \tilde{F}(x, \omega) \quad (5.36)$$

for all $\tilde{F} \in \mathbb{L}_2(\mathbb{R}^2)$. Here we used a tilde to emphasize that \tilde{F} lives in phase-space. This convention will be used throughout the remainder of this text. Recall that $z = e^{2\pi i s}$ so applying \mathcal{S} to an element of \mathcal{H} amounts to taking the section $s(x, \omega) = -\frac{x \cdot \omega}{2}$. We furthermore note that

$$\mathcal{G}_\psi = \mathcal{S} \circ \mathcal{W}_\psi . \quad (5.37)$$

Now let the phase-space equivalent of the left-invariant operator $\Phi, \tilde{\Phi} : \mathbb{L}_2(\mathbb{R}^2) \rightarrow \mathbb{L}_2(\mathbb{R}^2)$, be defined by conjugation of Φ with \mathcal{S} :

$$\tilde{\Phi} = \mathcal{S} \circ \Phi \circ \mathcal{S}^{-1} . \quad (5.38)$$

Using eq. (5.25) and eq. (5.37) we now have

$$\begin{aligned} \Upsilon_\psi &= (\mathcal{W}_\psi)^* \circ \Phi \circ \mathcal{W}_\psi \\ &= (\mathcal{S} \circ \mathcal{W}_\psi)^{-1} \circ \tilde{\Phi} \circ (\mathcal{S} \circ \mathcal{W}_\psi) \\ &= (\mathcal{G}_\psi)^* \circ \tilde{\Phi} \circ \mathcal{G}_\psi . \end{aligned} \quad (5.39)$$

So left-invariant operators on \mathcal{H} can be directly translated to operators on phase-space such that the effective result on the signal is translation and modulation covariant.

Next consider the phase-space equivalents of the left-invariant vector fields on \mathcal{H} which are presented in eq. (5.33),

$$\begin{aligned} (\tilde{\mathcal{A}}_1 U)(x, \omega) &= (\mathcal{S} \circ \mathcal{A}_1 \circ \mathcal{S}^{-1} U)(x, \omega) = ((\partial_x - 2\pi i \omega) U)(x, \omega) \\ (\tilde{\mathcal{A}}_2 U)(x, \omega) &= (\mathcal{S} \circ \mathcal{A}_2 \circ \mathcal{S}^{-1} U)(x, \omega) = (\partial_\omega U)(x, \omega) \\ (\tilde{\mathcal{A}}_3 U)(x, \omega) &= (\mathcal{S} \circ \mathcal{A}_3 \circ \mathcal{S}^{-1} U)(x, \omega) = (-2\pi i U)(x, \omega) \end{aligned} \quad (5.40)$$

for all smooth functions $U : \mathbb{R}^2 \rightarrow \mathbb{C}$ and all $x, \omega \in \mathbb{R}$. The vector fields $\tilde{\mathcal{A}}_1$ and $\tilde{\mathcal{A}}_3$ are not very practical for direct discretization because of the multiplication operators that appear in their definitions. However, the way we obtained them, viz. by conjugation with \mathcal{S} , will prove useful in the discretization we propose later on.

5.4 Cauchy-Riemann Equations and Window Selection

Up until now we were not very specific about the selection of the window function ψ that is used to obtain a continuous Gabor transform \mathcal{W}_ψ of a signal f . It is of great importance from a practical point of view to select a proper window. There are many reasons to prefer different windows over a Gaussian window as was initially proposed by Gabor [48]. Harris published a paper that summarizes properties of a substantial collection of windows [55]. Despite all considerations in [55] that mostly speak against a Gaussian window function we still stick to the Gaussian because such a window makes the continuous Gabor transform of a signal into an analytic function [22, Chapter 3], [29, 48]. Indeed, if the window function is given by

$$\psi(\xi) = e^{-\pi \xi^2} \quad (5.41)$$

then for $f \in \mathbb{L}_2(\mathbb{R})$ the continuous Gabor transform of $\mathcal{W}_\psi f$ satisfies

$$(\mathcal{A}_2 + i\mathcal{A}_1) \mathcal{W}_\psi f = 0 . \quad (5.42)$$

On phase space we observe that since $\mathcal{G}_\psi f = \mathcal{S} \circ \mathcal{W}_\psi f$,

$$(\tilde{\mathcal{A}}_2 + i\tilde{\mathcal{A}}_1) \mathcal{G}_\psi f = 0 \quad (5.43)$$

also holds, with $\tilde{\mathcal{A}}_1$ and $\tilde{\mathcal{A}}_2$ as defined in eq. (5.40). These relations make the Gaussian window to be preferable since it allows us to relate derivatives of the phase to derivatives of the modulus of a continuous Gabor transform. Using such a construction, branch-cuts in the phase can be avoided which otherwise would have to be tackled by means of a cumbersome phase-unwrapping procedure.

Let $\mathcal{W}_\psi f = |U|e^{i\Omega}$ with ψ as defined in eq. (5.41), with $U = \mathcal{W}_\psi f$, and $\Omega = \arg\{\mathcal{W}_\psi f\}$, then by eq. (5.42)

$$(\mathcal{A}_2 + i\mathcal{A}_1) (|U|e^{i\Omega}) = 0 \Leftrightarrow \mathcal{A}_1\Omega = \frac{\mathcal{A}_2|U|}{|U|} \text{ and } \mathcal{A}_2\Omega = -\frac{\mathcal{A}_1|U|}{|U|} . \quad (5.44)$$

One can indeed compute derivatives of the phase by only considering the amplitude and derivatives thereof.

A phase-space equivalent of eq. (5.44) cannot be obtained by just replacing $\mathcal{A}_1 \leftarrow \tilde{\mathcal{A}}_1$ and $\mathcal{A}_2 \leftarrow \tilde{\mathcal{A}}_2$ since the multiplication operator that appears in $\tilde{\mathcal{A}}_1$ does not satisfy the chain rule. Substituting the definition of the left-invariant vector fields as given in eq. (5.40) into eq. (5.43) and denoting $\mathcal{G}_\psi f = |\tilde{U}|e^{i\tilde{\Omega}}$, $\tilde{U} = \mathcal{G}_\psi f$, and $\tilde{\Omega} = \arg\{\mathcal{G}_\psi f\}$ gives

$$\left(\partial_\omega |\tilde{U}| - |\tilde{U}| \partial_x \tilde{\Omega} + 2\pi\omega |\tilde{U}| + i|\tilde{U}| \partial_\omega \tilde{\Omega} + i\partial_x |\tilde{U}| \right) e^{i\tilde{\Omega}} = 0 . \quad (5.45)$$

Hence we conclude,

$$\tilde{\mathcal{A}}_2 \tilde{\Omega} = -\frac{\partial_x |\tilde{U}|}{|\tilde{U}|} , \quad (5.46)$$

$$\tilde{\mathcal{B}}_1 \tilde{\Omega} = \frac{\tilde{\mathcal{A}}_2 |\tilde{U}|}{|\tilde{U}|} \quad (5.47)$$

are satisfied with

$$\tilde{\mathcal{B}}_1 \tilde{\Omega} = \partial_x \tilde{\Omega} - 2\pi\omega . \quad (5.48)$$

Notice that by using eq. (5.23) one can verify that $\tilde{\mathcal{B}}_1 \circ \arg$ is rather than $\tilde{\mathcal{B}}_1$ a left-invariant vector field.

Now consider the dilation of the window function. To this end we introduce the dilation operator $\mathcal{D}_a : \mathbb{L}_2(\mathbb{R}) \rightarrow \mathbb{L}_2(\mathbb{R})$ which is given by

$$(\mathcal{D}_a(f))(x) = \frac{1}{\sqrt{a}} f(x/a) \quad (5.49)$$

for $f \in \mathbb{L}_2(\mathbb{R})$ and $a > 0$ and define a scaled version of the window ψ as

$$\psi_a(\xi) = e^{-\pi(\frac{\xi}{a})^2} . \quad (5.50)$$

Now

$$(\mathcal{G}_{\psi_a} f)(p, q) = \left(\sqrt{a} \mathcal{G}_{\psi} \mathcal{D}_{\frac{1}{a}} f \right) \left(\frac{x}{a}, a\omega \right) . \quad (5.51)$$

with $\psi = \psi_{a=1}$. By eq. (5.43) and eq. (5.40) we have

$$(\partial_{\omega'} + i(\partial_{x'} - 2\pi i \omega')) \left(\mathcal{G}_{\psi} \mathcal{D}_{\frac{1}{a}} f \right) (x', \omega') = 0 . \quad (5.52)$$

Then by the substitution $x' = \frac{x}{a}$ and $\omega' = a\omega$

$$\left(\frac{1}{a} \partial_{\omega} + i(a \partial_x - 2\pi i a \omega) \right) (\mathcal{G}_{\psi_a} f)(x, \omega) = 0 . \quad (5.53)$$

So the left-invariant vector fields that satisfy the Cauchy-Riemann relations when a window ψ_a is used in the continuous Gabor transform are given by

$$\tilde{\mathcal{A}}_1^a = a \tilde{\mathcal{A}}_1 \text{ and } \tilde{\mathcal{A}}_2^a = a^{-1} \tilde{\mathcal{A}}_2 . \quad (5.54)$$

One can verify that $\mathcal{A}_1^a = a \mathcal{A}_1$ and $\mathcal{A}_2^a = a^{-1} \mathcal{A}_2$ also hold. Furthermore notice that such a scaling also implies that derivatives on the scaled phase Ω^a can be related to derivatives on de scaled modulus $|U^a|$ via

$$\mathcal{A}_1 \Omega^a = a^{-2} \frac{\mathcal{A}_2 |U^a|}{|U^a|} \quad (5.55)$$

$$\mathcal{A}_2 \Omega^a = -a^2 \frac{\mathcal{A}_1 |U^a|}{|U^a|} \quad (5.56)$$

with $(\mathcal{W}_{\psi_a} f) = |U^a| e^{i\Omega^a}$. In the next section the left-invariant vector fields and the just described Cauchy-Riemann relations will be used to define a convection process on the continuous Gabor transform of a signal.

5.5 Reassignment

The first reassignment methods [73, 3] transform the spectrogram $|\mathcal{G}_\psi f|$ into a, in a practical sense, more desirable counterpart in a single step. Later on differential reassignment methods were proposed [23, 22, 29]. These methods perform a deformation of the spectrogram that is guided by some vector field that depends on the spectrogram itself. Differential reassignment¹ is the preferred method for us since we already obtained the tools to perform operations on phase-space such that the net effect on the signal is group-translation covariant.

Let us define a convection process on \mathcal{H} such that the net effect of the signal is (i) translation and modulation covariant and (ii) phase invariant. The latter constraint was introduced in the context of reassignment by Daudet et al. [29] and aims to preserve phase information. This phase information is well known to be carrying much of the signal information [88] and should be handled with care. In order to define a phase invariant convection process we restrict the convection to go along equi-phase isophotes. To this end we introduce a vector \mathbf{v}_U along the equi-phase isophotes of the continuous Gabor transform of a signal $U^a = \mathcal{W}_{\psi_a} f = |U^a| e^{i\Omega^a} \in \mathcal{H}$:

$$\mathbf{v}_{U^a} = (-\mathcal{A}_2 \Omega^a, \mathcal{A}_1 \Omega^a)^T, \quad (5.57)$$

and define a convection process and its initial condition as follows

$$\begin{cases} \partial_t W(g, t) = -C(W(\cdot, t))(g) \\ W(g, 0) = U^a(g) \end{cases}, \quad (5.58)$$

with $g \in H_r$, convection time $t > 0$ and with either

$$C(W(\cdot, t)) = \mathbf{v}_{U^a} \cdot \vec{\mathcal{A}} W(\cdot, t) \quad (5.59)$$

or

$$C(W(\cdot, t)) = \left(a^2 \frac{(\partial_x |W(\cdot, t)|)^2}{|W(\cdot, t)|} + a^{-2} \frac{(\partial_\omega |W(\cdot, t)|)^2}{|W(\cdot, t)|} \right) e^{i\Omega^a}. \quad (5.60)$$

The left-invariant gradient of $W(\cdot, t)$ is given by

$$\vec{\mathcal{A}} W(\cdot, t) = (\mathcal{A}_1 W(\cdot, t), \mathcal{A}_2 W(\cdot, t))^T. \quad (5.61)$$

¹Differential reassignment is a popular term in signal processing for adaptive convection on Gabor transforms.

Notice that the first approach, i.e., eq. (5.59), at $t = 0$ yields

$$C(|U^a|e^{i\Omega^a}) = (-\mathcal{A}_2\Omega^a\mathcal{A}_1|U^a| + \mathcal{A}_1\Omega\mathcal{A}_2|U^a|)e^{i\Omega^a}, \quad (5.62)$$

and by using the Cauchy-Riemann relations eqs. (5.55) and (5.56) that hold because of the specific choice of the window function we have

$$C(|U^a|e^{i\Omega^a}) = \left(a^2 \frac{(\partial_x |U^a|)^2}{|U^a|} + a^{-2} \frac{(\partial_\omega |U^a|)^2}{|U^a|} \right) e^{i\Omega^a}, \quad (5.63)$$

which is clearly phase invariant. As a result eq. (5.59) and eq. (5.60) are the same for $t = 0$. However, since the Cauchy-Riemann relations are not maintained over time the approaches are essentially different. The fact that the Cauchy-Riemann relations do not hold over time directly follows from the preservation of phase and the non-preservation of amplitude.

With respect to the first approach we mention again that the phase is maintained by the convection process so for a practical implementation one can obtain \mathbf{v}_{U^a} at $t = 0$ from the modulus by means of eqs. (5.55) and (5.56). The second approach can be computed in three steps:

1. Store the phase of the initial condition.
2. Apply an erosion to the logarithm of the modulus of the initial condition.
3. Exponentiate the result that was obtained in step 2 and restore the phase that was stored in step 1.

We note that eq. (5.60) reduces in step 2 to

$$\partial_t \log |W(x, \omega, s, t)| = a^2 (\partial_x \log |W(x, \omega, s, t)|)^2 + a^{-2} (\log |W(x, \omega, s, t)|)^2 \quad (5.64)$$

on the modulus. Under the substitution $u = \log |W|$ we arrive at

$$\begin{cases} \partial_t u(x, \omega, t) = a^2 (\partial_x u(x, \omega, t))^2 + a^{-2} (\partial_\omega u(x, \omega, t))^2 \\ u(x, \omega, 0) = \log |U^a|(x, \omega) \end{cases}. \quad (5.65)$$

Such an erosion equation is often encountered in mathematical morphology [108, 110]. It is solved by a morphological convolution

$$u(x, \omega, t) = (|U^a| \ominus b_t)(x, \omega) = \inf_{(x', \omega') \in \mathbb{R}^2} \{ |U^a|(x, \omega) - b_t(x' - x, \omega' - \omega) \} \quad (5.66)$$

using a quadratic structuring element $b_t(x, \omega) = -\frac{a^{-2}x^2 + a^2\omega^2}{4t}$, $t > 0$ [110, 17, 45, 18]. Here we used that $|U^a|$ is independent of s .

On phase-space we obtain equivalent convection equations by conjugation with \mathcal{S} , whence we have

$$\begin{cases} \partial_t \tilde{W}(x, \omega, t) = -\tilde{C}(\tilde{W}(\cdot, t))(x, \omega) \\ \tilde{W}(x, \omega, 0) = \tilde{U}^a(x, \omega) \end{cases} . \quad (5.67)$$

with $\tilde{U}^a = |\tilde{U}^a|e^{i\tilde{\Omega}^a} = \mathcal{G}_{\psi_a} f$ and

$$\tilde{C}(\tilde{W}(\cdot, t)) = -\tilde{\mathcal{A}}_2 \tilde{\Omega}^a \tilde{\mathcal{A}}_1 \tilde{W}(\cdot, t) + \tilde{\mathcal{B}}_1 \tilde{\Omega}^a \tilde{\mathcal{A}}_2 \tilde{W}(\cdot, t) . \quad (5.68)$$

Using the Cauchy-Riemann relations for the initial condition on phase space we observe that the phase-space counterpart of eq. (5.60) reads

$$\tilde{C}(\tilde{W}(\cdot, t)) = \left(a^2 \frac{(\partial_x |\tilde{W}(\cdot, t)|)^2}{|\tilde{W}(\cdot, t)|} + a^{-2} \frac{(\partial_\omega |\tilde{W}(\cdot, t)|)^2}{|\tilde{W}(\cdot, t)|} \right) e^{i\tilde{\Omega}^a} , \quad (5.69)$$

and hence we conclude that the second approach on phase-space is solved in the same manner as its counterpart on the full group.

The left-invariant convection process on phase-space that makes use of eq. (5.68) was also suggested by Daudet et al. [29]. They did however not provide a computational scheme to implement that convection process. Here the results from the previous sections turn out to be crucial. We stress that the developments in the previous sections are essential for a correct implementation of that convection scheme. In the next section we will provide a sound discretization scheme for this convection process where we will essentially follow the same process as before but now for a discrete group.

5.6 Discretization

In this section a discretization of the aforementioned reassignment construction will be presented. First the discretization of the continuous Gabor transform will be considered. To this end the integrals in eq. (5.6) are replaced by a Riemann sum. We will use the nomenclature that is used in

the review paper of Bölcskei et al. [14]. Such a discretization leads to the discrete Gabor transform

$$(\mathcal{W}_{\vec{\psi}_a}^D \vec{f})[l, m, k] = e^{-2\pi i(\frac{k}{Q} - \frac{mL}{2M})} \frac{1}{N} \sum_{n=0}^{N-1} \overline{\vec{\psi}_a^c[n - lL]} \vec{f}[n] e^{-\frac{2\pi i n m}{M}}, \quad (5.70)$$

where we used a D to emphasize this is a discrete transform. Furthermore brackets are used to denote a discrete index. In this transform $L, K, N, M, Q \in \mathbb{N}$, $k = 0, \dots, Q - 1$, $l = 0, \dots, K - 1$, $m = 0, \dots, M - 1$ and $L = \frac{N}{K}$. We also introduce the oversampling factor $P = \frac{M}{L} = \frac{KM}{N}$. This discrete transform transforms a periodic signal that is sampled using N samples onto a discrete grid containing M frequency bands and K samples in the time direction. The discrete signal $\vec{f} = \{\vec{f}[n]\}_{n=0}^{N-1} = \{f(\frac{n}{N})\}_{n=0}^{N-1} \in \mathbb{C}^N$ is a sampled version of the continuous signal. The discrete kernel, which should be N -periodic, is given by

$$\vec{\psi}_a^c = \left\{ \vec{\psi}_a^c[n] \right\}_{n=-(N-1)}^{N-1} = \left\{ e^{-\frac{\pi(|n| - \lfloor \frac{N-1}{2} \rfloor)^2}{N^2 a^2}} \right\}_{n=-(N-1)}^{N-1} \in \mathbb{C}^{2N-1}. \quad (5.71)$$

Here we already explicitly used a discretization of ψ_a that appeared in eq. (5.50). The shift of $\lfloor \frac{N-1}{2} \rfloor$ is introduced for notational convenience. For Riemann-integrable f compactly supported on $[0, 1]$ and the continuous counterpart of $\vec{\psi}_a^c$ we have on the interval $[-1, 1]$,

$$\begin{aligned} (\mathcal{W}_{\vec{\psi}_a}^D \vec{f})[l, m, k] &= e^{-2\pi i(\frac{k}{Q} - \frac{mL}{2M})} \frac{1}{N} \sum_{n=0}^{N-1} e^{-\frac{\pi(|n-lL| - \lfloor \frac{N-1}{2} \rfloor)^2}{N^2 a^2}} f\left(\frac{n}{N}\right) e^{-\frac{2\pi i n m}{M}} \\ &= e^{-2\pi i(\frac{k}{Q} - \frac{mL}{2P})} \frac{1}{N} \sum_{n=0}^{N-1} e^{-\pi a^{-2}(|\frac{n}{N} - \frac{l}{K}| - \frac{1}{N} \lfloor \frac{N-1}{2} \rfloor)^2} f\left(\frac{n}{N}\right) e^{-\frac{2\pi i(K/P)nm}{N}} \\ &\rightarrow e^{-2\pi i(\frac{k}{Q} - \frac{mL}{2P})} \int_0^1 f(\xi) e^{-\pi a^{-2}(|\xi - \frac{l}{K}| - \frac{1}{2})^2} e^{-2\pi i \xi \frac{Km}{P}} d\xi \end{aligned} \quad (5.72)$$

as $N \rightarrow \infty$. Here we identified $x = \frac{l}{K}$, $\omega = \frac{mK}{P}$ and $s = \frac{k}{Q}$. When $N \rightarrow \infty$ we keep K and P fixed, so $M \rightarrow \infty$ resulting in a continuous frequency spectrum.

The cyclic discrete Gabor transform can also be written in a similar form to eq. (5.18), where the Schrödinger representation of the Weyl-Heisenberg group is explicitly used, viz.

$$(\mathcal{W}_{\vec{\psi}}^D \vec{f})[l, m, k] = \left(\mathcal{U}_{[l, m, k]}^D \vec{\psi}, \vec{f} \right)_{l_2(I)}, \quad (5.73)$$

where $I = \{0, \dots, N-1\}$, the discrete inner product for $\vec{f} = \{\vec{f}[n]\}_{n=0}^{N-1}$, $\vec{g} = \{\vec{g}[n]\}_{n=0}^{N-1} \in \mathbb{C}^N$ is given by

$$(\vec{f}, \vec{g})_{l_2(I)} = \frac{1}{N} \sum_{n=0}^{N-1} \overline{\vec{f}[n]} \vec{g}[n], \quad (5.74)$$

and

$$(\mathcal{U}_{[l,m,k]}^D \vec{\psi})[n] = e^{2\pi i(\frac{k}{Q} - \frac{ml}{2P})} e^{\frac{2\pi i n m}{M}} \vec{\psi}[n - lL]. \quad (5.75)$$

To find a group product for the discrete group for which $\mathcal{U}_{[l,m,k]}^D$ is a representation we calculate for all $\vec{\psi} \in l_2(I)$,

$$\begin{aligned} (\mathcal{U}_{[l',m',k']}^D \mathcal{U}_{[l,m,k]}^D \vec{\psi})[n] &= \\ e^{2\pi i(\frac{k'}{Q} - \frac{m'l'}{2P})} e^{\frac{2\pi i n m'}{M}} e^{2\pi i(\frac{k}{Q} - \frac{ml}{2P})} e^{\frac{2\pi i(n-l'L)m}{M}} \vec{\psi}[n - (l+l')L] \\ &= e^{2\pi i(\frac{k+k'}{Q} + \frac{Q}{2P} \frac{(m'l-l'm)}{Q} - \frac{(m+m')(l+l')}{2P})} e^{\frac{2\pi i n(m+m')}{M}} \vec{\psi}[n - (l+l')L] \\ &= \left(\mathcal{U}_{[l+l' \pmod{K}, m+m' \pmod{M}, k+k' + \frac{Q}{2P}(m'l-l'm) \pmod{Q}]}^D \vec{\psi} \right)[n] \end{aligned} \quad (5.76)$$

where we note that $\frac{M}{L} = P$ and we introduce the additional constraints $\frac{Q}{2P}$, L even and $\frac{K}{2P} = \frac{N}{2M} \in \mathbb{N}$ in order to stay on the discrete grid in the k direction. For the rest of this text we will assume all these constraints, which are of almost no burden for practical applications, are satisfied. If the following discrete group product is associated to the discrete reduced Heisenberg group $h_r = \{[l, m, k] \mid l = 0, \dots, K-1, m = 0, \dots, M-1, k = 0, \dots, Q-1\}$

$$\begin{aligned} [l', m', k'] [l, m, k] &= [l + l' \pmod{K}, m + m' \pmod{M}, \\ &\quad k + k' + \frac{Q}{2P}(m'l - l'm) \pmod{Q}] \end{aligned} \quad (5.77)$$

one can see that h_r is a suitable group for the domain of the discrete cyclic Gabor transforms. Indeed,

$$(\mathcal{U}_{[l',m',k']}^D \mathcal{U}_{[l,m,k]}^D \vec{\psi})[n] = (\mathcal{U}_{[l+l', m+m', k+k' + \frac{Q}{2P}(m'l-l'm)]}^D \vec{\psi})[n] \quad (5.78)$$

is satisfied for all $\vec{\psi} \in l_2(I)$.

5.6.1 Discrete Left-Invariant Vector Fields

The reassignment method that corresponds to eq. (5.59) in Section 5.5 heavily depends on the left-invariant vector fields that were presented in Section 5.3.1. One should therefore take care to carefully construct these vector fields in the discretization of the method. Failure of doing so would result in a method that is not covariant with respect to translations or modulations of the input signal, which is highly undesirable. Straight-forward discretization of the vector fields in eq. (5.33) does not suffice. Therefore we took care in the beginning of this section to introduce a discrete group that corresponds to the continuous group \mathcal{H}_r for which we can compute the discrete counterparts of the vector fields that are presented in eq. (5.33). We will now follow a similar construction as was used on \mathcal{H}_r , viz. taking the derivative of the right-regular representation, to obtain the discrete left-invariant vector fields. Here we recall that such operators are indeed left-invariant since left and right-regular actions commute.

In the discretized algorithm an upwind scheme will be employed that uses both forward and backward finite differences. Therefore we will calculate both the forward and backward discrete left-invariant vector fields on discrete Gabor transforms. The forward discrete left-invariant vector fields \mathcal{A}_i^{D+} $i = 1 \dots 3$, where the $+$ superscript to D is used to emphasize the fact that the finite difference operator is taken in the forward direction, are given by (cf. eq. (5.77))

$$\begin{aligned} \left(\mathcal{A}_1^{D+} \mathcal{W}_{\vec{\psi}}^D \vec{f} \right) [l, m, k] &= \frac{\left(\mathcal{W}_{\vec{\psi}}^D \vec{f} \right) [[l, m, k][1, 0, 0]] - \left(\mathcal{W}_{\vec{\psi}}^D \vec{f} \right) [l, m, k]}{K^{-1}} \\ &= \frac{e^{-\frac{\pi i m L}{M}} \left(\mathcal{W}_{\vec{\psi}}^D \vec{f} \right) [l+1, m, k] - \left(\mathcal{W}_{\vec{\psi}}^D \vec{f} \right) [l, m, k]}{K^{-1}} \end{aligned} \quad (5.79)$$

$$\begin{aligned} \left(\mathcal{A}_2^{D+} \mathcal{W}_{\vec{\psi}}^D \vec{f} \right) [l, m, k] &= \frac{\left(\mathcal{W}_{\vec{\psi}}^D \vec{f} \right) [[l, m, k][0, 1, 0]] - \left(\mathcal{W}_{\vec{\psi}}^D \vec{f} \right) [l, m, k]}{NM^{-1}} \\ &= \frac{e^{\frac{\pi i m L}{M}} \left(\mathcal{W}_{\vec{\psi}}^D \vec{f} \right) [l, m+1, k] - \left(\mathcal{W}_{\vec{\psi}}^D \vec{f} \right) [l, m, k]}{NM^{-1}} \end{aligned} \quad (5.80)$$

$$\begin{aligned} \left(\mathcal{A}_3^{D+} \mathcal{W}_{\vec{\psi}}^D \vec{f} \right) [l, m, k] &= \frac{\left(\mathcal{W}_{\vec{\psi}}^D \vec{f} \right) [[l, m, k][0, 0, 1]] - \left(\mathcal{W}_{\vec{\psi}}^D \vec{f} \right) [l, m, k]}{Q^{-1}} \\ &= Q \left(e^{-\frac{2\pi i}{Q}} - 1 \right) \left(\mathcal{W}_{\vec{\psi}}^D \vec{f} \right) [l, m, k], \end{aligned} \quad (5.81)$$

for all $\vec{f} \in \mathbb{C}^N$, $\vec{\psi} \in \mathbb{C}^N$ and $[l, m, k] \in h_r$. We note that this are just finite differences using right-shifts on h_r . Notice this is the discrete equivalent of

eq. (5.29). The backward discrete left-invariant vector fields \mathcal{A}_i^{D-} $i = 1, 2, 3$ are obtained in a similar fashion. These vector fields are given by

$$\left(\mathcal{A}_1^{D-} \mathcal{W}_\psi^D \vec{f}\right)[l, m, k] = \frac{\left(\mathcal{W}_\psi^D \vec{f}\right)[l, m, k] - e^{\frac{\pi i m L}{M}} \left(\mathcal{W}_\psi^D \vec{f}\right)[l-1, m, k]}{K-1} \quad (5.82)$$

$$\left(\mathcal{A}_2^{D-} \mathcal{W}_\psi^D \vec{f}\right)[l, m, k] = \frac{\left(\mathcal{W}_\psi^D \vec{f}\right)[l, m, k] - e^{-\frac{\pi i m L}{M}} \left(\mathcal{W}_\psi^D \vec{f}\right)[l, m-1, k]}{NM-1} \quad (5.83)$$

$$\left(\mathcal{A}_3^{D-} \mathcal{W}_\psi^D \vec{f}\right)[l, m, k] = Q \left(1 - e^{\frac{2\pi i}{Q}}\right) \left(\mathcal{W}_\psi^D \vec{f}\right)[l, m, k]. \quad (5.84)$$

Centered discrete left-invariant vector fields can be obtained by averaging the corresponding forward and backward left-invariant vector fields. Notice these operators are exact on h_r and no interpolation is needed. It can be shown that for $N \rightarrow \infty$ they converge to their continuous counterparts [40].

5.6.2 Phase-Space

To obtain a dimension reduction we introduce a discrete version of \mathcal{S} (recall eqs. (5.35) and (5.18)), $\mathcal{S}^D : R(\mathcal{W}_\psi^D) \rightarrow l_2(\{0, \dots, K-1\} \times \{0, \dots, M-1\})$. Clearly this mapping maps a discrete Gabor transform to its phase space representation

$$\left(\mathcal{G}_\psi^D \vec{f}\right)[l, m] = \frac{1}{N} \sum_{n=0}^{N-1} \overline{\psi[n-lL]} \vec{f}[n] e^{-\frac{2\pi i(n-l)m}{M}} \quad (5.85)$$

and is given by

$$\left(\mathcal{G}_\psi^D \vec{f}\right)[l, m] = \left(\mathcal{S}^D \mathcal{W}_\psi^D \vec{f}\right)[l, m] = \left(\mathcal{W}_\psi^D \vec{f}\right)\left[l, m, -\frac{lmQ}{2P}\right]. \quad (5.86)$$

Its inverse is given by

$$\left(\mathcal{W}_\psi^D \vec{f}\right)[l, m, k] = \left((\mathcal{S}^D)^{-1} \mathcal{G}_\psi^D \vec{f}\right)[l, m, k] = e^{-2\pi i(\frac{k}{Q} + \frac{lmL}{2M})} \left(\mathcal{G}_\psi^D \vec{f}\right)[l, m]. \quad (5.87)$$

Using this mapping, namely via conjugation, the discrete left-invariant vector fields on phase space, $\tilde{\mathcal{A}}_i^{D+}$ and $\tilde{\mathcal{A}}_i^{D-}$ $i = 1, 2, 3$, can be obtained from the discrete left-invariant vector fields that were obtained in the previous subsection. The forward discrete left-invariant vector fields on phase space

are

$$\begin{aligned} (\tilde{\mathcal{A}}_1^{D+} \mathcal{G}_\psi^D \vec{f})[l, m] &= ((S^D) \circ \mathcal{A}_1^{D+} \circ (S^D)^{-1} \mathcal{G}_\psi^D \vec{f})[l, m] \\ &= \frac{e^{-\frac{2\pi i m L}{M}} (\mathcal{G}_\psi^D \vec{f})[l+1, m] - (\mathcal{G}_\psi^D \vec{f})[l, m]}{K^{-1}} \end{aligned} \quad (5.88)$$

$$\begin{aligned} (\tilde{\mathcal{A}}_2^{D+} \mathcal{G}_\psi^D \vec{f})[l, m] &= ((S^D) \circ \mathcal{A}_2^{D+} \circ (S^D)^{-1} \mathcal{G}_\psi^D \vec{f})[l, m] \\ &= \frac{(\mathcal{G}_\psi^D \vec{f})[l, m+1] - (\mathcal{G}_\psi^D \vec{f})[l, m]}{NM^{-1}} \end{aligned} \quad (5.89)$$

$$\begin{aligned} (\tilde{\mathcal{A}}_3^{D+} \mathcal{G}_\psi^D \vec{f})[l, m] &= ((S^D) \circ \mathcal{A}_3^{D+} \circ (S^D)^{-1} \mathcal{G}_\psi^D \vec{f})[l, m] \\ &= Q \left(e^{-\frac{2\pi i}{Q}} - 1 \right) (\mathcal{G}_\psi^D \vec{f})[l, m] \end{aligned} \quad (5.90)$$

for all $\vec{f} \in \mathbb{C}^N$ and $\vec{\psi} \in \mathbb{C}^N$ and $[l, m] \in \{0, \dots, K-1\} \times \{0, \dots, M-1\}$. The backward discrete left-invariant vector fields are computed in the same manner and read

$$(\tilde{\mathcal{A}}_1^{D-} \mathcal{G}_\psi^D \vec{f})[l, m] = \frac{(\mathcal{G}_\psi^D \vec{f})[l, m] - e^{\frac{2\pi i m L}{M}} (\mathcal{G}_\psi^D \vec{f})[l-1, m]}{K^{-1}} \quad (5.91)$$

$$(\tilde{\mathcal{A}}_2^{D-} \mathcal{G}_\psi^D \vec{f})[l, m] = \frac{(\mathcal{G}_\psi^D \vec{f})[l, m] - (\mathcal{G}_\psi^D \vec{f})[l, m-1]}{NM^{-1}} \quad (5.92)$$

$$(\tilde{\mathcal{A}}_3^{D-} \mathcal{G}_\psi^D \vec{f})[l, m] = Q \left(1 - e^{\frac{2\pi i}{Q}} \right) (\mathcal{G}_\psi^D \vec{f})[l, m] \quad (5.93)$$

for all $\vec{f} \in \mathbb{C}^N$ and $\vec{\psi} \in \mathbb{C}^N$ and $[l, m] \in \{0, \dots, K-1\} \times \{0, \dots, M-1\}$. Now formally on phase-space one should still adhere to the restrictions that were posed on L, K, M and Q earlier in this section, otherwise the left-invariant vector fields do not correspond to an underlying discrete group. However in practice these restrictions can be violated since the k direction is not visible to the operators that act on phase-space.

5.6.3 Discrete Cauchy-Riemann Equations and Sampled Windows

It was pointed out in Section 5.4 that the selection of a certain windowing function $\psi \in \mathbb{L}_2(\mathbb{R})$ for the continuous Gabor transform leads to favorable properties of such a transform. Namely derivatives of the phase can be

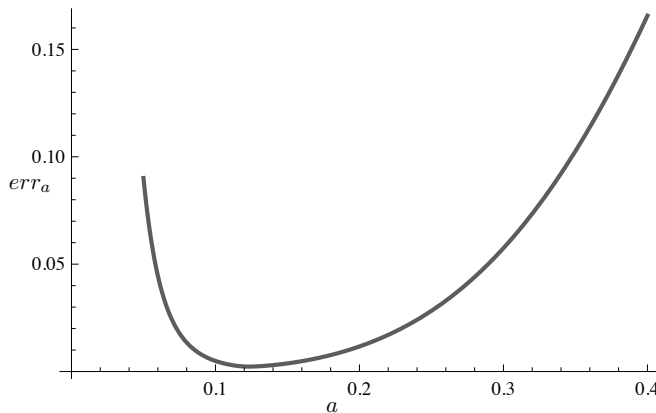


Figure 5.1: The relative error ϵ_a that shows how well the Cauchy-Riemann relations hold for central discrete left-invariant vector fields on the Gabor transform of a chirp signal as a function of a for a practical range of a . The analysis window that is used to obtain the Gabor transform of a chirp signal is a sampled version of the window function that is optimal for the continuous case.

related to derivatives of the amplitude, cf. eqs. (5.42) and (5.43). To quantify how well these relations hold in the discrete setting we sample ψ_a in eq. (5.50) as in eq. (5.71) and use it to obtain a discrete Gabor transform of an arbitrary signal \vec{f} . Next we verify to which extent

$$\left(a^{-1}\tilde{\mathcal{A}}_2^D + ai\tilde{\mathcal{A}}_1^D\right)\left(\mathcal{G}_{\vec{\psi}_a}^D \vec{f}\right) = 0 \quad (5.94)$$

holds as a function of scale $a > 0$. Here $\tilde{\mathcal{A}}_i^D = \frac{1}{2}\left(\tilde{\mathcal{A}}_i^{D+} + \tilde{\mathcal{A}}_i^{D-}\right)$, $i = 1, 2$ denotes a discrete left-invariant central finite difference operator. The scaling directly corresponds to the scaling in the continuous case. The relative error as a function of a ,

$$\epsilon_a(\vec{f}) = \frac{\left\| \left(a^{-1}\tilde{\mathcal{A}}_2^D + ai\tilde{\mathcal{A}}_1^D\right)\left(\mathcal{G}_{\vec{\psi}_a}^D \vec{f}\right) \right\|^2}{\|\vec{f}\|^2}, \quad (5.95)$$

is depicted in Figure 5.1. To produce this figure we have taken \vec{f} to be a sampled version of a linear chirp function such that there are responses for large frequency and time ranges in the discrete Gabor transform that is used in the error measure. The measured errors are rather large, especially for relatively large or small a . A graph of several sampled windows for different values of a together with sampled windows that do satisfy eq. (5.94)

exactly can be found in Figure 5.2. From this figure one can clearly see that taking too few samples relative to the scale a as well as a too large a relative to the number of samples N used in the discretization lead to numerical problems.

Even for an optimal a in the example of Figure 5.1, i.e., that a that corresponds to the smallest ϵ_a , the relative error is not satisfactory. Therefore we proceed by finding a kernel such that the Cauchy-Riemann relations do hold in the specific case of discrete left-invariant centered differences. To this end a linear system of equations for a scale a of interest is numerically solved. The obtained solution now serves as the window function for the discrete Gabor transform.

To compute an optimal window one can, because of linearity and left-invariance, consider the transform of $\vec{\delta}_n = \{\delta_{0n}\}_{n=0}^{N-1}$, with δ_{ij} the Kronecker delta function ($\delta_{ij} = 1$ if $i = j$, 0 otherwise), and optimize for that function. So we search for $\vec{\psi}_a^d$ such that

$$\left(a^{-1}\tilde{\mathcal{A}}_2^D + ai\tilde{\mathcal{A}}_1^D\right)\left(\mathcal{G}_{\vec{\psi}_a^d}^D\vec{\delta}_n\right) = 0, \quad (5.96)$$

which leads to

$$\begin{aligned} \left(a^{-1}\tilde{\mathcal{A}}_2^D + ai\tilde{\mathcal{A}}_1^D\right)\left(\frac{1}{N}\overline{\vec{\psi}_a^d[-lL]}e^{\frac{2\pi ilm}{M}}\right) = \\ \frac{M}{2aN^2}\overline{\vec{\psi}_a^d[-lL]}e^{2\pi ilm\frac{L}{M}}\left(e^{2\pi il\frac{L}{M}} - e^{-2\pi il\frac{L}{M}}\right) \\ + i\frac{aK}{2N}e^{2\pi ilm\frac{L}{M}}\left(\overline{\vec{\psi}_a^d[-(l+1)L]} - \overline{\vec{\psi}_a^d[-(l-1)L]}\right) \\ (5.97) \\ = \frac{1}{N}e^{2\pi ilm\frac{L}{M}}\left(\frac{M}{aN}\sin(2\pi l\frac{L}{M})\overline{\vec{\psi}_a^d[-lL]} \right. \\ \left. + \frac{aK}{2}\left(\overline{\vec{\psi}_a^d[-(l+1)L]} - \overline{\vec{\psi}_a^d[-(l-1)L]}\right)\right) = 0. \end{aligned}$$

This should hold for all $l = 0, \dots, K-1$ and $m = 0, \dots, M-1$, but since the m variable only appears as a modulation factor it suffices to solve the system for all l and a fixed m . In order to exclude the trivial solution $\vec{\psi}_a^d = 0$ the constraint

$$\sum_{l=0}^{K-1} \vec{\psi}_a^d[l] = 1 \quad (5.98)$$

is also included. This system of equations can be represented using a tridiagonal matrix in which also the cyclic boundary conditions are expressed. Such a system of equations is easily solved [99]. Windows we calculated for different values of a can be found in Figure 5.2. A graph of the relative errors (5.95) made using these windows is not presented since the errors are close to machine precision. For example, for $a = \frac{1}{8}$ the relative error is of the order 10^{-18} in our implementation. We do however notice that the forward and backward discrete left-invariant finite differences do not satisfy the discrete Cauchy-Riemann equations when the optimized window for central differences is used. A graph of the errors made when using either forward or backward differences can be found in Figure 5.3. These errors overlap due to symmetry.

5.6.4 Discrete Reassignment on Phase-Space

The discrete Gabor transforms we used in our implementation of the reassignment algorithm are based on the Zak transform. Such algorithms are known for their computational efficiency. Since this is well established theory but still necessary for a self-contained presentation of our work we refer to Appendix C.1 in which the diagonalization of the frame operator that appears in the discrete Gabor transform and the construction of the synthesis windows that are used in the reconstruction are addressed. One should be aware that the discrete synthesis windows are, in contrast to the continuous windows, not just the complex conjugated versions of the analysis windows.

For the discrete implementation of the reassignment procedure on phase space we will use an upwind scheme [84, 96, 89]. Such schemes are often used in mathematical morphology [109, 16]. A favorable property of this scheme is that it does not introduce new maxima during computation. We do note however that the scheme suffers from numerical blurring, which can be overcome [16, 84] at the expense of other imperfections such as phase errors and under and overshoot. The morphological convolution that was used in the erosion process (see Section 5.5) is trivially discretized and will not be elaborated on.

The vector field \vec{v}^D along which the convection will take place is calculated using finite differences, where we make use of the Cauchy-Riemann relations, i.e., the vector field at grid position $(l, m) \in \{0, \dots, K-1\} \times$

$\{0, \dots, M-1\}$ and time $t > 0$ is given by

$$\vec{v}^D = \left(\frac{a^2}{2K} \left((\log |\tilde{W}^D|) [l+1, m] - (\log |\tilde{W}^D|) [l-1, m] \right), \right. \\ \left. (\log |\tilde{W}^D| [l, m+1] - \log |\tilde{W}^D| [l, m-1]) \right) \quad (5.99)$$

with $\tilde{W}^D[l, m, 0] = (\mathcal{G}_{\vec{\psi}}^D \vec{f})[l, m]$. Recall this vector field points in a direction that is orthogonal to the gradient of the phase. Using

$$z^+(\phi)[l, m, t] = \max\{\phi[l, m, t], 0\} \quad (5.100)$$

and

$$z^-(\phi)[l, m, t] = \min\{\phi[l, m, t], 0\} \quad (5.101)$$

$$(5.102)$$

a decision is made between forward and backward derivatives per position $[l, m]$ and convection time grid point t . In the time direction we simply apply a forward Euler method with time step τ . Denoting $\vec{v}^D = (v_1^D, v_2^D)$ this gives an expression for the reassigned discrete Gabor transform at time $t + \tau$ based on \tilde{W}^D at time t :

$$\tilde{W}^D[l, m, t + \tau] = \tilde{W}^D[l, m, t] \quad (5.103)$$

$$- \tau \left((z^+(v_1^D)[l, m, t] (\tilde{\mathcal{A}}_1^{D-}) [l, m, t] z^-(v_1^D)[l, m, t] (\tilde{\mathcal{A}}_1^{D+}) [l, m, t]) \right. \\ \left. + (z^+(v_2^D)[l, m, t] (\tilde{\mathcal{A}}_2^{D-}) [l, m, t] + z^-(v_2^D)[l, m, t] (\tilde{\mathcal{A}}_2^{D++}) [l, m, t]) \right).$$

Notice the calculations are done on the complex valued discrete Gabor transform and not just on its modulus. The reassignment process could be implemented on the modulus only, as we suggested in the erosion scheme. We chose however to implement it this way so we can verify our discretization scheme and show the feasibility of the proposed method that acts on the full Gabor transform and not just its modulus.

5.7 Evaluation

To evaluate the proposed methods we apply both reassignment schemes to the reassignment of a linear chirp that is multiplied by a modulated

Gaussian and is sampled using $N = 128$ samples. The input signal is an analytic signal so it suffices to show its Gabor transform from 0 to π . A visualization of this complex valued signal can be found in Figure 5.4. For all experiments we have set the grid parameters $K = M = N = 128$, which implies $P = 128$ and $L = 1$. The scale of the window functions is set to $a = \frac{1}{6}$.

Figure 5.5 shows several reconstructions of the reassigned Gabor transforms that are shown in Figure 5.6. To produce the left most column of Figure 5.5 the window $\vec{\psi}_a^c$ was used and to produce the right most column $\vec{\psi}_a^d$ was used as a window. The top row in this figure corresponds to the PDE based convection scheme and the bottom row corresponds to the erosion scheme.

The reassigned Gabor transforms in Figure 5.6 are obtained by, from top to bottom, the PDE scheme using $\vec{\psi}_a^c$, the PDE scheme using $\vec{\psi}_a^d$, the erosion scheme using $\vec{\psi}_a^c$ and finally the erosion scheme using $\vec{\psi}_a^d$. The time parameter to produce Figures 5.5 and 5.6 is set to $t = 0.1$ and the time step for the PDE based method is set to $\tau = 10^{-3}$. The signals are scaled such that their energy equals the energy of the input signal. This is needed to correct for the numerical diffusion the discretization scheme suffers from. Reassignment should only *reassign* “time frequency particles”, therefore we argue it is justified to compare the methods in such a way that the energy appears to be conserved.

Clearly the reassigned signals resemble the input signal quite well. There is a difference between the reconstructions of the Gabor transforms using different windows that were reassigned by the erosion based method. To study the differences Figure 5.7 shows the modulus of the input signal together with the moduli of the reconstructed reassigned signals that were produced using the erosion method. From this figure we conclude that it is preferable to use $\vec{\psi}_a^c$ as a window in order to better preserve the signal. Numerical results support this observation. We also notice from Figure 5.6 the erosion method is sensitive to the selection of the window function.

Table 5.7 shows the relative errors of the complex valued reconstructed

signal ϵ_1 , and the relative error of its modulus ϵ_2 , i.e.,

$$\epsilon_1 = \frac{\|\vec{u} - \vec{v}\|_{l_2(I)}^2}{\|\vec{u}\|_{l_2(I)}^2}, \quad (5.104)$$

$$\epsilon_2 = \frac{\| |\vec{u}| - |\vec{v}| \|_{l_2(I)}^2}{\|\vec{u}\|_{l_2(I)}^2} \quad (5.105)$$

with \vec{u} the sampled input signal and \vec{v} the reconstructed reassigned signal. The table also includes one extra experiment, where the convection time for the PDE scheme using $\vec{\psi}_a^d$ is set to $t = 0.16$. As can be seen in Table 5.7 the PDE scheme using $\vec{\psi}_a^d$ as a window gives less signal distortion then when $\vec{\psi}_a^c$ is used. We can however not compare the erosion and PDE schemes directly since they are essentially different methods. Figure 5.6 shows the PDE scheme sharpens the Gabor transform of the signal much more slowly then the erosion scheme. To compare both methods we included the last experiment in the table where we stopped the convection when it reached an error that is comparable to the error produced by the erosion scheme using $\vec{\psi}_a^c$ as window. A visualization of the modulus of reassigned Gabor transform with $t = 0.16$ and window $\vec{\psi}_a^d$ can be found in Figure 5.8.

The PDE scheme performs best when the window $\vec{\psi}_a^d$ is used and the erosion scheme performs better when the window $\vec{\psi}_a^c$ is used. Erosion leads to sharper reassigned Gabor transforms compared to the reassigned Gabor transforms that are obtained using a the PDE scheme where both schemes show a comparable error. Furthermore one should note that the implementation of the erosion scheme is much easier and also much faster than the PDE scheme. Because of the separability of the erosion kernel it is also trivial to compute the erosion in a parallel fashion.

5.8 Conclusions

We showed how to reassign a Gabor transform of a signal using left-invariant derivatives. This lead to two left-invariant methods that are effectively covariant with respect to translations and modulations of the input signal. By directing the convection process that is used to deform the signal in the Gabor domain in a direction that is orthogonal to the left-invariant gradient of its phase, the methods are also phase invariant. This

	ϵ_1	ϵ_2	t
Erosion $\vec{\psi}_a^c$	2.4110^{-2}	8.3810^{-3}	0.1
Erosion $\vec{\psi}_a^d$	8.2510^{-2}	7.8910^{-2}	0.1
PDE $\vec{\psi}_a^c$	2.1610^{-2}	2.2110^{-3}	0.1
PDE $\vec{\psi}_a^d$	1.4710^{-2}	3.3210^{-4}	0.1
PDE $\vec{\psi}_a^d$	2.4310^{-2}	6.4310^{-3}	0.16

Table 5.1: The first column shows ϵ_1 , the relative error of the complex valued reconstructed signal compared to the input signal. In the second column ϵ_2 can be found which represents the relative error of the modulus of the signals. The rows show the methods that were used in the reassignment of the chirp signal. Parameters involved are grid constants $K = M = N = 128$, window scale $a = \frac{1}{8}$ and the convection time $t = 0.1$. The time step for the forward Euler method is set to $\tau = 10^{-3}$ if applicable. PDE means the upwind scheme that is presented in Section 5.6.4 is used and erosion means the morphological erosion method that is presented Section 5.5 is used in the computations.

leads to two methods that, in contrast to the representation of the signal in the Gabor domain, only slightly change the signal itself. Thus the reassignment method can be used to produce a more localized time-frequency representation of the original input signal.

To compute the gradient of the phase, Cauchy-Riemann relations are used that only hold when a specific window is used. A discretization of this window is proposed which ensures the Cauchy-Riemann relations are maintained in the discrete setting. The alternative discretization, straight forward sampling of the window that was derived in the continuous case, does not maintain the discrete Cauchy-Riemann relations.

We furthermore identify a discrete group that corresponds to the continuous one in order to discretize the left-invariant vector fields that are used in the reassignment method. This leads to discrete left-invariant vector fields that are used in the implementation of the PDE based reassignment scheme. This also allows us to correctly implement a method that was only theoretically presented in [29].

Next to the PDE based convection scheme we also propose a method that can be implemented by means of a morphological erosion operation on the logarithm of the modulus of the Gabor transform of a signal. Such an erosion method has the advantage it can be implemented using a fast

separable scheme. It also produces sharper reassignments compared to the PDE scheme.

Experiments show that for the erosion scheme the best window is a sampled version of the window that is optimal in the continuous case and for the PDE scheme the newly derived window gives better performance.

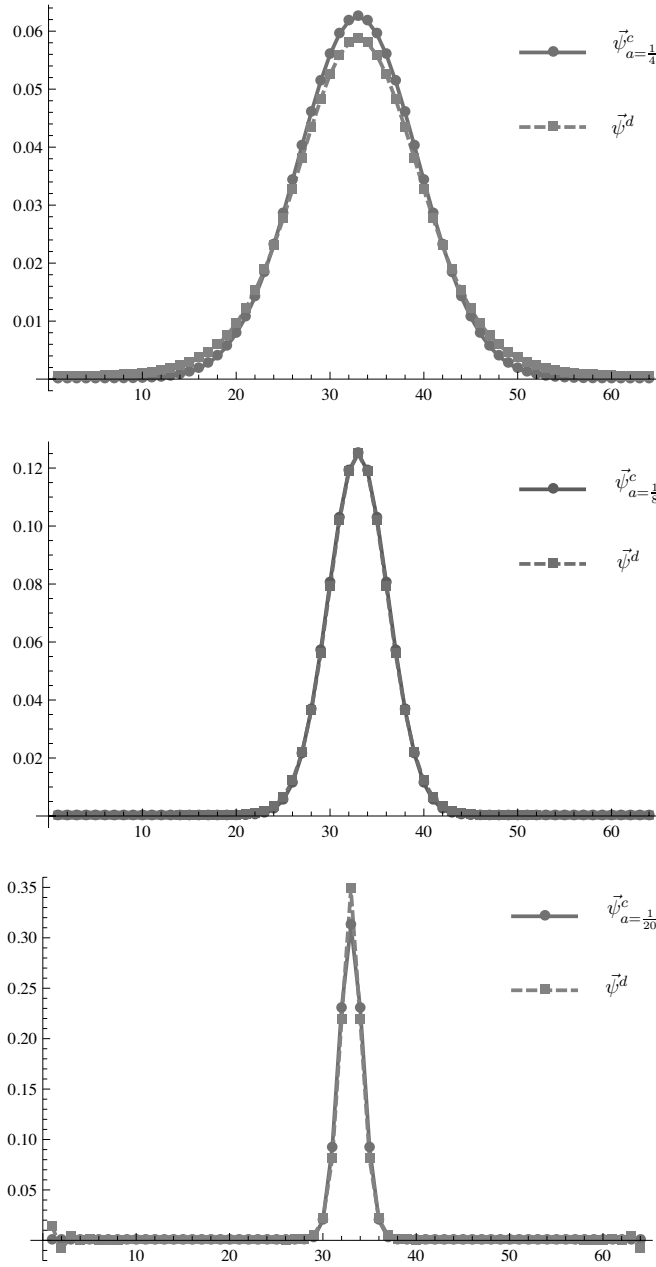


Figure 5.2: From top to bottom the sampled continuous windows and the discrete windows that are optimized for central discrete left-invariant vector fields using parameter a set to $\frac{1}{4}, \frac{1}{8}, \frac{1}{20}$ respectively. Clearly the sampled window deviates from the optimal one when for both $a = \frac{1}{4}$ and $a = \frac{1}{20}$.

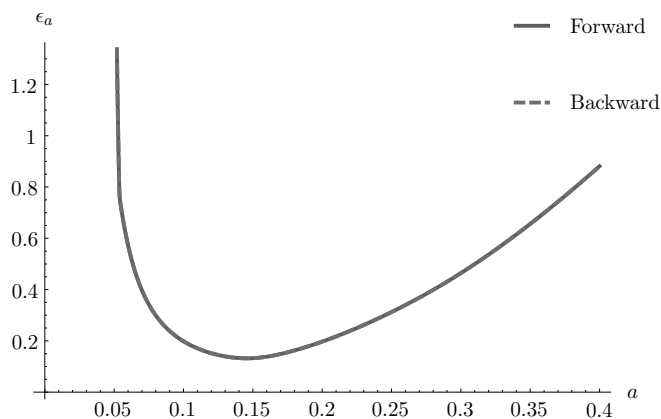


Figure 5.3: The relative error ϵ_a that shows how well the Cauchy-Riemann relations hold for forward and backward discrete left-invariant vector fields on the Gabor transform of a chirp signal as a function of a for practical range of a . The analysis window that is used to obtain the Gabor transform of a chirp signal is an optimal window for central discrete left-invariant vector fields.

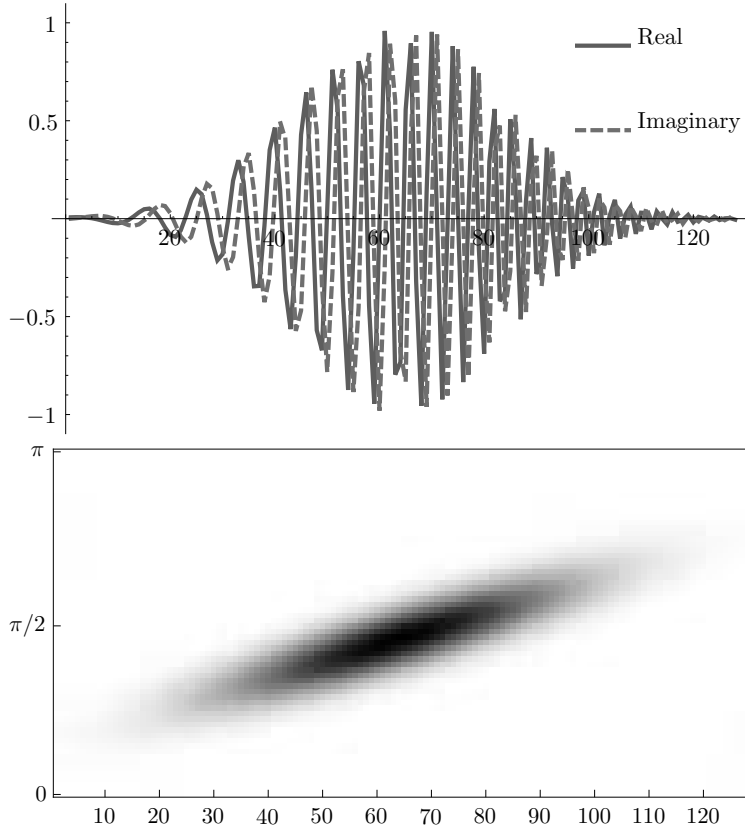


Figure 5.4: On top a chirp signal that is multiplied by a modulated Gaussian is shown. The bottom image shows the modulus of the Gabor transform of the complex valued signal that is shown on top. Parameters for the transform are $K = M = N = 128$ and $a = \frac{1}{6}$. As a window $\vec{\psi}_a^d$ was used.

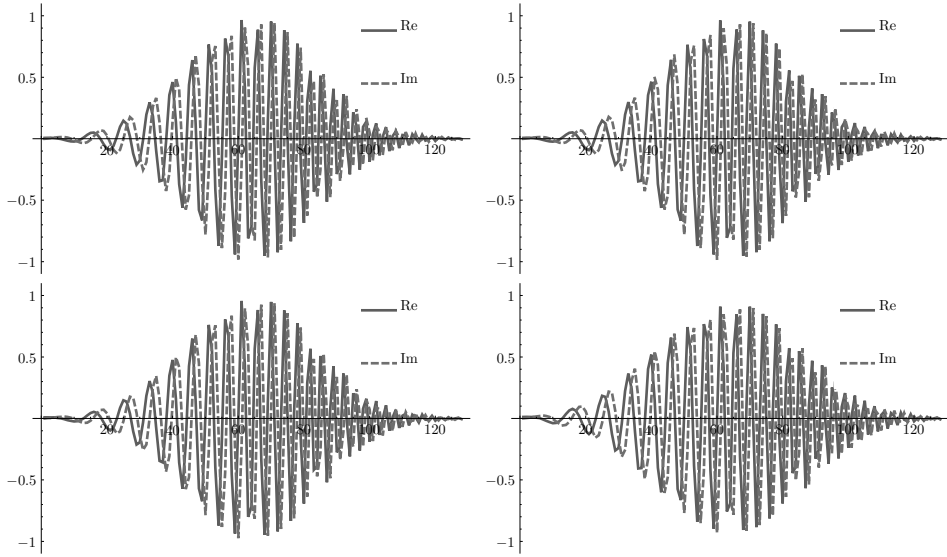


Figure 5.5: Reconstructions of the reassigned Gabor transforms of the signal that is depicted in Figure 5.4. The left column is produced using $\vec{\psi}_a^c$ as window and the right column is produced using $\vec{\psi}_a^d$ as window. The top row was produced using the PDE based method and the bottom row was produced using the erosion based method. Parameters involved are grid constants $K = M = N = 128$, window scale $a = \frac{1}{6}$ time step $\tau = 10^{-3}$ and the convection time $t = 0.1$.

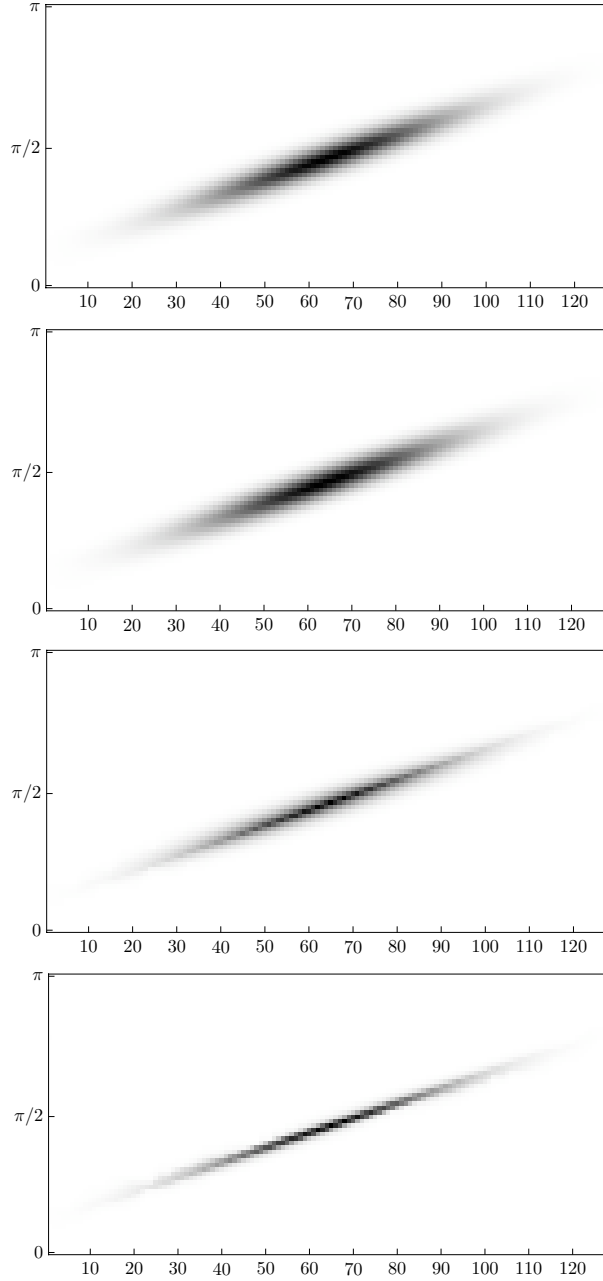


Figure 5.6: The moduli of the reassigned Gabor transforms that correspond to the signals in Figure 5.5. From top to bottom the PDE scheme using ψ_a^c , the PDE scheme using $\tilde{\psi}_a^c$, the erosion scheme using $\tilde{\psi}_a^c$ and finally the erosion scheme using $\tilde{\psi}_a^d$ are shown. Parameters involved are grid constants $K = M = N = 128$, window scale $a = \frac{1}{6}$ time step $\tau = 10^{-3}$ and the convection time $t = 0.1$.

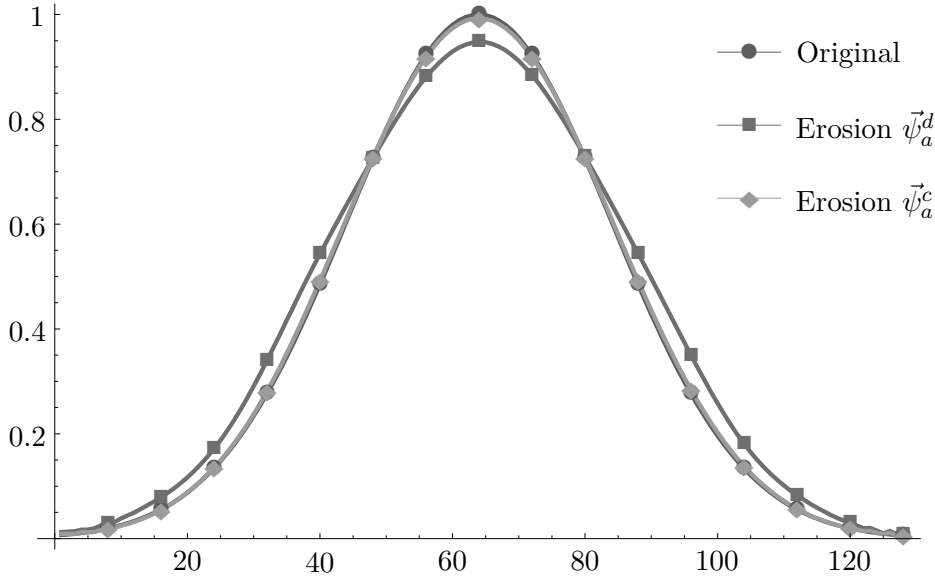


Figure 5.7: The modulus of the input signal together with the moduli of the reconstructed reassigned signals that were produced using the erosion method using $\vec{\psi}_a^d$ and $\vec{\psi}_a^c$ as a window.

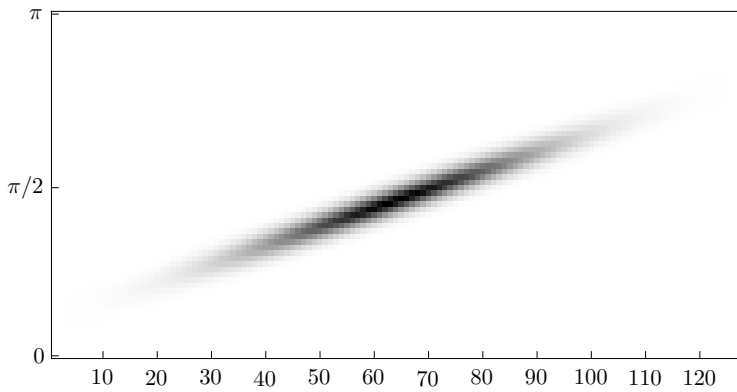


Figure 5.8: The modulus of the reassigned Gabor transform that corresponds to the experiment listed in the bottom most row of Table 5.7 ($t = 0.16, \tau = 10^{-3}$, window: $\vec{\psi}_{a=\frac{1}{6}}^d$). This figure should be compared to the third image in Figure 5.6.

Left-Invariant Diffusion on the Heisenberg Group

6.1 Introduction

In Chapter 5 we showed how one can enhance an over-sampled Gabor transform of a signal, in the sense that it is easier to interpret, such that the corresponding action in the signal domain is close to the identity operation. The machinery that was presented in that chapter can also be used for enhancement in the Gabor domain such that the represented signal itself is enhanced. By using operators on the domain of Gabor transforms that are left-invariant the corresponding enhancement operator on the signal domain will be translation and modulation covariant.

Enhancement of signals via processing in transform domains is not new. Thresholding of wavelet coefficients [32], which is also called wavelet shrinkage, is common practice for de-noising of, e.g., images. Yu et al. [122] noticed that in case of audio de-noising, which is often done using over-sampled Gabor transforms, artifacts arise when simple thresholding operations are performed. Those artifacts are known as “musical noise” [21]. In [122] it is shown that it is beneficial to apply a block based thresholding method, thus adapting the attenuation factor based on information in the direct neighborhood of the coefficients to be thresholded. Thresholding methods produce satisfying results because they apply phase-covariant operators in the transform domain. That is, wavelet shrinkage is, like the reassignment methods that were presented in the previous chapter, both phase-invariant and phase-covariant. Those methods however do not take advantage of the group structure that is present on the domain of Gabor transforms and can only handle local spatial and frequency information in a crude manner, i.e., by block thresholding.

Another popular method for the enhancement of images is the application of a diffusion process to the image to be enhanced, where the amount of diffusion is adapted to the local structure of the image. Perona and Malik [91] proposed such a method. Their method inhibits diffusion near edge-like structures. As a result edges are preserved but homogeneous areas are smoothed. Following the general idea in [91], where isotropic non-linear diffusion is applied, many other researchers proposed diffusion processes that also incorporate the local direction of the structure, resulting in truly anisotropic diffusion processes [87, 25, 113]. Weickert [114] proposed coherence enhancing diffusion, where he steers the diffusion in the direction of flow-like structures. The diffusion based methods however cannot take advantage of transform domain representations, in which local

structure is “pried apart” into distinctive constituents. For example, the superposition of two tones (sinusoids of different frequency) gets separated in the Gabor domain while in the spatial domain alone they heavily interfere. We also note that for a very artificial case wavelet shrinkage and non-linear adaptive diffusion on the image domain can be related to each other [116, 115].

Combining the two approaches (transform domain processing and adaptive diffusion) can be very advantageous. Franken and Duits [46, 47, 39] recently showed that the enhancement of crossing elongated structures can indeed be done using such an approach and has advantages compared to coherence enhancing diffusion on the image domain. Their method is able to handle crossing structures that are, like the example of the superimposed sinusoids, segregated in the transform domain where the diffusion is applied. Compared to thresholding methods the combined approach gives the advantage that one can incorporate local information in the processing. For the general theory about scale spaces on Lie groups we refer to [36].

We will first briefly summarize the method of coherence enhancing diffusion on images before we show how to extend it to the domain of Gabor transforms. In order to gain computational efficiency we map, as we did in the case of reassignment, the left-invariant vector fields and induced evolutions onto phase space.

6.2 Non-Linear Anisotropic Diffusion on \mathbb{R}^2

The basic idea of coherence enhancing diffusion [114] is that one finds the solution to the scale space representation $u_f(\vec{x}, t)$ that corresponds to the evolution equation

$$\begin{cases} \partial_t u_f(\vec{x}, t) = \nabla_{\vec{x}} \cdot (C(u_f)(\vec{x}, t) \nabla_{\vec{x}} u_f)(\vec{x}, t) \\ u_f(\vec{x}, 0) = f(\vec{x}) \end{cases} \quad (6.1)$$

for a given time $t > 0$ and $\vec{x} \in \mathbb{R}^2$. Here $\nabla_{\vec{x}}$ denotes the spatial gradient operator, and $C : \mathbb{L}_2(\mathbb{R}^2 \times \mathbb{R}^+) \rightarrow C^1(\mathbb{R}^2 \times \mathbb{R}^+)$ is a function that represents the local conductivity and depends on the local structure of the solution.

Weickert proposed to use the structure tensor [10, 72, 58] to steer the

diffusion process. The structure tensor is given by

$$J_{\rho,\sigma}(u_f)(\vec{x}, t) = \left(G_\rho * \left((\nabla_{\vec{x}}(u_f(\cdot, t) * G_\sigma)) (\nabla_{\vec{x}}(u_f(\cdot, t) * G_\sigma))^T \right) \right) (\vec{x}) \quad (6.2)$$

where $G_\sigma(\vec{x}) = \frac{1}{4\pi\sigma^2} e^{-\frac{\|\vec{x}\|^2}{2\sigma^2}}$ is a normalized Gaussian kernel. The two parameters involved, σ and ρ , appear in the convolution with G_σ and the convolution with G_ρ . The first parameter, σ , ensures that the spatial gradient is less sensitive to small structures which are regarded as noise and the second parameter, ρ , reflects the scale of the structure to be measured. In practice ρ is usually larger than σ . The eigenvectors $\vec{e}_1(\vec{x}, t)$ and $\vec{e}_2(\vec{x}, t)$ that correspond to the eigenvalues $\lambda_1(\vec{x}, t) \geq \lambda_2(\vec{x}, t)$ of the structure tensor $J_{\rho,\sigma}$ point orthogonal to the local structure and along the local structure, respectively.

Now the idea is to only apply a little amount ($\epsilon > 0$) of isotropic diffusion when $\lambda_1(\vec{x}, t) \approx \lambda_2(\vec{x}, t)$ and otherwise mainly diffuse in the direction of the structure. This can be attained by setting the conductivity in eq. (6.1) as follows

$$C(u_f)(\vec{x}, t) = \epsilon I + (1 - \epsilon) e^{-\frac{c}{(\lambda_1(\vec{x}, t) - \lambda_2(\vec{x}, t))^2}} \vec{e}_2(\vec{x}, t) \vec{e}_2^T(\vec{x}, t), \quad (6.3)$$

where we used the same function as was proposed in [114] to steer the amount of diffusion in the direction that corresponds to the smallest eigenvalue of the structure tensor. Here the most sensitive parameter $c > 0$ is introduced, which can be thought of as some sort of threshold. If the local anisotropy $|\lambda_1(\vec{x}, t) - \lambda_2(\vec{x}, t)| \gg c$ there will be unit diffusion in the direction of $\vec{e}_2(\vec{x}, t)$ and only a small amount of diffusion orthogonal to that direction. If $|\lambda_1(\vec{x}, t) - \lambda_2(\vec{x}, t)| \approx 0$ there will only be a little isotropic diffusion. In the next section we will describe how the method of coherence enhancing diffusion which we applied on the additive group $(\mathbb{R}^2, +)$ can be applied to Gabor transforms.

6.3 CED on the Weyl-Heisenberg Group

Conventional coherence enhancing diffusion inhibits diffusion when there is not much structure present. In case of diffusion on the Gabor domain we still want to apply diffusion, since small structures are likely to be noise and it is beneficial to remove them. So on the Gabor domain we will

always apply a certain amount of diffusion, but when structure is present only diffusion tangent to the structure will take place while orthogonal to this structure it is inhibited. With this modification the alternative to equation (6.1) can now be formulated as

$$\begin{cases} \partial_t u_f(\vec{x}, t) &= \left(\nabla_{\vec{x}} \cdot \mathbf{S} \cdot \begin{pmatrix} 1 - (1 - \epsilon)e^{-\frac{c}{(\lambda_1 - \lambda_2)^2}} & 0 \\ 0 & 1 \end{pmatrix} \cdot \mathbf{S}^{-1} \cdot \nabla_{\vec{x}} (u_f(\cdot, t))^T \right) (\vec{x}) \\ &= (\partial_u, \partial_v) \begin{pmatrix} 1 - (1 - \epsilon)e^{-\frac{c}{(\lambda_1 - \lambda_2)^2}} & 0 \\ 0 & 1 \end{pmatrix} \begin{pmatrix} \partial_u \\ \partial_v \end{pmatrix} u_f(\vec{x}, t) \\ u_f(\vec{x}, 0) &= f(\vec{x}), \end{cases} \quad (6.4)$$

with $t > 0$, $\vec{x} \in \mathbb{R}^2$ and a matrix $\mathbf{S} = (\vec{e}_1 | \vec{e}_2)$ that maps the standard basis into the basis of the local eigenvectors \vec{e}_1 and \vec{e}_2 of the structure tensor $J_{\rho, \sigma}$. Here we introduced gauge coordinates $(\partial_u, \partial_v) = (\partial_x, \partial_y) \cdot \mathbf{S}$ that align with the eigenvalues of the structure tensor and thus with the local structure. In the next section we will discuss the alignment of the diffusion along the gauge coordinates in more detail.

6.3.1 Principal Diffusion Directions on H_r

The convection that was described in the previous chapter takes place in the direction ∂_u that is adapted to the local structure of the Gabor transform of the signal. This direction was chosen to be aligned with equi-phase lines of the Gabor transform of the signal to be reassigned. Now our goal is to design a non-linear anisotropic diffusion scheme which adapts the amount and direction of the diffusion based on the local structure in the Gabor domain. This diffusion should take place in a direction ∂_v that is orthogonal to the direction the convection would take place in. A visualization of this idea can be found in Figure 6.1. From a physical point of view there is the problem that derivatives in the frequency direction and derivatives in the spatial direction cannot be related to each other since they have different physical dimensions. Therefore we have to introduce a parameter such that this problem can be solved. In order to talk about orthogonality we introduce a metric tensor $\mathcal{G} : H_r \times \mathcal{H} \times \mathcal{H} \rightarrow \mathbb{C}$ that acts on elements of $\mathcal{H} \subset T(H_r)$, with $\mathcal{H} = \text{span}\{\partial_u, \partial_v\} = \text{span}\{\mathcal{A}_1, \mathcal{A}_2\}$ (see Figure 6.1),

$$\mathcal{G}_\beta = \beta^4 d\mathcal{A}_1 \otimes d\mathcal{A}_1 + d\mathcal{A}_2 \otimes d\mathcal{A}_2 \quad (6.5)$$

where the positive parameter β has the dimension length^{-1} . To fix the parameter β we consider the Cauchy-Riemann relations that arise when a

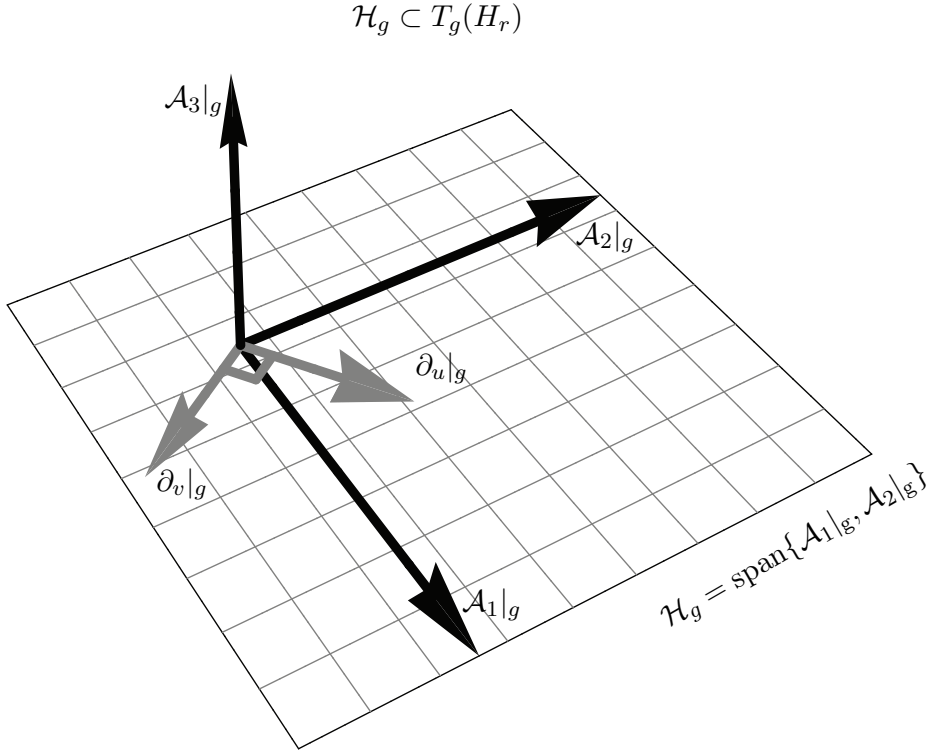


Figure 6.1: A visualization of the directions $\partial_u|_g$ and $\partial_v|_g$ in which the diffusion takes place. Convection, as described in the previous chapter takes place in the direction $\partial_u|_g$ diffusion in that direction is attenuated when structure is present at the corresponding location. The diffusion is confined to $\mathcal{H}_g = \text{span}\{\mathcal{A}_1|_g, \mathcal{A}_2|_g\}$.

specific window is chosen for the Gabor transform. Recall that this window depends on the parameter a . If we choose $\beta = \frac{1}{a}$ we have

$$\mathcal{G}_{\beta=\frac{1}{a}}^{-1}(\text{d log } |\mathbf{U}^a|, \mathbb{P}_{\mathcal{H}^*} \text{d}\Omega^a) = 0, \quad (6.6)$$

with

$$\text{d}\Omega^a = \sum_{i=1}^3 \mathcal{A}_i \Omega^a \text{d}\mathcal{A}^i, \quad (6.7)$$

and

$$\mathbb{P}_{\mathcal{H}^*} \text{d}\Omega^a = \sum_{i=1}^2 \mathcal{A}_i \Omega^a \text{d}\mathcal{A}^i. \quad (6.8)$$

Here $\mathbb{P}_{\mathcal{H}^*}$ is the orthogonal projection on the dual space \mathcal{H}^* of the horizontal part $\mathcal{H} = \text{span}\{\mathcal{A}_1, \mathcal{A}_2\}$ of the tangent space, and $U^a = |U^a|e^{i\Omega^a} = \mathcal{W}_{\psi_a}f$, cf. eq. (5.6) and eq. (5.50). Using \mathcal{G}_β with $\beta = \frac{1}{a}$ we have the geometric understanding that normal vectors $d\Omega|_{g_0}$ to equi-phase surfaces $\{g \in H_r \mid \Omega^a(g) = \Omega^a(g_0)\}$ are \mathcal{G}_β -orthogonal to the normal vectors $d|U^a| \big|_g$ of surfaces of constant amplitude $\{g \in H_r \mid |U^a(g)| = |U^a(g_0)|\}$ in the Gabor transform of a signal. These are the principal directions for which the amount of diffusion will adaptively be adjusted.

6.3.2 Non-Linear Diffusion on H_r

At this point we can express coherence enhancing diffusion on H_r where we keep the diffusion in \mathcal{H}_g , so the \mathcal{A}_3 component is kept to 0, i.e.,

$$\begin{cases} \partial_t W(x, \omega, s, t) &= \left((\beta^{-2}\mathcal{A}_1, \mathcal{A}_2) \cdot \mathbf{S} \cdot \mathbf{D} \cdot \mathbf{S}^{-1} \begin{pmatrix} \beta^{-2}\mathcal{A}_1 W \\ \mathcal{A}_2 W \end{pmatrix} \right) (x, \omega, s, t) \\ &= (\partial_u, \partial_v) \mathbf{D} \begin{pmatrix} \partial_u \\ \partial_v \end{pmatrix} W(x, \omega, s, t) \\ W(x, \omega, s, 0) &= (\mathcal{W}_{\psi_a}f)(x, \omega, s) \end{cases}, \quad (6.9)$$

with $(x, \omega, s) \in H_r$ and $t > 0$ and

$$\mathbf{D} = \begin{pmatrix} 1 - (1 - \epsilon)e^{-\frac{\epsilon}{(\lambda_1 - \lambda_2)^2}} & 0 \\ 0 & 1 \end{pmatrix}. \quad (6.10)$$

Here the normalized left-invariant vector fields on \mathbb{R}^2 , $\{\partial_x, \partial_y\}$, were replaced by the left-invariant vector fields on H_r , $\{\beta^{-2}\mathcal{A}_1, \mathcal{A}_2\}$, and the normalization $\mathcal{G}_\beta(\beta^{-2}\mathcal{A}_1, \beta^{-2}\mathcal{A}_1) = \mathcal{G}_\beta(\mathcal{A}_2, \mathcal{A}_2) = 1$ was used. The structure tensor on H_r , which we will apply to the modulus of W , now reads

$$\mathcal{J}_{\rho, \sigma}(|W|)(x, \omega, s, t) = \left(G_\rho * \begin{pmatrix} \beta^{-2}\partial_x(|W|(\cdot, s, t) * G_\sigma) \\ \partial_\omega(|W|(\cdot, s, t) * G_\sigma) \end{pmatrix} \begin{pmatrix} \beta^{-2}\partial_x(|W|(\cdot, s, t) * G_\sigma) \\ \partial_\omega(|W|(\cdot, s, t) * G_\sigma) \end{pmatrix}^T \right) (x, \omega, s, t) \quad (6.11)$$

with $G_\sigma(x, \omega) = \frac{\beta^2}{2\pi\sigma^2} e^{-\frac{\beta^4 x^2 + \omega^2}{2\sigma^2}}$. Because the left-invariant derivatives are applied to the modulus, $\mathcal{J}_{\rho, \sigma}$ is independent of s . Furthermore notice that $\mathcal{A}_1|\mathcal{W}_\psi f| = \partial_x|\mathcal{W}_\psi f|$ and $\mathcal{A}_2|\mathcal{W}_\psi f| = \partial_\omega|\mathcal{W}_\psi f|$ was used. The eigenvector that corresponds to the smallest eigenvalue of $\mathcal{J}_{\rho, \sigma}$ points in the direction

of constant amplitude, ∂_v , and the eigenvector that corresponds to the largest eigenvalue of $\mathcal{J}_{\rho,\sigma}$ points in the direction of constant phase, ∂_u . This is however only the case because of the Cauchy-Riemann equations that only hold for the initial condition. To keep this relation valid one can project W in every diffusion step such that it is again a Gabor transform of a signal.

6.3.3 Non-Linear Anisotropic Left-Invariant Diffusion on Phase-Space

Although the diffusion in eq. (6.9) only takes place in the planes $\{\text{span}\{\partial_u|_g, \partial_v|_g \mid g \in H_r\}\}$ it is still a process that takes place on the full group. To define the diffusion process on phase-space one can again apply the \mathcal{S} mapping that is described in Section 5.3.2. Thus $\tilde{\mathcal{A}}_i = \mathcal{S} \circ \mathcal{A}_i \circ \mathcal{S}$, $i = 1, 2$, $\mathcal{S} \circ \mathcal{W}_\psi f = \mathcal{G}_\psi f$ and because $|\mathcal{W}_\psi f|(\cdot, s) = |\mathcal{G}_\psi f|$ for all s we have that $\{\mathcal{S} \circ \partial_u \circ \mathcal{S}^{-1}, \mathcal{S} \circ \partial_v \circ \mathcal{S}^{-1}\} = \{\partial_{\tilde{u}}, \partial_{\tilde{v}}\}$. This gives the following diffusion equation on phase-space

$$\begin{cases} \partial_t \tilde{W}(x, \omega, t) &= \left((\beta^{-2} \tilde{\mathcal{A}}_1, \tilde{\mathcal{A}}_2) \cdot \mathbf{S} \cdot \mathbf{D} \cdot \mathbf{S}^{-1} \begin{pmatrix} \beta^{-2} \tilde{\mathcal{A}}_1 \tilde{W} \\ \tilde{\mathcal{A}}_2 \tilde{W} \end{pmatrix} \right) (x, \omega, t) \\ &= (\partial_{\tilde{u}}, \partial_{\tilde{v}}) \mathbf{D} \begin{pmatrix} \partial_{\tilde{u}} \\ \partial_{\tilde{v}} \end{pmatrix} \tilde{W}(x, \omega, t) \\ \tilde{W}(x, \omega, 0) &= (\mathcal{G}_{\psi_a} f)(x, \omega) \end{cases}, \quad (6.12)$$

for all $x, \omega \in \mathbb{R}$ and $t > 0$ and \mathbf{D} as define in eq. (6.10). If the diffusion tensor is not updated, i.e., $\mathcal{S} \circ \mathcal{J}_{\rho,\sigma}(\mathcal{S}^{-1}|\mathcal{G}_\psi f|)$ is used to obtain the eigenvalues and eigenvectors for the conductivity on phase-space, then

$$\begin{aligned} \partial_t W(x, \omega, s, t) &= (\partial_u, \partial_v) \mathbf{D} \begin{pmatrix} \partial_u \\ \partial_v \end{pmatrix} W(x, \omega, s, t) \Leftrightarrow \\ \partial_t (\mathcal{S}^{-1} \tilde{W})(x, \omega, s, t) &= (\partial_u, \partial_v) \mathbf{D} \begin{pmatrix} \partial_u \\ \partial_v \end{pmatrix} (\mathcal{S}^{-1} \tilde{W})(x, \omega, s, t) \Leftrightarrow \quad (6.13) \\ \partial_t (\mathcal{S}^{-1} \tilde{W})(x, \omega, s, t) &= (\partial_u, \partial_v) \mathcal{S}^{-1} \mathbf{D} \mathcal{S} \begin{pmatrix} \partial_u \\ \partial_v \end{pmatrix} (\mathcal{S}^{-1} \tilde{W})(x, \omega, s, t) \end{aligned}$$

for all $(x, \omega, t) \in H_r$, $t > 0$ and \mathbf{D} as defined in eq. (6.10). Now by application of \mathcal{S} on both sides we see that this implies

$$\partial_t \tilde{W}(x, \omega, t) = (\partial_{\tilde{u}}, \partial_{\tilde{v}}) \mathbf{D} \begin{pmatrix} \partial_{\tilde{u}} \\ \partial_{\tilde{v}} \end{pmatrix} \tilde{W}(x, \omega, t) \quad (6.14)$$

on phase space for $(x, \omega) \in \mathbb{R}^2$, $t > 0$ and vice versa provided that $W(\cdot, \cdot, \cdot, t)$ stays in \mathcal{H} (recall eq. (5.20)) so we can relate $\tilde{W}(x, \omega, t)$ to $W(x, \omega, s, t)$ via \mathcal{S} . This is the case since $\mathcal{W}(\cdot, \cdot, \cdot, 0) \in \mathcal{H}$ and the operator in the diffusion equation is a composition of $\mathcal{A}_i : \mathcal{H} \rightarrow \mathcal{H}$, with $i = 1, 2$, and multiplication operators $M : \mathcal{H} \rightarrow \mathcal{H}$ of the form

$$(MF)(x, \omega, s) = M(x, \omega)F(x, \omega, s) . \quad (6.15)$$

We furthermore notice that the eigenvalues and corresponding eigenvectors of the structure tensor on H_r , $\mathcal{J}_{\rho, \sigma}(|\mathcal{W}_\psi f|)$, are equivalent to the ones of the structure tensor on phase space, $\mathcal{S} \circ \mathcal{J}_{\rho, \sigma}(\mathcal{S}^{-1}|\mathcal{G}_\psi f|)$. Now by the uniqueness of the solutions W of eq. (6.9) and \tilde{W} of eq. (6.12), which are unique because of the choice that the conductivity solely depends on the initial condition, we have

$$\begin{aligned} \tilde{W}(\cdot, \cdot, 0) &= \mathcal{G}_\psi f = \mathcal{S} \circ \mathcal{W}_\psi f = \mathcal{S} \circ W(\cdot, \cdot, \cdot, 0) \\ &\Rightarrow \forall_{t \geq 0} : \tilde{W}(\cdot, \cdot, t) = \mathcal{S} \circ W(\cdot, \cdot, \cdot, t) . \end{aligned} \quad (6.16)$$

So one might as well obtain the solution to eq. (6.9) for a given time t by calculating $\mathcal{S}^{-1} \circ \tilde{W}(\cdot, t)$, which is a $2D$ problem instead of a $3D$ one.

6.4 Evaluation

We implemented the diffusion process using a basic Euler-forward method in the time direction and discrete left-invariant central differences in the space and frequency direction. The discrete group and the corresponding discrete left-invariant derivatives are described in Section 5.6.

To evaluate the diffusion method we apply the nonlinear diffusion method to the Gabor transforms of the signals that are shown in Figure 6.2. To obtain the noisy signals we added zero-mean white Gaussian noise with a variance that is a quarter of the maximum signal amplitude to both the complex and real parts of the signals. The noisy signals are depicted in

Figure 6.3. We used the numerically optimized window ψ_a^d that is given in Section 5.6.3 to compute the Gabor transforms of the signals using window scale $a = \frac{1}{6}$ so $\beta = 6$, grid constants $K = M = N = 128$, which implies $L = 1, P = 128$. The parameters for the diffusion process are, the time step in the Euler-forward method $\tau = 0.1$, total diffusion time $t = 30$, regularization scales $\rho = 2, \sigma = 0.25$ and parameters for the nonlinear penalization function $\epsilon = 10^{-4}, c = \log 1.01$. Clearly the noise is removed from the signal, also enhancement can be observed since the top most signal in Figure 6.4 has a slightly larger support in time compared to the reference signal that is displayed in Figure 6.2

6.5 Conclusions

We showed that it is possible to enhance signals by means of nonlinear anisotropic left-invariant diffusion on the domain of Gabor transforms. In order to gain computational efficiency we map the left-invariant vector fields, which guarantee translation and modulation covariance, and the induced evolutions on phase space. This reduces the complexity by one dimension while retaining the non-commutative structure on the Heisenberg group. The theory we derived in the continuous domain is mapped to the discrete domain by replacing the continuous group by a discrete group yielding discrete left-invariant vector fields that allow for an exact implementation on the grid.

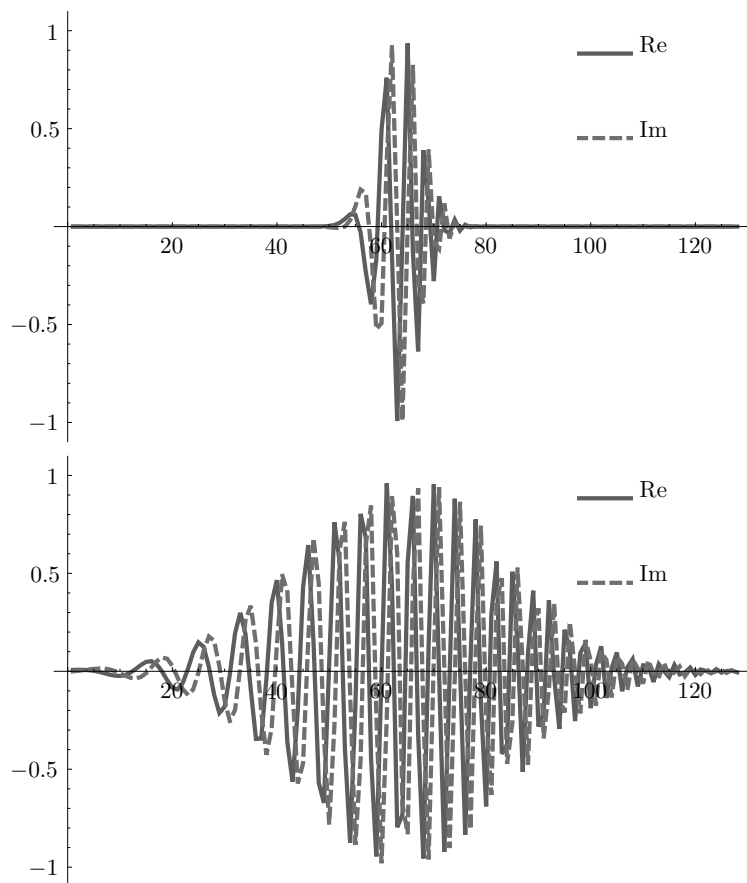


Figure 6.2: The reference signals to which noise is added. Top most a signal with a small support is shown. On the bottom a visualization of a chirp whose amplitude is modulated by a Gaussian is depicted.

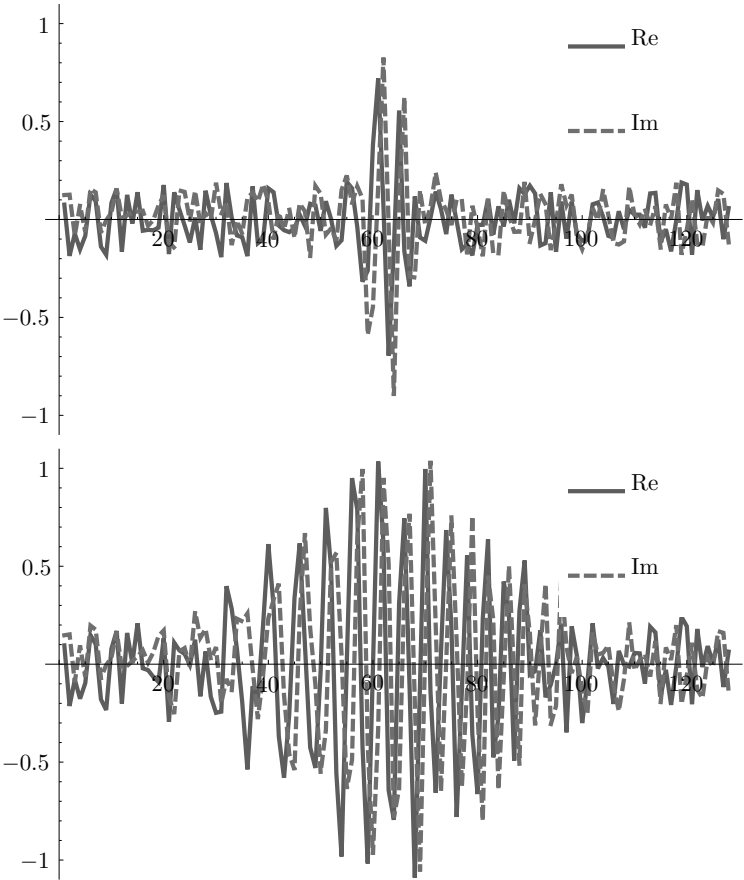


Figure 6.3: Noisy versions of the signals in Figure 6.2.

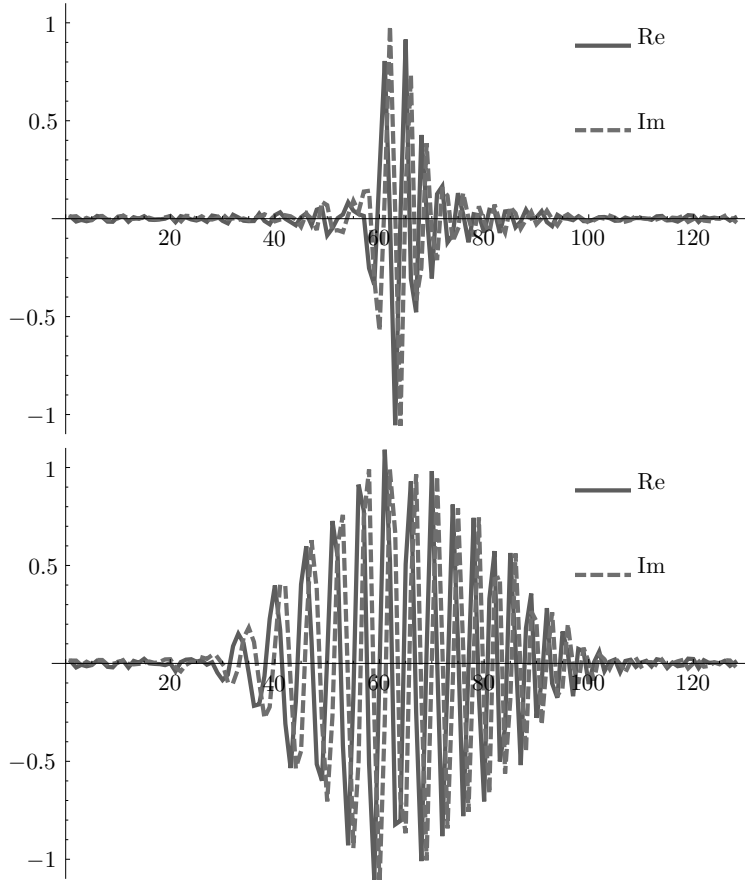


Figure 6.4: Enhanced versions of the signals that are depicted in Figure 6.3. Parameters involved are window scale $a = \frac{1}{6}$, grid constants $K = M = N = 128$, timestep $\tau = 0.1$, diffusion time $t = 30$, regularization parameters $\rho = 2$, $\sigma = 0.25$ and parameters for the nonlinear penalization function $\epsilon = 10^{-4}$ and $c = \log 1.01$. These parameter settings imply that $P = 128$, $L = 1$ and $\beta = 6$.

7

Summary and Future Research

7.1 Representation and Manipulation of Images Based on Linear Functionals (Summary)

The reconstruction of a signal from its samples is one of the fundamental problems in signal processing. It deserves and receives much attention from the scientific community. In this thesis we consider a general case of the sampling problem. We aim to reconstruct an image from a set of samples that are irregularly spaced and obtained by means of linear functionals on the image. As an application we reconstruct a candidate image from differential structure that is obtained from a scale space representation of an image at the locations of certain interest points. The locations of these points are not arbitrary, but induced by the structure of the image.

In addition to the reconstruction of images we describe the enhancement of time-frequency representations. Both the time-frequency representation of the signal and the signal itself are enhanced. The enhancements are achieved by applying a convection process and a diffusion process to the Gabor transform of the signal, respectively. These evolution processes should be translation and modulation covariant on the signal domain. To achieve this the corresponding operator on the time-frequency domain must be left-invariant. This means that the operator should commute with the left-regular representation of the Heisenberg group. This part is a specialization of a more general theory on scale spaces on Lie groups.

Chapter 2 presents a linear reconstruction method that searches for an image that is indistinguishable from its original when observed through the filters the features were extracted with, and simultaneously minimizes a certain prior. This prior should be a norm that is induced by an inner product. We show that by using a Sobolev norm visually appealing reconstructions can be obtained by means of orthogonal projections in the corresponding Sobolev space. In this chapter the domain of definition of an image is taken to be all of \mathbb{R}^n , i.e. boundary conditions are de-emphasized.

A similar method to the one that is presented in Chapter 2 is described in Chapter 3. There we formulate the reconstruction problem for the bounded domain. This overcomes problems that appear on the unbounded domain when much regularization is used. The implementation of the method is done in the discrete domain and is exact on the grid such that approximation and truncation errors are avoided.

In Chapter 4 the reconstruction problem is casted into an approximation problem. Features are not interpolated as in the previous two chapters but are rather approximated. The approximation framework admits a coarse-to-fine reconstruction method that uses a gauge field to propagate information from reconstructions at a coarse resolution to a reconstruction at a finer level of resolution. To allow for a gauge field an image is not interpreted as a scalar function, but as a section through a so-called fibred space.

Enhancement of time-frequency representations of signals, which is also called reassignment, is discussed in Chapter 5. We show that Gabor transforms of signals can be considered as functions on the Weyl-Heisenberg group. In order to define operators on the domain of Gabor transforms that are translation and modulation covariant on the signal domain we construct left-invariant vector fields. Using these vector fields we define an adaptive convection process on Gabor transforms that are phase-invariant. This leads to a time-frequency representation of the signal that is easier to interpret. In order to discretize the method we identify a discrete group for which we obtain the discrete left-invariant vector fields. This discretization ensures that the method is confined to the given discrete grid, thus avoiding interpolation.

In Chapter 6 we apply the theory that was developed in Chapter 5 to the construction of left-invariant nonlinear anisotropic diffusion processes on Gabor transforms. As a result an enhancement of the signal is obtained. Our method can be beneficial compared to thresholding methods since it is able to take local information into account. Nonlinear diffusion schemes on the signal domain do have this advantage, but lack the ability to separate time-frequency structures.

7.2 Future Research

In this section we will give a short and non-exhaustive list of possible areas of future research. An interesting open research problem is the adaptation of the methods that are presented in Chapter 2 and Chapter 3 for the interpolation of vector or tensor fields. Furthermore the application of gauge fields to image sequence analysis should be considered.

The reconstructions from features obtained at the locations of singular points of Gaussian scale space representations of images contain spurious singular points, i.e. singular points appear in the scale space representation of the reconstructed image that were not present in the scale space representation of the original image. It would be interesting if one could devise a reconstruction method that guarantees that no new singular points are introduced in the scale space representation of the reconstructed image. Possible directions are the introduction of different features. Another possibility could be the adaptation of the method that is presented in Chapter 4. Here a feedback loop could be introduced such that unwanted singularities can be (iteratively) suppressed. An adaptation of the coarse-to-fine reconstruction method such that nonlinear partial differential equations (PDE's) are used for regularization is feasible. A longer-term research goal could be video and image compression based on singular points although it will be very hard to compete with state of the art compression schemes.

Reassignment via left-invariant vector fields does not provide a perfect representation of the signal. Elimination of the errors that are introduced by the reassignment method should thus be subject of further research. One of the first things to address would be phase-covariant reassignment that does not leave the phase untouched for every time-frequency location. With respect to the diffusion processes, audio applications should be considered. The diffusion process still depends on many parameters and is dependent on the diffusion time itself. Automatic determination of these parameters would be of great interest. One can also think of combining the convection and diffusion process. Furthermore the adaptation of the method to enhance images can be considered. The presented theory is also applicable to other groups such as the affine group, which is related to the wavelet transform.



Appendix to Chapter 2

A.1 Simple Alternative Approach to Theorem 2.2.2

Recall that V is the span of the filters κ_i . Then

$$V^\perp = \{f \in \mathbb{L}_2(\mathbb{R}^2) \mid (\kappa_i, f)_A = 0 \ \forall \ i = 1, \dots, N\} \quad (\text{A.1})$$

On the space of images $\mathbb{L}_2(\mathbb{R}^2)$ we define the following equivalence relation:

$$f \sim g \Leftrightarrow (\kappa_i, f)_A = (\kappa_i, g)_A \ \forall \ i = 1, \dots, N, \quad (\text{A.2})$$

i.e. two images are equivalent if they share the same set of features. As a result the equivalence class $[f]$ of representant f is given by

$$[f] = \{g \in \mathbb{L}_2(\mathbb{R}^2) \mid f \sim g\} = f + V^\perp. \quad (\text{A.3})$$

Next we show that the unique element g within $[f]$ that minimizes the energy $E[g] = \|g\|_A^2$ is given by the A -orthogonal projection of f on V , $\mathcal{P}_V f$:

$$\min_{g \in [f]} \|g\|_A^2 = \min_{g \in [f]} \|g - \mathcal{P}_V f + \mathcal{P}_V f\|_A^2 = \min_{g \in [f]} \|g - \mathcal{P}_V f\|_A^2 + \|\mathcal{P}_V f\|_A^2 \quad (\text{A.4})$$

and this equals $\|\mathcal{P}_V f\|_A^2$ only in the case $g = \mathcal{P}_V f$. Notice with respect to the last equality (equation (A.4)) the Pythagoras theorem has been used, which can be applied since $(g - \mathcal{P}_V f) = (g - \mathcal{P}_V g) \in V^\perp$ and $\mathcal{P}_V f \in V$.

B

Appendix to Chapter 3

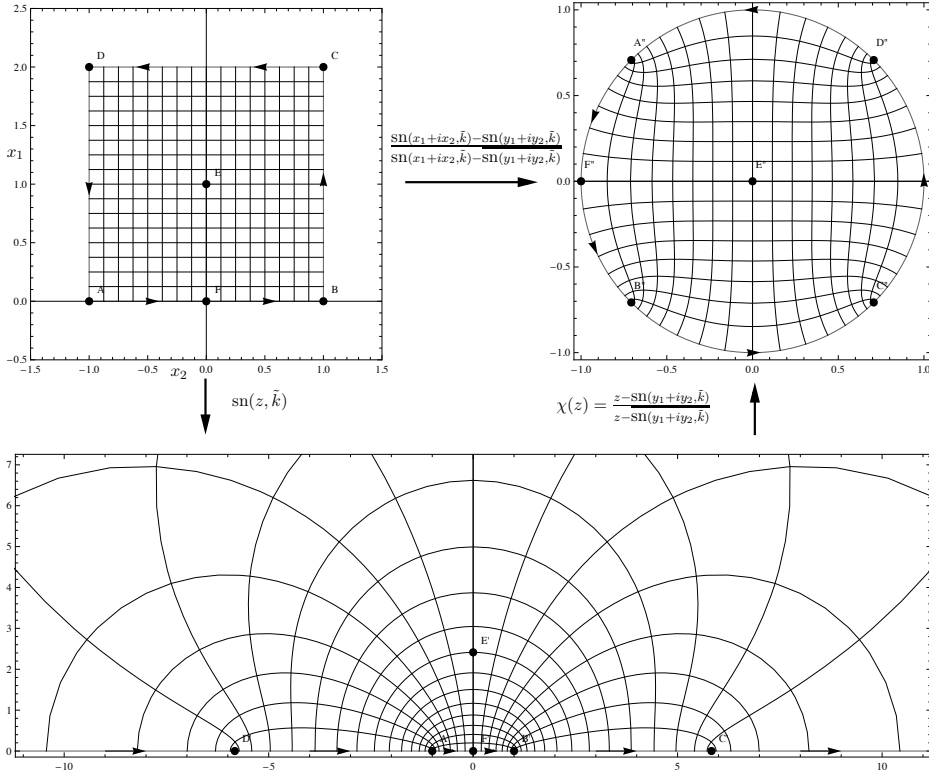


Figure B.1: Mapping from a square (top left) to the upper half space in the complex plane (bottom) followed by a mapping to the disc (upper right). The concatenation of the two mappings (from top left to top right) is used to obtain the Green's function of the Dirichlet operator. In this particular example $a = 1, b = 2$, and $(y_1, y_2) = (0, 1)$.

B.1 Green's Function of the Dirichlet Operator on a Rectangle

The Green's function $G : \Omega \times \Omega \rightarrow \mathbb{R}$ of the Dirichlet operator \mathcal{D} (recall Definition 5) can be obtained by means of conformal mapping¹. A visualization of the mappings used to arrive at the solution can be found in Fig. B.1.

To this end we first map the rectangle to the upper half space in the

¹Our solution is a generalization of the solution derived by Boersma et al. in [13].

complex plane. By the Schwarz-Christoffel formula the derivative of the inverse of such a mapping is given by

$$\begin{aligned}\frac{dz}{dw} &= -C \frac{1}{\tilde{k}} (w-1)^{-\frac{1}{2}} (w+1)^{-\frac{1}{2}} \left(w - \frac{1}{\tilde{k}}\right)^{-\frac{1}{2}} \left(w + \frac{1}{\tilde{k}}\right)^{-\frac{1}{2}} \\ &= C \frac{1}{\sqrt{1-w^2}} \frac{1}{\sqrt{1-\tilde{k}^2 w^2}},\end{aligned}\quad (\text{B.1})$$

where $C \in \mathbb{R}^+$ and $w(\pm 1/\tilde{k}) = \pm a + ib$. As a result

$$z(w, \tilde{k}) = C \int_0^w \frac{dt}{\sqrt{1-t^2} \sqrt{1-\tilde{k}^2 t^2}} \Leftrightarrow w(z) = \text{sn}\left(\frac{z}{C}, \tilde{k}\right), \quad (\text{B.2})$$

where sn denotes the Jacobi-elliptic function [52], [117, Chapter XXII]. We have $\text{sn}(0, \tilde{k}) = 0$, $\text{sn}(\pm a, \tilde{k}) = \pm 1$, $\text{sn}(\pm a + ib, \tilde{k}) = \pm(1/\tilde{k})$ and $\text{sn}(i(b/2), \tilde{k}) = i/\sqrt{\tilde{k}}$, where the elliptic modulus \tilde{k} is given by

$$(b/a)z(1, \tilde{k}) = z(1, \sqrt{1-\tilde{k}^2}). \quad (\text{B.3})$$

We note that for every fraction $b/a \in \mathbb{R}^+$ there is a unique \tilde{k} that satisfies eq. (B.3). For example, in case of a square $b/a = 2$ we have $\tilde{k} \approx 0.1715728752$. The reader must be aware that \tilde{k} is a function of the aspect ratio b/a .

For the moment we assume

$$a = z(1, \tilde{k}) \quad (\text{B.4})$$

and

$$b = z(1, \sqrt{1-\tilde{k}^2}), \quad (\text{B.5})$$

which implies $C = 1$. The next step is to map the half plane onto the unit disk $\overline{B_{\mathbf{0},1}} = \{\mathbf{x} \in \mathbb{R}^2 \mid \|\mathbf{x}\| \leq 1\}$. This is easily done by means of a linear fractional transform

$$\chi(z) = \frac{z - \text{sn}(y_1 + i y_2, \tilde{k})}{z - \text{sn}(y_1 + i y_2, \tilde{k})}. \quad (\text{B.6})$$

To this end we notice that $|\chi(0)| = 1$ and that the mirrored points $\text{sn}(y_1 + i y_2, \tilde{k})$ and $\text{sn}(y_1 + i y_2, \tilde{k})$ are mapped to the mirrored points $\chi(\text{sn}(y_1 + i y_2, \tilde{k})) = 0$ and $\chi(\overline{\text{sn}(y_1 + i y_2, \tilde{k})}) = \infty$.

Now define $F : \mathbb{C} \rightarrow \mathbb{C}$ and $\mathbf{F} : \bar{\Omega} \rightarrow \overline{B_{\mathbf{0},1}}$ by

$$\begin{aligned} F &= \chi \circ \text{sn}(\cdot, \tilde{k}), \text{ i.e. } F(x_1 + i x_2) = \frac{\text{sn}(x_1 + i x_2, \tilde{k}) - \text{sn}(y_1 + i y_2, \tilde{k})}{\text{sn}(x_1 + i x_2, \tilde{k}) - \text{sn}(y_1 + i y_2, \tilde{k})} \\ \mathbf{F}(x_1, x_2) &= (\text{Re}(F(x_1 + i x_2)), \text{Im}(F(x_1 + i x_2)))^T, \end{aligned} \quad (\text{B.7})$$

then \mathbf{F} is a conformal mapping of $\bar{\Omega}$ onto $\overline{B_{\mathbf{0},1}}$ with $\mathbf{F}(\mathbf{y}) = \mathbf{0}$. As a result we have by the Cauchy-Riemann equations

$$\Delta_{\mathbf{F}(\mathbf{x})} = |\mathbf{F}'(\mathbf{x})|^{-1} \Delta_{\mathbf{x}}, \quad (\text{B.8})$$

where the scalar factor in front of the right Laplacian is the inverse Jacobian:

$$\begin{aligned} |\mathbf{F}'(\mathbf{x})|^{-1} &= (\det \mathbf{F}'(\mathbf{x}))^{-1} \\ &= \left(\left(\frac{\partial F_1}{\partial x_1}(\mathbf{x}) \right)^2 + \left(\frac{\partial F_2}{\partial x_1}(\mathbf{x}) \right)^2 \right)^{-1} \\ &= |F'(x_1 + i x_2)|^{-1}, \end{aligned} \quad (\text{B.9})$$

for all $\mathbf{x} = (x_1, x_2) \in \Omega$.

Now $\tilde{G}(\mathbf{u}, \mathbf{0}) = \frac{-1}{2\pi} \log \|\mathbf{u}\|$ is the unique Green's function with Dirichlet boundary conditions on the disk $\overline{B_{\mathbf{0},1}}$ with singularity at $\mathbf{0}$ and our Green's function is given by $\check{G} = \tilde{G} \circ \mathbf{F}$, i.e.

$$\begin{aligned} \check{G}(\mathbf{x}, \mathbf{y}) &= -\frac{1}{2\pi} \log |(\chi \circ \text{sn}(\cdot, \tilde{k}))(x_1 + i x_2)| \\ &= -\frac{1}{2\pi} \log \left| \frac{\text{sn}(x_1 + i x_2, \tilde{k}) - \text{sn}(y_1 + i y_2, \tilde{k})}{\text{sn}(x_1 + i x_2, \tilde{k}) - \text{sn}(y_1 + i y_2, \tilde{k})} \right|. \end{aligned} \quad (\text{B.10})$$

In eqs. (B.4) and (B.5) we assumed a certain scaling of a and b such that $C = 1$. To obtain the Green's function for the correctly scaled domain we can simply apply an isotropic scaling to the Green's function found in eq. (B.10). Hence we obtain for the Green's function $G_{a,b} : \Omega \times \Omega \rightarrow \mathbb{R}$ of the Dirichlet operator \mathcal{D} ,

$$G_{a,b}(\mathbf{x}, \mathbf{y}) = \quad (\text{B.11})$$

$$-\frac{1}{2\pi} \log \left| \frac{\text{sn}(x_1 \frac{z(1, \tilde{k})}{a} + i x_2 \frac{z(1, \sqrt{1-\tilde{k}^2})}{b}, \tilde{k}) - \text{sn}(y_1 \frac{z(1, \tilde{k})}{a} + i y_2 \frac{z(1, \sqrt{1-\tilde{k}^2})}{b}, \tilde{k})}{\text{sn}(x_1 \frac{z(1, \tilde{k})}{a} + i x_2 \frac{z(1, \sqrt{1-\tilde{k}^2})}{b}, \tilde{k}) - \text{sn}(y_1 \frac{z(1, \tilde{k})}{a} + i y_2 \frac{z(1, \sqrt{1-\tilde{k}^2})}{b}, \tilde{k})} \right|. \quad (\text{B.12})$$

Here we applied the following mappings: $x_1 \mapsto \frac{x_1 \operatorname{sn}(1, \tilde{k})}{a}$, $x_2 \mapsto \frac{x_2 \operatorname{sn}(1, \sqrt{1-\tilde{k}^2})}{b}$, $y_1 \mapsto \frac{y_1 \operatorname{sn}(1, \tilde{k})}{a}$, and $y_2 \mapsto \frac{y_2 \operatorname{sn}(1, \sqrt{1-\tilde{k}^2})}{b}$. This is an isotropic scaling because of eq. (B.3).

B.2 The Green's Function on the Unbounded Domain as a Limit of the Dirichlet Kernel

Next we shall put a relation between the fundamental solution of the Laplace operator on the unbounded domain and the Green's function on the bounded domain with Dirichlet conditions (i.e. the impuls response of the Dirichlet operator) on the square, i.e. $b = 2a$. Here we shall rewrite the solution eq. (B.11) for $b = 2a$ as follows

$$G_{a,b=2a}(\mathbf{x}, \mathbf{y}) = -\frac{1}{2\pi} \log |\phi(\beta z) - \phi(\beta v)| + \frac{1}{2\pi} \log |\phi(\beta z) - \phi(\overline{\beta v})|, \quad (\text{B.13})$$

where $z = x_1 + ix_2$ and $v = y_1 + iy_2$ and $\phi(\beta z) = \operatorname{sn}\left(\frac{z(1, \tilde{k})}{a}(x_1 + ix_2), \tilde{k}\right)$, $\beta = \frac{z(1, \tilde{k})}{a} > 0$. We recall that \tilde{k} is the unique solution of eq. (B.3) with $b = 2a$. Furthermore, we note that $\phi(\bar{v}) = \overline{\phi(v)}$ for all $v \in \mathbb{C}$.

By taking the limit $a \rightarrow \infty$ and $b = 2a \rightarrow \infty$ in the rectangular case we arrive at the Dirichlet problem on the upper plane $\{(x_1, x_2) \in \mathbb{R}^2 \mid x_2 > 0\}$. It is well-known, see eg. [75], that the solution of this problem is given by a superposition of two fundamental solutions (the Green's function of the Laplace operator on \mathbb{R}^2). In this case one fundamental solution is centered with plus sign at (y_1, y_2) and one fundamental solution is centered at $(y_1, -y_2)$ with negative sign. This is based on the well-known Schwarz principle and the fact that the difference of these fundamental solutions is zero at the boundary so that the Dirichlet condition is satisfied. In the field of electro-magnetics this result is obvious since the electric potential due to a negative charge at (y_1, y_2) cancels out to the electric potential due to a positive charge at $(y_1, -y_2)$. From this observation we should get

$$\lim_{a \rightarrow \infty} G_{a,b=2a}(\mathbf{x}, \mathbf{y}) = -\frac{1}{2\pi} \log |z - v| + \frac{1}{2\pi} \log |z - \bar{v}|, \quad (\text{B.14})$$

which we shall verify next.

The mapping $\phi : [-a, a] + i[0, b] \rightarrow \mathbb{C}$ is analytic and by means of the mean-value theorem there exist $\xi_{z,\beta}^1 \in B_{\beta v, \beta|z-v|} = \{w \in \mathbb{C} \mid |w - \beta v| < \beta|z - v|\}$, $\xi_{z,\beta}^2 \in B_{\overline{\beta v}, \beta|z-\bar{v}|}$. Therefore we have

$$\phi(z) = \phi(w) + \phi'(\xi_z^1) (z - w) \text{ and } \phi(z) = \phi(\bar{w}) + \phi'(\xi_z^2) (z - \bar{w}) \quad (\text{B.15})$$

so that we have

$$\lim_{a \rightarrow \infty} G_{a,b=2a}(\mathbf{x}, \mathbf{y}) = -\frac{1}{2\pi} \left(\log \left| \frac{\phi'(\xi_z^1)}{\phi'(\xi_z^2)} \right| + \log |z - v| - \log |z - \bar{v}| \right), \quad (\text{B.16})$$

where we recall that $\beta = \left(\frac{z(1, \tilde{k})}{a} \right)$. As $a \rightarrow \infty$, i.e. $\beta \rightarrow 0$, it follows by the continuity of $z \mapsto \phi'(z)$ that $\log \left| \frac{\phi'(\xi_z^1)}{\phi'(\xi_z^2)} \right| \rightarrow \log 1 = 0$, from which the result in eq. (B.14) follows.



Appendix to Chapter 5

C.1 Diagonalization of the Gabor Frame Operator

In our implementation we used fast algorithms for the discrete Gabor transform as well as for the calculation of the synthesis windows. The tool for such fast algorithms is the Zak transform [123] which was introduced in the signal processing community by A.J.E.M. Janssen [59, 61], cite[Chapter 1]Feichtinger1998 and [60] as referred to in e.g. [14]. There exists a vast literature on the subject of fast transforms. Methods based on IIR filters are proposed [9], as well as methods using the discrete Zak transform [59, 4]. Zak transform based methods are proposed for rational oversampling [8] and even for Gabor transforms on non-separable time-frequency grids [111]. For a good review on the discrete Zak transform and its application to discrete cyclic Gabor transforms we refer to [14] and the references therein.

In a similar manner to eq. (5.73) the discrete Gabor transform can be written by means of a discrete inner product

$$\left(\mathcal{G}_{\vec{\psi}}^D \vec{f}\right)[l, m] = \left(\mathcal{U}^D[l, m, k = -\frac{lmQ}{2P}] \vec{\psi}, \vec{f}\right)_{l_2(I)}, \quad (\text{C.1})$$

with $l = 0, \dots, K-1$, and $m = 0, \dots, M-1$. We abbreviate the vectors $\mathcal{U}^D[l, m, k = -\frac{lmQ}{2P}] \vec{\psi}$ as $\vec{\psi}_{lm}$. If the inner products of the elements of the set $\{\vec{\psi}_{lm}\}_{l=0, m=0}^{l=K-1, m=M-1}$ with any band limited signal \vec{f} completely describe that signal it is called a frame [34]. Clearly this depends on K and M and the window $\vec{\psi}$. For the case of the discrete Gabor transform necessary conditions for these parameters are given by Daubechies in [27]. A short exposition of frame theory can be found in [83, Chapter 5].

Next we consider the frame operator $\mathfrak{F} : l_2(I) \rightarrow l_2(I)$,

$$\left(\mathfrak{F} \vec{f}\right)[n] = \sum_{l=0}^{K-1} \sum_{m=0}^{M-1} \left(\vec{\psi}_{lm}, \vec{f}\right)_{l_2(I)} \vec{\psi}_{lm}[n] \quad (\text{C.2})$$

with $n \in I$. If $\{\vec{\psi}_{lm}\}_{l=0, m=0}^{l=K-1, m=M-1}$ constitutes a frame there exist Riesz-bounds $A, B > 0$ such that

$$A \|\vec{f}\|_{l_2(I)} \leq \sum_{l=0}^{K-1} \sum_{m=0}^{M-1} \left| \left(\mathfrak{F} \vec{f}, \vec{f}\right)_{l_2(I)} \right|^2 \leq B \|\vec{f}\|_{l_2(I)} \quad (\text{C.3})$$

so \mathfrak{F} is bounded and \mathfrak{F}^{-1} exists. Because of linearity of the inner product we have $\mathfrak{F}^* = \mathfrak{F}$ and

$$f = \mathfrak{F}^{-1} \mathfrak{F} f = \sum_{l=0}^{K-1} \sum_{m=0}^{M-1} \left(\vec{\psi}_{lm}, \vec{f} \right)_{l_2(I)} \mathfrak{F}^{-1} \vec{\psi}_{lm}, \quad (\text{C.4})$$

so the synthesis window $\mathfrak{F}^{-1} \vec{\psi}_{lm}$ can be obtained from the analysis window $\vec{\psi}_{lm}$ by applying the inverse of the frame operator. Since \mathfrak{F} is self-adjoint on a finite dimensional vector space it has an orthonormal basis of eigen vectors. The discrete Zak-transform is an expansion into this orthonormal basis (see e.g. [14]) and is given by

$$\left(Z^D \vec{f} \right) [n, k] = \left(\vec{u}_{nk}, \vec{f} \right)_{l_2(I)} \quad (\text{C.5})$$

with

$$\vec{u}_{nk}[n'] = \frac{1}{\sqrt{K}} \vec{v}[n' - n] e^{\frac{2\pi i k}{N}(n' - n)}, \quad (\text{C.6})$$

$\vec{v}[n] = \sum_{l=-\infty}^{\infty} \delta[n - lL]$, $n \in \{0, \dots, L-1\}$ and $k \in \{0, \dots, K-1\}$. We recall that $N = KL$. Using this decomposition the frame operator can be expressed in diagonal form

$$\mathfrak{F} = \left(Z^D \right)^{-1} \circ \Lambda \circ Z^D \quad (\text{C.7})$$

with a diagonal matrix Λ that contains the eigen values

$$\lambda_{nk} = L \sum_{p=0}^{P-1} \left| \left(Z^D \vec{\psi} \right) \left[n, k - p \frac{N}{M} \right] \right|^2 \quad (\text{C.8})$$

and where the oversampling factor $P = M/L$ is integer valued. Using this decomposition the synthesis window is obtained by

$$\mathfrak{F}^{-1} \vec{\psi} = \sum_{n=0}^{L-1} \sum_{k=0}^{K-1} \lambda_{nk}^{-1} \left(\vec{u}_{nk}, \vec{\psi} \right)_{l_2(I)} \vec{u}_{nk}. \quad (\text{C.9})$$

We also note that the Zak transform can be implemented efficiently by means of fast Fourier transforms.

Bibliography

- [1] M. Arigovindan. *Variational Reconstruction of Vector and Scalar Images from Non-Uniform Samples*. PhD thesis, Ecole Polytechnique Fédérale de Lausanne, Lausanne, Switzerland, 2005.
- [2] M. Arigovindan, M. Sühling, P. Hunziker, and M. Unser. Variational image reconstruction from arbitrarily spaced samples: A fast multiresolution spline solution. *IEEE Transactions on Image Processing*, 14(4):450–460, April 2005.
- [3] F. Auger and P. Flandrin. Improving the readability of time-frequency and time-scalerepresentations by the reassignment method. *IEEE Transactions on Signal Processing*, 43(5):1068–1089, May 1995.
- [4] L. Auslander, I.C. Gertner, and R. Tolimieri. The discrete Zak transform application to time-frequency analysis and synthesis of nonstationary signals. *IEEE Transactions on Signal Processing*, 39(4):825–835, April 1991.
- [5] A. Averbuch, M. Israeli, and L. Vozovoi. A fast Poisson solver of arbitrary order accuracy in rectangular regions. *SIAM Journal of Scientific Computing*, 19(3):933–952, May 1998.
- [6] E. Balmashnova. *Scale-Euclidean invariant object retrieval*. PhD thesis, Eindhoven University of Technology, Eindhoven, The Netherlands, 2007.
- [7] R. Barret, M. Berry, T.F. Chan, and et al. *Templates for the solution of linear systems: Building blocks for iterative methods*. Society for Industrial and Applied Mathematics, 1994.
- [8] M.J. Bastiaans and M.C.W. Geilen. On the discrete Gabor transform and the discrete Zak transform. *Signal Processing*, 49(3):151–166, 1996.
- [9] A. Bernardino and J. Santos-Victor. Fast IIR isotropic 2-D complex Gabor filters with boundary initialization. *IEEE Transactions on Image Processing*, 15(11):3338–3349, November 2006.
- [10] J. Bigün and G.H. Granlund. Optimal orientation detection of linear symmetry. In *Proceedings of the ICCV*, pages 433–438, 1987.

- [11] J. Blom. *Topological and Geometrical Aspects of Image Structure*. PhD thesis, University of Utrecht, Utrecht, The Netherlands, 1992.
- [12] T. Blu and M. Unser. Quantitative Fourier analysis of approximation techniques: Part I: Interpolators and projectors. *IEEE Transactions on Signal Processing*, 47(10):2783–2795, October 1999.
- [13] J. Boersma, J.K.M. Jansen, F.H. Simons, and F.W. Sleutel. The SIAM 100-dollar, 100-digit challenge: Problem 10. SIAM News, January 2002. <http://www.win.tue.nl/casa/meetings/special/siamcontest/problem10.pdf>.
- [14] H. Bölcskei and F. Hlawatsch. Discrete Zak transforms, polyphase transforms, and applications. *IEEE Transactions on Signal Processing*, 45(4):851–866, April 1997.
- [15] W.L. Briggs, V.E. Henson, and S.F. McCormick. *A Multigrid Tutorial*. Society for Industrial and Applied Mathematics, 2000.
- [16] M. Brueß and J. Weickert. A shock-capturing algorithm for the differential equations of dilation and erosion. *Journal of Mathematical Imaging and Vision*, 25(2):187–201, 2006.
- [17] B. Burgeth and J. Weickert. An explanation for the logarithmic connection between linear and morphological systems. In *Scale Space Methods in Computer Vision, 4th International Conference, Scale Space 2003*, Lecture Notes in Computer Science, pages 325–339, Berlin, 2003. Springer Verlag.
- [18] B. Burgeth and J. Weickert. An explanation of the logarithmic connection between linear and morphological system theory. *International Journal of Computer Vision*, 64(2/3):157–169, September 2005.
- [19] S. Butterworth. On the theory of filter amplifiers. *Wireless Engineer*, 7:536–541, 1930.
- [20] J.E. Candes, J. Romberg, and T. Tao. Robust uncertainty principles: Exact signal reconstruction from highly incomplete frequency information. *IEEE Transactions on Information Theory*, 52(2):489–509, February 2006.

- [21] O. Cappeé. Elimination of the musical noise phenomenon with the Ephraim and Mallah noise suppressor. *IEEE Transactions on Speech and Audio Processing*, 2(2):345–349, April 1994.
- [22] E. Chassande-Mottin. *Méthodes de réallocation dans le plan temps-fréquence pour l'analyse et le traitement de signaux non stationnaires*. PhD thesis, Université de Cergy-Pontoise, France, 1998.
- [23] E. Chassande-Mottin, I. Daubechies, F. Auger, and P. Flandrin. Differential reassignment. *Signal Processing Letters, IEEE*, 4(10):293–294, October 1997.
- [24] P. Christian Hansen, J.G. Nagy, and D.P. O’Leary. *Deblurring Images*. Fundamentals of Algorithms. Society for Industrial and Applied Mathematics, 2006.
- [25] G.H. Cottet and L. Germain. Image processing through reaction combined with nonlinear diffusion. *Mathematics of Computation*, 61(204):659–673, October 1993.
- [26] J. Damon. Local Morse theory for solutions to the heat equation and Gaussian blurring. *Journal of Differential Equations*, 115(2):368–401, January 1995.
- [27] I. Daubechies. *Ten Lectures on Wavelets*, volume 61. CBMS-NSF Regional Conference Series in Applied Mathematics, 8 edition, 1992.
- [28] I. Daubechies and S. Maes. A nonlinear squeezing of the continuous wavelet transform based on auditory nerve models. In A. Aldroubi and M. Unser, editors, *Wavelets in Medicine and Biology*, pages 527–546. CRC Press, 1996.
- [29] L. Daudet, M. Morvidone, and B. Torrèsani. Time-frequency and time-scale vector fields for deforming time-frequency and time-scale representations. In M. Unser, editor, *Proceedings of the SPIE conference, Denver*, pages 2–15, 1999.
- [30] N.G. de Bruijn. Uncertainty principles in Fourier analysis. In Oved Shisha, editor, *Inequalities: proceedings of a symposium held at Wright-Patterson air force base, Ohio*, pages 57–71, New York, August 1967. Academic Press.

- [31] N.G. de Bruijn. A theory of generalized functions, with applications to Wigner distribution and Weyl correspondence. *Nieuw Archief voor Wiskunde*, 21(3):205–280, 1973.
- [32] D.L. Donoho and I.M. Johnstone. Adapting to unknown smoothness via wavelet shrinkage. *Journal of the American Statistical Association*, 90(432):1200–1224, December 1995.
- [33] J. Duchon. Splines minimizing rotation-invariant semi-norms in Sobolev spaces. Springer Verlag, 1977.
- [34] R.J. Duffin and A.C. Schaeffer. A class of nonharmonic Fourier series. *Transactions of the American Mathematical Society*, 72(1):341–366, January 1952.
- [35] R. Duits. *Perceptual Organization in Image Analysis*. PhD thesis, Eindhoven University of Technology, 2005.
<http://www.bmi2.bmt.tue.nl/Image-Analysis/People/RDuits/THESISRDUIITS.pdf>.
- [36] R. Duits and B. Burgeth. Scale spaces on lie groups. In *Scale Space and Variational Methods in Computer Vision: Proceedings of the First International Conference, SSVM 2007, Ischia, Italy*, volume 4485 of *Lecture Notes in Computer Science*, pages 300–312, Berlin, 2008. Springer Verlag.
- [37] R. Duits, M. Felsberg, L.M.J. Florack, and B. Platel. α scale spaces on a bounded domain. In L. Griffin and M. Lillholm, editors, *Scale Space Methods in Computer Vision, 4th International Conference, Scale Space 2003*, pages 494–510, Isle of Skye, UK, June 2003. Springer.
- [38] R. Duits, L.M.J. Florack, B.M. ter Haar Romeny, and J. de Graaf. On the axioms of scale space theory. *Journal of Mathematical Imaging and Vision*, 20:267–298, 2004.
- [39] R. Duits and E.M. Franken. Left-invariant parabolic evolutions on $SE(2)$ and contour enhancement via invertible orientation scores - Part II: Nonlinear left-invariant diffusions on invertible orientation scores. *Quarterly on Applied Mathematics of the American Mathematical Society*, 2009.
- [40] R. Duits, H. Führ, and B.J. Janssen. Left invariant evolution equations on Gabor transforms. CASA report 9, Eindhoven

- University of Technology, Eindhoven, The Netherlands, February 2009.
- [41] R. Duits, B.J. Janssen, F.M.W. Kanters, and L.M.J. Florack. Linear image reconstruction from a sparse set of α -scale space features by means of inner products of Sobolev type. In O. Fogh Olsen, L.M.J. Florack, and A. Kuijper, editors, *Deep Structure, Singularities and Computer Vision*, volume 3753 of *Lecture Notes in Computer Science*, pages 96–111. Springer Verlag, 2005.
 - [42] L.M.J. Florack, R. Duits, and J. Bierkens. Tikhonov regularization versus scale space: A new result. In *Proceedings of the 11th International Conference on Image Processing (ICIP 2004)*, Singapore, volume 1, pages 271–274, October 2004.
 - [43] L.M.J. Florack, B.J. Janssen, F.M.W. Kanters, and R. Duits. Towards a new paradigm for motion extraction. In A. Campilho and M. Kamel, editors, *Image Analysis and Recognition, Third International Conference, ICIAR 2006*, volume 4141 of *Lecture Notes in Computer Science*, pages 743–754, Berlin, September 2006. Springer Verlag.
 - [44] L.M.J. Florack and A. Kuijper. The topological structure of scale-space images. *Journal of Mathematical Imaging and Vision*, 12(1):65–79, February 2000.
 - [45] L.M.J. Florack, R. Maas, and W.J. Niessen. Pseudo-linear scale-space theory. *International Journal of Computer Vision*, 31(2/3):247–259, April 1999.
 - [46] E.M. Franken. *Enhancement of Crossing Elongated Structures in Images*. PhD thesis, Eindhoven University of Technology, Eindhoven, The Netherlands, December 2008.
 - [47] E.M. Franken and R. Duits. Crossing-preserving coherence-enhancing diffusion on invertible orientation scores. *International Journal of Computer Vision*, 2009.
 - [48] D. Gabor. Theory of communication. *Journal of the Institution of Electrical Engineers*, 93(22):429–457, November 1946.
 - [49] I Galic, J. Weickert, M. Welk, A. Bruhn, A. Belyaev, and H. Seidel. Image compression with anisotropic diffusion. *Journal of Mathematical Imaging and Vision*, 31(2-3):255–269, July 2008.

- [50] T. Georgiev. Relighting, retinex theory, and perceived gradients. In *Proceedings of Mirage 2005*, March 2005.
- [51] R. Gilmore. *Catastrophe Theory for Scientists and Engineers*. Dover Publications, New York, 1993. Originally published by John Wiley & Sons, New York, 1981.
- [52] I.S. Gradshteyn and I.M. Ryzhik. *Table of Integrals, Series, and Products*. Academic Press, Boston, fifth edition, 1994. (Edited by A. Jeffrey.).
- [53] K. Gröchenig. *Foundations of Time-Frequency Analysis*. Birkhauser, first edition, 2001.
- [54] A. Grossmann, J. Morlet, and T. Paul. Transforms associated to square integrable group representations. i. general results. *Journal of Mathematical Physics*, 26(10):2473–2479, April 1985.
- [55] F.J. Harris. On the use of windows for harmonic analysis with the discrete fourier transform. *Proceedings of the IEEE*, 66(1):51–83, January 1978.
- [56] C.W. Helstrom. An expansion of a signal in gaussian elementary signals. *IEEE Transactions on Information Theory*, 12:81–82, January 1966.
- [57] T. Iijima. Basic theory on normalization of a pattern (in case of typical one-dimensional pattern). *Bulletin of Electrical Laboratory*, 26:368–388, 1962.
- [58] B. Jähne. *Digital Image Processing*. Springer, fifth edition, 2002.
- [59] A.J.E.M. Janssen. The Zak transform: A signal transform for sampled time-continuous signals. *Philips Journal of Research*, 43(1):23–69, 1988.
- [60] A.J.E.M. Janssen. Duality and biorthogonality for discrete-time Weyl-Heisenberg frames. Technical Report 002/94, Philips Natuurkundig Laboratorium, 1994.
- [61] A.J.E.M. Janssen. The duality condition for weyl-heisenberg frames. Technical report, Philips Natuurkundig Laboratorium, 1996.

- [62] B.J. Janssen, R. Duits, and B.M. ter Haar Romeny. Linear image reconstruction by Sobolev norms on the bounded domain. In F. Sgallari, A. Murli, and N. Paragios, editors, *Scale Space and Variational Methods in Computer Vision*, volume 4485 of *Lecture Notes in Computer Science*, pages 55–67. Springer Verlag, June 2007.
- [63] B.J. Janssen, L.M.J. Florack, R. Duits, and B.M. ter Haar Romeny. Optic flow from multi-scale dynamic anchor point attributes. In A. Campilho and M. Kamel, editors, *Image Analysis and Recognition, Third International Conference, ICIAR 2006*, volume 4141 of *Lecture Notes in Computer Science*, pages 767–779, Berlin, September 2006. Springer Verlag.
- [64] B.J. Janssen, F.M.W. Kanters, R. Duits, L.M.J. Florack, and B.M. ter Haar Romeny. A linear image reconstruction framework based on Sobolev type inner products. *International Journal of Computer Vision*, 70(3):231–240, 2006.
- [65] P. Johansen, M. Nielsen, and O.F. Olsen. Branch points in one-dimensional gaussian scale space. *Journal of Mathematical Imaging and Vision*, 13(3):193–203, 2000.
- [66] P. Johansen, S. Skelboe, K. Grue, and J.D. Andersen. Representing signals by their top points in scale-space. In *Proceedings of the 8th International Conference on Pattern Recognition*, pages 215–217, 1986.
- [67] J. Jost. *Riemannian Geometry and Geometric Analysis*. Springer, Berlin, fourth edition, 2005.
- [68] F.M.W. Kanters. *Towards Object-based Image Editing*. PhD thesis, Eindhoven University of Technology, Eindhoven, The Netherlands, February 2007.
- [69] F.M.W. Kanters, L.M.J. Florack, R. Duits, and B. Platel. Scalespaceviz: Visualizing α -scale spaces. Demonstration software, 2004. <http://bmia.bmt.tue.nl/people/FKanters/Software/ScaleSpaceViz.html>.
- [70] F.M.W. Kanters, L.M.J. Florack, R. Duits, and B.M. ter Haar Romeny. Scalespaceviz: alpha-scale spaces in practice. *Pattern Recognition and Image Analysis*, 17(1):106–116, 2007.

- [71] F.M.W. Kanters, B. Platel, L.M.J. Florack, and B.M. ter Haar Romeny. Image reconstruction from multiscale critical points. In L. Griffin and M. Lillholm, editors, *Scale Space Methods in Computer Vision, 4th International Conference, Scale Space 2003*, volume 2695 of *Lecture Notes in Computer Science*, pages 464–478. Springer Verlag, June 2003.
- [72] M. Kass and A.P. Witkin. Analyzing oriented patterns. *Computer Vision Graphics and Image Processing*, 37(3):362–385, March 1987.
- [73] K. Kodera, C. de Villedary, and R. Gendrin. A new method for the numerical analysis of non-stationary signals. *Physics of the Earth and Planetary Interiors*, 12:142–150, August 1976.
- [74] J.J. Koenderink. The structure of images. *Biological Cybernetics*, 50:363–370, 1984.
- [75] E. Kreyszig. *Advanced Engineering Mathematics*. Wiley, ninth edition, 1993.
- [76] J. Kybic, T. Blu, and M. Unser. Generalized sampling: a variational approach – part I: Theory. *IEEE Transactions on Signal Processing*, 50:1965–1976, August 2002.
- [77] J. Kybic, T. Blu, and M. Unser. Generalized sampling: a variational approach – part II: Applications. *IEEE Transactions on Signal Processing*, 50:1977–1985, August 2002.
- [78] G. Le Besnerais and F. Champagnat. B-Spline image model for energy minimization-based optical flow estimation. *IEEE Transactions on Image Processing*, 15(10):3201–3206, 2006.
- [79] M. Lillholm, M. Nielsen, and L.D. Griffin. Feature-based image analysis. *International Journal of Computer Vision*, 52(2/3):73–95, 2003.
- [80] T. Lindeberg. *Scale-Space Theory in Computer Vision*. The Kluwer International Series in Engineering and Computer Science. Kluwer Academic Publishers, 1994.
- [81] W.E. Lorensen and H.E. Cline. Marching cubes: A high resolution 3d surface construction algorithm. *Computer Graphics*, 21(4):163–169, 1987.

- [82] S. Mallat. Zero-crossings of a wavelet transform. *IEEE Transactions on Information Theory*, 37(4):1019–1033, July 1991.
- [83] S. Mallat. *A wavelet tour of signal processing*. Academic Press, 1998.
- [84] R.M.M. Mattheij, S.W. Rienstra, and J.H.M. ten Thije Boonkkamp. *Partial Differential Equations, Modeling, Analysis, Computation*. Monographs on Mathematica Modeling and Computation. Society for Industrial and Applied Mathematics, first edition, 2005.
- [85] J. Meinguet. Multivariate interpolation at arbitrary points made simple. *Journal of Applied Mathematics and Physics (ZAMP)*, 30:292–304, 1979.
- [86] M. Nielsen and M. Lillholm. What do features tell about images? In *Scale-Space and Morphology in Computer Vision: Proceedings of the Third International Conference*, pages 39–50. Springer Verlag, 2001.
- [87] M. Nitzberg and T. Shiota. Nonlinear image filtering with edge and corner enhancement. *IEEE Transactions on Pattern Analysis and Machine Intelligence*, 14(8):826–833, August 1992.
- [88] A.V. Oppenheim and S.L. Jae. The importance of phase in signals. *Proceedings of the IEEE*, 69(5):529–541, May 1981.
- [89] S. Osher and J.A. Sethian. Fronts propagating with curvature-dependent speed: Algorithms based on Hamilton-Jacobi formulations. *Journal of Computational Physics*, 79:12–49, 1988.
- [90] A. Papoulis. Generalized sampling expansion. *IEEE Transactions on Circuits and Systems*, 24:652–654, 1977.
- [91] P. Perona and J. Malik. Scale-Space and edge detection using anisotropic diffusion. *IEEE Transactions on Pattern Analysis and Machine Intelligence*, 12(7):629–639, July 1990.
- [92] B. Platel. *Exploring the Deep Structure of Images*. PhD thesis, Eindhoven University of Technology, Eindhoven, The Netherlands, 2007. <http://yp.wtb.tue.nl/pdfs/8198.pdf>.

- [93] B. Platel, F.M.W. Kanters, L.M.J. Florack, and E.G. Balmachnova. Using multiscale top points in image matching. In *Proceedings of the 11th International Conference on Image Processing (ICIP 2004)*, Singapore, pages 389–392, 2004.
- [94] W.H. Press, B.P. Flannery, S.A. Teukolsky, and W.T. Vetterling. *Numerical Recipes in C*. Cambridge University Press, second edition, 1988.
- [95] R.W. Rodieck. *The First Steps in Seeing*. Sunderland: Sinauer Associates, 1998.
- [96] E. Rouy and A. Tourin. A viscosity solutions approach to shape-from-shading. *SIAM Journal of Numerical Analysis*, 29(3):867–884, June 1992.
- [97] C.E. Shannon. Communication in the presence of noise. In *Proc. IRE*, volume 37, pages 10–21, January 1949.
- [98] E.M. Stein. *Harmonic Analysis: Real-Variable Methods, Orthogonality and Oscillatory Integrals*. Number 43 in Princeton Mathematical Series. Princeton University Press, Princeton, second edition, 1993.
- [99] C. Temperton. Algorithms for the solution of cyclic tridiagonal systems. *Journal of Computational Physics*, 19(3):317–323, November 1975.
- [100] M.E. Testorf, J. Ojeda-Castaneda, and A.W. Lohmann, editors. *Selected Papers on Phase-Space Optics*, volume MS181 of *SPIE Milestone Series*. The Society of Photo-Optical Instrumentation Engineers, Bellingham, Washington USA, 2006.
- [101] P. Thevenaz, U.E. Ruttimann, and M. Unser. A pyramid approach to subpixel registration based on intensity. *IEEE Transactions on Image Processing*, 7(1):27–41, January 1998.
- [102] A.N. Tikhonov and V.Y. Arsenin. *Solutions of Ill-Posed Problems*. John Wiley & Sons, New York, 1977.
- [103] M. Unser. Splines: A perfect fit for signal and image processing. *IEEE Signal Processing Magazine*, 16(6):22–38, November 1999.
- [104] M. Unser. Sampling—50 Years after Shannon. *Proceedings of the IEEE*, 88(4):569–587, April 2000.

- [105] M. Unser and A. Aldroubi. A general sampling theory for nonideal acquisition devices. *IEEE Transactions on Signal Processing*, 42:2915–2925, November 1994.
- [106] M. Unser, A. Aldroubi, and M. Eden. On the asymptotic convergence of B-Spline wavelets to Gabor functions. *IEEE Transactions on Information Theory*, 38(2):864–872, March 1992.
- [107] M.A. van Almsick. *Context Models of Lines and Contours*. PhD thesis, Eindhoven University of Technology, Eindhoven, The Netherlands, 2007.
- [108] R. van den Boomgaard. *Mathematical Morphology: Extensions Towards Computer Vision*. PhD thesis, University of Amsterdam, Amsterdam, 1992.
- [109] R. van den Boomgaard. Numerical solution schemes for continuous-scale morphology. In M. Nielsen, P. Johansen, O.F. Olsen, and J. Weickert, editors, *Scale-Space Theories in Computer Vision: Second International Conference*, volume 1682 of *Lecture Notes in Computer Science*, pages 199–210, Berlin, 1999. Springer Verlag.
- [110] R. van den Boomgaard and A. Smeulders. The morphological structure of images: The differential equations of morphological scale-space. *IEEE Transactions on Pattern Analysis and Machine Intelligence*, 16(11):1101–1113, November 1994.
- [111] A.J. van Leest. *Non-separable Gabor Schemes: Their Design and Implementation*. PhD thesis, Eindhoven University of Technology, Eindhoven, The Netherlands, January 2001.
- [112] A.O. Warburton. *Analyses of musical classics: Book 2*. Longman, London, 1967.
- [113] J. Weickert. *Anisotropic Diffusion in Image Processing*. ECMI. Teubner, Stuttgart, January 1998.
- [114] J. Weickert. Coherence-enhancing diffusion filtering. *International Journal of Computer Vision*, 31(2/3):111–127, 1999.
- [115] M. Welk, G. Steidl, and J. Weickert. Locally analytic schemes: A link between diffusion filtering and wavelet shrinkage. *Applied and Computational Harmonic Analysis*, 24:195–224, 2008.

- [116] M. Welk, J. Weickert, and G. Steidl. From tensor-driven diffusion to anisotropic wavelet shrinkage. In H. Bischof, A. Leonardis, and A. Pinz, editors, *Proceedings of ECCV 2006*, volume 3951 of *Lecture Notes in Computer Science*, pages 391–403, Berlin, 2006. Springer Verlag.
- [117] E.T. Whittaker and G.N. Watson. *Modern Analysis*. Camebridge University Press, 4 edition, 1946.
- [118] A.P. Witkin. Scale-space filtering. In *Proceedings of the International Joint Conference on Artificial Intelligence*, pages 1019–1022, Karlsruhe, Germany, 1983.
- [119] S. Wolfram. *Mathematica: A System for doing Mathematics by Computer*. Addison-Wesley, second edition, 1991.
- [120] K. Yamatani and N. Saito. Improvement of DCT-based compression algorithms using Poisson’s equation. *IEEE Transactions on Image Processing*, 15(12):3672–3689, December 2006.
- [121] K. Yosida. *Functional Analysis*. Springer Verlag, Berlin, sixth edition, 1980.
- [122] G. Yu, S. Mallat, and E. Barcy. Audio denoising by time-frequency block thresholding. *IEEE Transactions on Signal Processing*, 56(5):1830–1839, May 2008.
- [123] J. Zak. Finite translation in solid state physics. *Physical Review Letters*, 19:1385–1397, 1967.

Samenvatting (Summary in Dutch)

De reconstructie van een signaal uit een aantal monsterwaarden is een fundamenteel probleem in het vakgebied der signaalverwerking. Het zogenoemde reconstructieprobleem verdient en krijgt veel aandacht van de wetenschappelijke gemeenschap. In dit proefschrift wordt een algemene vorm van dit probleem behandeld. We trachten een beeld te reconstrueren dat is bemonsterd op een onregelmatig rooster en waarbij de monsterwaarden zijn verkregen middels lineaire functionalen op het bronbeeld. Als applicatie reconstrueren we een beeld uit haar differentiaal structuur die verkregen is uit de schaalruimterepresentatie van het bronbeeld. Hiertoe restricteren we de bemonstering tot bepaalde punten die afhangen van de structuur van het bronbeeld.

Naast het reconstrueren van beelden beschrijven we ook hoe tijd-frequentie representaties van signalen kunnen worden bewerkt. De voorgestelde bewerkingen dienen een tweetal doelen. Namelijk, het verbeteren van de leesbaarheid van tijd-frequentie representaties van signalen, en het ontruisen van signalen waarvan we de tijd-frequentie representatie verkregen hebben. De verbeteringen worden respectievelijk bewerkstelligd middels het uitvoeren van een convectie en een diffusieproces op een tijd-frequentie representatie van een signaal dat verkregen is door de Gabor getransformeerde van het signaal te berekenen. Om deze evolutieprocessen translatie en modulatie covariant te laten zijn op het signaaldomein voeren we de evolutieprocessen uit door middel van links-invariante operatoren in het tijd-frequentie domein. Dit wil zeggen dat de te gebruiken operatoren dienen te commuteren met de links-reguliere representaties van de Heisenberg groep. Dit deel van het proefschrift is een verfijning van een meer generieke theorie die schaalruimten op Lie groepen beschrijft.

In Hoofdstuk 2 wordt een lineaire reconstructiemethode beschreven. Deze methode produceert een beeld uit een aantal monsterwaarden die verkregen zijn met behulp van een aantal filters. Wanneer men het gereconstrueerde beeld opnieuw bemonstert met diezelfde filters dan kan er op grond van de nieuwe monsterwaarden geen onderscheid gemaakt worden tussen het gereconstrueerde beeld en het bronbeeld. Omdat er verschillende beelden bestaan die deze eigenschap bezitten wordt er een uniek beeld gekozen dat een zeker model zo goed mogelijk benadert. Dit model dient een door een inproduct geïnduceerde norm te zijn zodat de reconstructie middels een

projectie kan worden verkregen. We laten zien dat, wanneer er voor een Sobolev norm gekozen wordt, men visueel aantrekkelijke reconstructies kan verkrijgen. In dit hoofdstuk wordt verondersteld dat het domein van het beeld de gehele \mathbb{R}^n beslaat. Er wordt derhalve geen aandacht besteed aan de randvoorwaarden.

Hoofdstuk 3 beschrijft een reconstructiemethode die vergelijkbaar is met de methode die wordt beschreven in Hoofdstuk 2. Nu nemen we de begrensdheid van het beeld echter wel in acht. Dit heeft als voordeel dat de problemen, die optreden in het onbegrensd domein wanneer veel regularisatie wordt toegepast, kunnen worden vermeden. De implementatie van de methode wordt geheel in het discrete domein beschreven en is exact op een regelmatig rooster. Approximatie- en truncatiefouten treden door deze aanpak niet op.

De bovengenoemde reconstructiemethoden interpoleren de gegeven monsterwaarden. In Hoofdstuk 4 wordt een methode beschreven die deze waarden juist approximeert. De approximatiemethode stelt ons in staat een grof-naar-fijn reconstructiemethode te formuleren die informatie op grove resolutie naar een fijnere resolutie propageert middels een ijkveld. Om een ijkveld te kunnen gebruiken wordt het beeld niet beschouwd als een scalar functie maar als een sectie door een zogenoemde gefiberde ruimte.

Het verbeteren van de leesbaarheid van een tijd-frequentie representatie van een signaal wordt ook wel “hertoekenning” (Engels reassignment) genoemd. Dit onderwerp wordt besproken in Hoofdstuk 5. Daar laten we zien dat de Gabor getransformeerde van een signaal gezien kan worden als een functie op de Weyl-Heisenberg groep. Met behulp van links-invariante vectorvelden definiëren we operatoren op het domein van Gabor getransformeerden van signalen. De resulterende operatoren gebruiken we vervolgens om een adaptief convectieproces op de Gabor getransformeerde van een signaal te definiëren dat zowel translatie- als modulatiecovariant is op het signaaldomein. Dit proces leidt tot een gemakkelijker interpreteerbare tijd-frequentie representatie van het te analyseren signaal. Om een computerimplementatie te kunnen maken identificeren we allereerst een discrete groep waarvoor we de discrete links-invariante vectorvelden berekenen. Met behulp van deze discrete vectorvelden maken we vervolgens een implementatie die gerestricteerd is tot een discreet rooster waardoor we interpolatiefouten kunnen vermijden.

In Hoofdstuk 6 passen we de in Hoofdstuk 5 ontwikkelde theorie toe op het ontruisen van signalen. Dit wordt gedaan door een links-invariant niet-lineair anisotroop diffusieproces uit te voeren op de Gabor getransformeerde van een signaal. Door de gemodificeerde tijd-frequentie representatie terug te transformeren naar het signaaldomein verkrijgt men een ontruiste versie van het bronsignaal. Onze methode is prefereerbaar boven de meer conventionele drempelmethoden omdat het in staat is rekening te houden met lokale informatie. Niet-lineaire diffusiemethodes op het signaal hebben dit voordeel ook maar deze zijn niet in staat verschillende tijd-frequentie structuren te separeren.

Dankwoord

Zo... nu het meest gelezen gedeelte van de binnenkant van dit proefschrift. Ondanks dat ik graag slechts één enkel woord zou willen besteden aan deze sectie en dat eenieder die ik daarmee impliciet aanspreek waarschijnlijk wel weet dat het voor hem of haar bedoeld is, zal ik deze sectie gebruiken om enkele woorden aan diegenen te richten die het schrijven van dit proefschrift veraangenaamd hebben.

Herr dr. Duits, Remco, bedankt voor de fantastische samenwerking en de enthousiaste wijze waarop jij de rol van copromotor op je hebt genomen. Ik heb ontzettend veel van je geleerd in de afgelopen jaren en bewonder de brede kennis van de wiskunde die je bezit en weet over te brengen. Luc, bedankt voor de plek die ik mocht innemen in je “fundamentalistische” VICI-project. Ook de vrijheid die je me als eerste promotor gegeven hebt in mijn onderzoek kan ik erg waarderen. Tweede promotor Bart, bedankt voor je enorme enthousiasme en de leuke groep die je neer hebt gezet bij BMT. Mede door jouw enthousiasme ben ik in de mathematische beeldverwerking terechtgekomen.

Verder wil ik mijn (voormalig) kamergenoten bij BMT en W&I, Bram, Erik, Evgeniya, Frans en Laura, graag bedanken voor de leuke tijd die ik met jullie heb gehad in de afgelopen jaren. Mijn dank wil ik dan ook uiten middels de op de voorkant van dit proefschrift prijkende groet. Voormalig tafelgenoten in het BMIA lab, Tim en Arjen, ook jullie wil ik bedanken middels diezelfde groet. Paranimf dr. dr. F., Erik, bedankt voor de leuke samenwerking en je geweldige humor die zelfs terug te vinden is in de broncode van de door ons opgezette library: MathVisionC++. Markus, bedankt voor je perfectionisme. Met name door jou was IMS'08 een succes. Alessandro en Pieter, ook jullie bedankt voor de goede samenwerking. Naast de bovengenoemde personen wil ik alle andere mensen bij BMIA en CASA bedanken voor het veraangename van mijn promotietijd.

Prof. Michael Unser, thank you for your hospitality. I really enjoyed my stay at the EPFL. Prof. Hartmut Führ, thank you for inviting Remco and me to Aachen. You provided important input for the work in this thesis. Sorry we failed to present you decent food during lunch in Eindhoven. Dr. A.J.E.M. (Guido) Janssen, bedankt voor het deelnemen aan de lezerscommissie en je gedetailleerde commentaar.

Natuurlijk wil ik ook de vaste ODIN lunchbezoekers niet vergeten. Erik, Iwan, Johan en Thijs: bedankt voor de gezellige lunches, de relatief goede koffie, mooie verhalen over konijnen, umami, vlees, geen vlees, het broeikas effect, etc. Ook de vaste en door arbeid minder vaste Walhalla/InVivo bezoekers wil ik graag bedanken. Te weten: Bakkus, Coen, Helle, Iwan, Jeroentje, Johan, Maes, Marjan, Martijn, Peter, Ronnie, Sanne, Thijs, Zef. Hopelijk kan de traditie nog een tijdje in stand blijven. Paranimf Maes, ik ben verheugd dat je me bij zult staan mocht het tot een handgemeen komen tijdens de verdediging van dit proefschrift. Met iemand van jouw kaliber aan mijn zijde kan ik de verdediging met vertrouwen tegemoet treden.

Leden van DMW, ook jullie hebben bijgedragen aan de leuke tijd die ik gehad heb tijdens mijn promotieonderzoek. Bedankt voor de leuke repetities en optredens. Sorry dat ik jullie dit jaar met carnaval in de steek moest laten omwillen van dit proefschrift.

Op dit punt wil ik iedereen bedanken die ik hierboven niet genoemd heb maar met dat ene woord wel aangesproken zou hebben.

Pap & Mam, Gijs & Sanne, Stijn & Tessa, Herman & Marleen en Martijn bedankt voor jullie steun. En Marjan... bedankt voor je liefde, bedankt voor het helpen tunen van de kافت van dit proefschrift en het aanhoren van “nerd” verhalen. Ook bedankt voor je geduld, begrip en steun, met name in de laatste fase van mijn promotie.

Curriculum Vitae

Bart Janssen was born in Geldrop, The Netherlands on January 25th 1980. After his pre-university graduation from the Dr. Knippenberg College in Helmond he started his studies Electrical Engineering at Eindhoven University of Technology. During his studies he fulfilled an internship on object tracking at Robert Bosch GmbH in Hildesheim, Germany. The subject of his M.Sc. thesis was multi-scale optic flow for which he received the M.Sc. degree in February 2005.

In March 2005 he started his Ph.D. research within the Biomedical Image Analysis group at Eindhoven University of Technology. He visited the Biomedical Imaging Group headed by prof. Unser at École Polytechnique Fédérale de Lausanne, Switzerland, in 2005 and the Lehrstuhl A für Mathematik headed by prof. Führ at Rheinisch-Westfälische Technische Hochschule Aachen, Germany, in 2008. He was a member of the organizing committee of the 9th International Mathematica Symposium, which was held in 2008 in Maastricht, The Netherlands. Results of his M.Sc. and Ph.D. research have been published in international peer reviewed journals and presented at international conferences.

Publications

B.J. Janssen and R. Duits. Linear image reconstruction by Sobolev norms on the bounded domain. *International Journal of Computer Vision*, 84(2):205–219, August 2009. (Invited Paper)

B.J. Janssen, R. Duits, and L.M.J. Florack. Coarse-to-fine image reconstruction based on weighted differential features and background gauge fields. In *Scale Space and Variational Methods in Computer Vision: Proceedings of the Second International Conference, SSVM 2009, Voss, Norway*, Lecture Notes in Computer Science, Berlin, June 2009. Springer Verlag.

R. Duits, H. Führ, and B.J. Janssen. Left invariant evolution equations on Gabor transforms. CASA report 9, Eindhoven University of Technology, Eindhoven, The Netherlands, February 2009.

A. Becciu, B.J. Janssen, H.C. Assen, L.M.J. Florack, V. Roode, and B.M. ter Haar Romeny. Extraction of cardiac motion using scale-space feature points and gauged reconstruction. In *Proceedings of The 13th International Conference on Computer Analysis of Images and Patterns (CAIP09)*, Lecture Notes in Computer Science. Springer Verlag, 2009. Accepted for publication.

P.A.G. Dorst, B.J. Janssen, L.M.J. Florack, and B.M. ter Haar Romeny. Optic flow using multi-scale anchor points. In *Proceedings of The 13th International Conference on Computer Analysis of Images and Patterns (CAIP09)*, Lecture Notes in Computer Science, Berlin, 2009. Springer Verlag. Accepted for publication.

R. Duits, H. Führ, and B.J. Janssen. Left invariant evolution equations on Gabor transforms. In L.M.J. Florack et. al, editors, *Locally Adaptive Filters in Signal and Image Processing*. Springer Verlag, 2009. Accepted for publication.

M.A. van Almsick, B.M. ter Haar Romeny, and B.J. Janssen, editors. *Proceedings of the 9th International Mathematica Symposium*, Maastricht, The Netherlands, June 2008.

A. Becciu, H.C. Assen, L.M.J. Florack, B.J. Janssen, and B.M. ter Haar Romeny. Cardiac motion estimation using multi-scale feature points. In *Proceedings of the MICCAI 2008 workshop on Computational Biomechanics for Medicine III*, New York, pages 5–14, 2008.

A. Becciu, H.C. Assen, L.M.J. Florack, B.J. Janssen, and B.M. ter Haar Romeny. Cardiac motion estimation using multi-scale maxima. In *Proceedings of the of the fourteenth annual conference of the Advanced School for Computing and Imaging (ASCI)*, Heijen, The Netherlands, 2008.

P.A.G. van Dorst, A. Becciu, B.J. Janssen, L.M.J. Florack, and B.M. ter Haar Romeny. Robust multi-scale optic flow using toppoints. In M.A. van Almsick, B.M. ter Haar Romeny, and B.J. Janssen, editors, *Proceedings of the 9th International Mathematica Symposium*, Maastricht, The Netherlands, June 2008.

E.M. Franken and B.J. Janssen. MathVisionC++ for efficient medical image processing in mathematica. In M.A. van Almsick, B.M. ter Haar Romeny, and B.J. Janssen, editors, *Proceedings of the 9th International Mathematica Symposium*, Maastricht, The Netherlands, June 2008.

B.J. Janssen, R. Duits, and B.M. ter Haar Romeny. Linear image reconstruction by Sobolev norms on the bounded domain. In F. Sgallari, A. Murli, and N. Paragios, editors, *Scale Space and Variational Methods in Computer Vision*, volume 4485 of *Lecture Notes in Computer Science*, pages 55–67. Springer Verlag, June 2007.

B.J. Janssen, F.M.W. Kanters, R. Duits, L.M.J. Florack, and B.M. ter Haar Romeny. A linear image reconstruction framework based on Sobolev type inner products. *International Journal of Computer Vision*, 70(3):231–240, 2006. (Invited Paper)

B.J. Janssen, L.M.J. Florack, R. Duits, and B.M. ter Haar Romeny. Optic flow from multi-scale dynamic anchor point attributes. In A. Campilho and M. Kamel, editors, *Image Analysis and Recognition, Third International Conference, ICIAR 2006*, volume 4141 of *Lecture Notes in Computer Science*, pages 767–779, Berlin, September 2006. Springer Verlag.

B.J. Janssen. Linear image reconstruction from multi-scale interest points. Invited talk at the Workshop on Image Analysis and Inverse Problems, EURANDOM, The Netherlands, December 11–13 2006.

L.M.J. Florack, B.J. Janssen, F.M.W. Kanters, and R. Duits. Towards a new paradigm for motion extraction. In A. Campilho and M. Kamel, editors, *Image Analysis and Recognition, Third International Conference, ICIAR 2006*, volume 4141 of *Lecture Notes in Computer Science*, pages 743–754, Berlin, September 2006. Springer Verlag.

H.E. Bennink, J.M. Korbeeck, B.J. Janssen, and B.M. ter Haar Romeny. Warping a neuro-anatomy atlas on 3D MRI data with radial basis functions. In *Proceedings of the International Conference on Biomedical Engineering (Biomed)*, Kuala Lumpur, 2006.

B.J. Janssen, F.M.W. Kanters, R. Duits, and B.M. ter Haar Romeny. A linear image reconstruction framework based on Sobolev type inner products. In *Scale Space and PDE Methods in Computer Vision: Proceedings of the Fifth International Conference, Scale-Space 2005, Hofgeismar, Germany*, volume 3459/2005 of *Lecture Notes in Computer Science*, pages 85–96, Berlin, 2005. Springer Verlag.

B.J. Janssen, L.M.J. Florack, and B.M. ter Haar Romeny. GigaNumerics in deep structure analysis of images. In *Proceedings of the Wolfram Technology Conference*, Champaign, Illinois, October 6–8 2005.

R. Duits, B.J. Janssen, F.M.W. Kanters, and L.M.J. Florack. Linear image reconstruction from a sparse set of α -scale space features by means of inner products of Sobolev type. In O. Fogh Olsen, L.M.J. Florack, and A. Kuijper, editors, *Deep Structure, Singularities and Computer Vision*, volume 3753 of *Lecture Notes in Computer Science*, pages 96–111. Springer Verlag, 2005.

F.M.W. Kanters, M. Lillholm, R. Duits, B.J. Janssen, B. Platel, L.M.J. Florack, and B.M. ter Haar Romeny. On image reconstruction from multiscale top points. In R. Kimmel, N. Sochen, and J. Weickert, editors, *Scale Space and PDE Methods in Computer Vision: Proceedings of the Fifth International Conference, Scale-Space 2005, Hofgeismar, Germany*, Lecture Notes in Computer Science, pages 431–442, Berlin, 2005. Springer Verlag.

